1244

Electric field and photocarrier collection in amorphous silicon p-i-n solar cells

Effects of light-induced degradation and of low-level i-layer doping

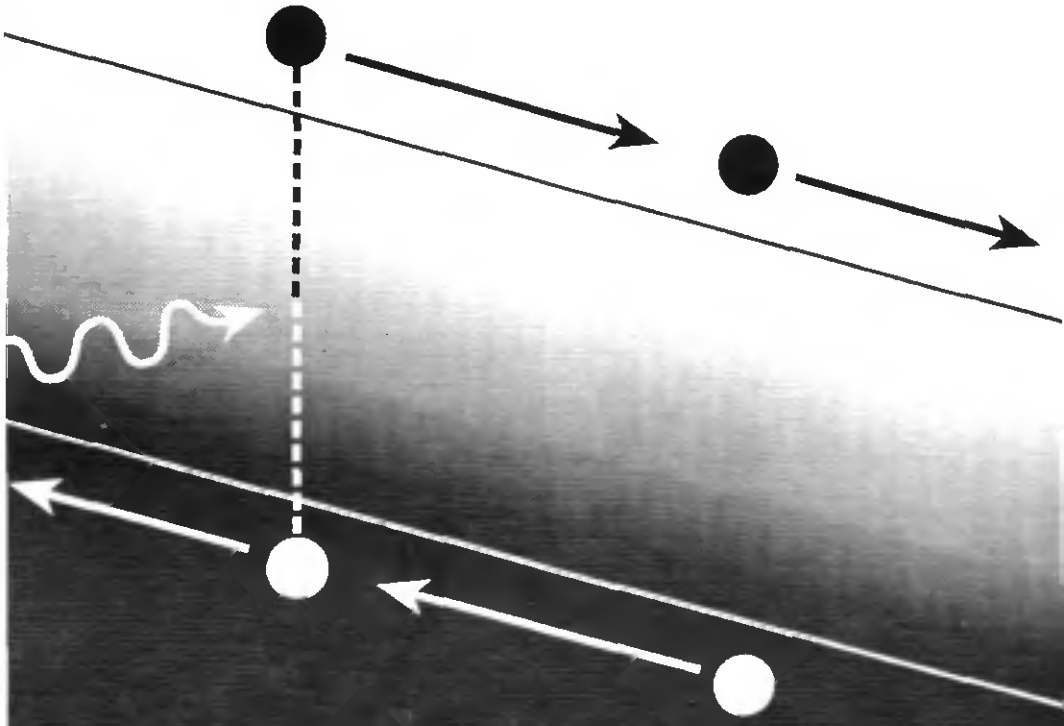

Diego Fischer - PhD Thesis - 1994

Institut de Microtechnique - Université de Neuchâtel

Université de Neuchâtel

Institut de Microtechnique

Electric field and photocarrier collection in amorphous silicon p-i-n solar cells

Effects of light-induced degradation and of low-level i-layer doping

Thèse

Présentée à la faculté des sciences
pour obtenir de titre de docteur ès sciences

par

Diego Fischer

Dipl. El. Ing ETH

Neuchâtel, novembre 1994

IMPRIMATUR POUR LA THÈSE

Electric field and photocarrier collection in amorphous silicon p-i-n solar cells: Effects of light-induced degradation and low-level i-layer doping

de Monsieur Diego Fischer

UNIVERSITÉ DE NEUCHÂTEL

FACULTÉ DES SCIENCES

Le Faculté des sciences de l'Université de Neuchâtel
sur le rapport des membres du jury,

Messieurs A. Shah, N. de Rooij, M. Ilegems (EPF-Lausanne), H. Schade (Phototronics, Munich) et C. Fortmann (Penn State University)

autorise l'impression de la présente thèse.

Neuchâtel, le 13 octobre 1994

Le doyen:

H.-H. Nägeli

Abstract

The effect of the i-layer electric field on the photocarrier collection in amorphous silicon p-i-n solar cells is studied both theoretically and experimentally. The focus is on the electric field distortions caused by charged light-induced defects, and on the compensation of these distortions by low-level graded doping in the i-layer.

A numerical model, simulating the photocarrier transport within the i-layer, and defining boundary conditions at the i-layer / doped layer interfaces, is developed to analyse the p-i-n solar cell operation. Experimentally, p-i-n solar cells with and without graded low-level i-layer doping are fabricated by VHF glow-discharge. The solar cells are characterised by the bifacial DICE method which yields the position dependent i-layer collection with an increased accuracy. Further, the i-layer electric fields are measured by transient photocurrent analysis.

Electric field distortions caused by charged gap-states are shown to govern the operation of amorphous silicon p-i-n solar cells. The illumination mode of the solar cell is found to strongly influence the charging of the i-layer gap-states, and thus to play a key role in those mechanisms.
For illumination with strongly absorbed light, the threshold behaviour of the voltage dependent current collection is explained in terms of the extension of the electric field in the i-layer. The threshold voltages are directly linked to the concentrations of charged gap-states within the i-layer of the solar cell. The concentration of ionised dopants, charged valence-band tail states, and charged dangling-bonds are measured in this way.

After light-soaking, standard p-i-n solar cells are found to exhibit a strong collection asymmetry, with a high collection at the p-i interface, and a low collection towards the n-i interface. This is explained as the effect of a dominating positive dangling-bond space charge at the p-side of the i-layer. The creation of positive space charges by the light-soaking is corroborated by the recovery effects found in cells with low-level boron doping.

With graded doping of the i-layer in the 1 ppm range, a controlled manipulation of the distribution of the i-layer electrical potential is demonstrated.
By applying an i-layer boron doping profile that linearly decreases from the p-i interface, the positive dangling-bond space charge is locally compensated. At an optimal doping concentration, the compensated p-i-n solar cells exhibit a symmetric i-layer collection after degradation. Such optimally compensated cells are shown to have the potential to increase the stabilised performance of stacked a-Si:H solar cells.

Table of contents

1 Introduction

"The amorphous silicon solar cell challenge"

The potential of photovoltaic power generation

Photovoltaic cells, or solar cells, directly generate electric power from sunlight. The attractiveness of the photovoltaic use of solar energy is in the fact that the energy conversion takes place in an inert semiconductor layer, not involving moving parts or mass flows. The photovoltaic power generation is thus very reliable, and requires practically no maintenance.

Photovoltaic power generating systems consist of an assembly of identical solar cell modules. Due to this modularity, systems from a few watts up to the megawatt size can be realised, with the performance and the specific costs in essence independent of the size of the system [LEN94]. This makes it possible to generate power on virtually any available surfaces.

With a solar cell conversion efficiency of 10 % and under average Swiss climatic conditions, 1 m^2 of solar cells produces 80 kWh of electric energy per year [MEI94] (the efficiency of today's commercially available solar cells is in the range of 5-15 %). To cover the average consumption of a Swiss household (3000 kWh/year), a solar cell area of about 6 m x 6 m is needed. The areas required for power generation by photovoltaics are thus well within the range of areas directly available on roofs and facades of the buildings in which the power is consumed. Table 1.1 gives an overview over typical system sizes and energy productions for Swiss climatic conditions.

Table 1.1: Electric power produced by photovoltaic systems of different sizes

type of system	area	efficiency	peak power[a)]	energy production	no. hh[b)]
Solar cell module A	1 m^2	10 %	100 W_p	80 kWh/a[c)]	0.027
Solar cell module B	1 m^2	15 %	150 W_p	120 kWh/a[c)]	0.04
Family home system	37.5 m^2	10 %	3750 W_p	3000 kWh/a[c)]	1
Road side system, N13, Chur, CH	970 m^2	11.3 %	110 kW_p	113 MWh/a[d)]	38
for comparison:					
Total annual solar cell production (1992)	0.6 km^2	5-15 %	60 MW_p	48 GWh/a[c)]	16000
Total CH electricity demand[e)] (1992) by PV	400 km^2	15 %	60000 MW_p	48000 GWh/a	16 Mio.

a): DC power produced by the solar cells at full sunshine (at so called standard conditions, see section 2.2.1)
b): number of average CH households that can be fully supplied by this amount of electricity (w/o el. hot water)
c): annual electricity fed to the AC grid, based on a measured average performance of 130 PV systems in CH [MEI94]
d): measured performance, 1993 [CLA94]
e): total electricity demand of households, industry, services, and transportation

The reason that currently prohibits the large-scale application of photovoltaic power generation are the high costs. With today's commercially available solar cell technologies, energy costs are around

1 Fr/kWh [LEN94]. This is to be compared with 0.1 Fr/kWh for conventional electricity generation [LEN94].
Definitely, to realise a widespread application of photovoltaics for power generation, the cost of photovoltaically generated electricity must be reduced. This can be done by reducing the cost of the solar cell fabrication, or by increasing the performance (efficiency) of the solar cells, or both. To integrate photovoltaic cells in building elements that serve also other functions, might be a key to further decrease the costs.
Obviously, in addition to the technological aspects, the progress of photovoltaic energy, as well as of the renewable energies in general, will depend to a large degree on a favourable global energy policy. E.g. should the external costs of energy use be accounted for to achieve a level play-field for the different energy sources (pollution taxes, etc.). Only such measures, together with the technical progress, will open the way towards a sensible energy future.

Amorphous silicon solar cells

Among the different photovoltaic technologies considered today, solar cells made from amorphous silicon have a great potential to yield the needed advances in the cost to performance ratio. This is due to the following characteristics of the amorphous silicon solar cell technology:

- Amorphous silicon solar cells are thin film solar cells. Because of the high optical absorption of the material, a large part of the solar spectrum can be absorbed in a less than 1 µm thick solar cell. The use of highly purified silicon per square meter of solar cell is thus more than 100 times lower than for crystalline solar cells [VAU93].

- Large area amorphous silicon solar cells can be fabricated by low-cost plasma deposition. On an industrial level, solar cell deposition over an area of $1 m^2$ has been demonstrated [MAC90]. Also, continuous fabrication has been demonstrated (e.g. roll to roll deposition on flexible substrates of 300 m x 0.3 m [NAT90]). The plasma deposition is carried out at relatively low temperatures (250°C). This has the advantage of a small energy consumption. Also, due to the low temperatures, many different substrate materials can be employed (glass, metal, plastic: see Figures 1.1 and 1.2).

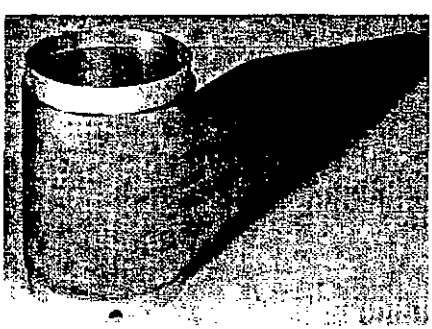

Figure 1.1: Amorphous silicon solar cell, continuously deposited by plasma deposition on a flexible plastic film (Teijin Co., Japan)

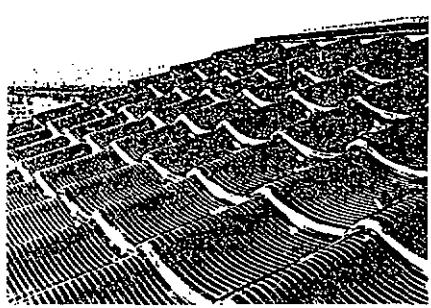

Figure 1.2: Amorphous silicon solar cells directly deposited on glass roof-tiles (Sanyo Co., Japan)

- If deposited on insulating substrates, amorphous silicon solar cells can be easily separated by laser-scribing into unit cells and then monolithically interconnected to form a high voltage solar module. This reduces the module fabrication costs.

- Amorphous silicon is a non-toxic material. Also, the base material silicon is a most abundant element.

Amorphous silicon solar cells today make up for about 30 % of the world-wide production of solar cells. The rest of the market is covered by crystalline silicon solar cells. Amorphous silicon is in particular successful in the range of the very small scale applications, such as electronic calculators, watches, etc. Concerning larger units (modules > 10 W_p, as required for bulk power generation) amorphous silicon, despite its advantages, has not yet been able to compete with crystalline silicon. This is explained by too low efficiencies of only 4 - 6 % as compared to crystalline silicon (10-15 % efficiency). Also, at the current small production volumes, the inherent advantages of amorphous silicon (large area capability, continuos fabrication capability, and the low silicon consumption) could not yet made sufficiently effective, resulting in specific costs (cost per W_p) similar to cristalline. This present situation is however likely to change in the coming years if advances are made in two respects:

- increase of stable efficiencies: on a laboratory scale, stable efficiencies of over 10 % are currently being achieved. Yet higher values must be realised, and these values have to be transferred to commercial production.

- while maintaining high efficiencies, the costs must be reduced: this includes e.g. question of the substrate related costs, where novel solutions are currently being implemented (avoid expensive TCO coated glass, deposition on plastics, building elements, etc.). Also, even at moderate production volumes, the inherent benefits of the amorphous silicon solar cell fabrication must be better employed (continuous fabrication, high speed deposition).

If substantial progress can be realised in these two fields, a new generation of cost effective amorphous silicon solar cells can make a break-through of photovoltaic power generation more likely to happen.

Approach and content of this work

This work wants to contribute to the performance improvement of amorphous silicon solar cells. It treats different aspects of the modelling, the characterisation, and the design of amorphous silicon solar cells. The focus is on issues directly related to the operation of the actual solar cell devices. This is in contrast to the majority of the current academic research efforts, which are rather focused on amorphous silicon materials aspects. In the view of the author, an intensified research on the device level would be imperative to effectively advance the performance of amorphous silicon solar cells. This is because the performance of the solar cells is governed to a significant part by device related effects that are only addressed by the study of complete solar cells.
In this sense, the present work concentrates on a typical device issue, the p-i-n solar cell internal electric field. The distribution of the electric field over the solar cell i-layer will be shown to vary

strongly as a function of different space-charges. These variations control the photocarrier collection, and thus the overall solar cell performance. While some space-charges seem to be inherent of amorphous silicon materials (dangling-bond states, tail-states), it will be shown that the application of minute concentrations of dopants in the i-layer allows to intentionally alter the space-charge, and thus to freely engineer the i-layer electric field distribution. It will be demonstrated that with such controlled manipulations, the electric field can be optimised towards an increase of the solar cell performance.

Chapter 2 presents the different 'tools' to be used. It starts with a discussion of the basic operation principles of p-i-n solar cells, leading to a set of simplified expressions that describe the major elements of the p-i-n solar cell operation. These expressions constitute a solar cell model, which will later be used to explain the different effects seen experimentally. A further part of this chapter consists in presentation of different characterisation methods judged particularly useful for the analysis of amorphous silicon solar cells. A special focus is on a generalised approach treating the interpretation of the spectral response under bias illumination, as well as on the introduction of the bifacial DICE method. In addition, a brief overview will be given over the solar cell fabrication technology that is employed in the present work.

Chapter 3 investigates the mechanisms involved in the light-induced degradation of the p-i-n solar cell. The influence of light-induced (dangling bonds) and constant (tail-states) states on the i-layer electric field will be analysed and discussed in detail. The comparison of the solar cell measurement and modelling shows that an increase of bulk i-layer defects, and the corresponding electric field distortions, can explain the major effects of the light-induced degradation. It is further shown that threshold-like behaviours in the solar cell current collection can be quantitatively linked to the i-layer space-charge densities, opening an interesting way of characterising amorphous silicon material properties direcly in the device structure.

Chapter 4 treats p-i-n solar cells with low-level doped i-layers. The motivation is to find out whether electric field distortions due to the light-induced defects can be compensated in order to improve the stable solar cell efficiency. First, different doping profiles are implemented to study the general effects of both the doping position and polarity on the electric fields, and the resulting solar cell operation. Then the doping profiles are optimised to compensate the space-charge of the light-induced defects. It will be demonstrated that in fact with a suitable graded boron doping scheme, the stable red light conversion efficiency of p-i-n cells can be increased. These p-i-n cells, used as bottom cells, are expected to enhance the stabilised performance of amorphous silicon tandem solar cells.

2 Amorphous silicon p-i-n solar cells: Modelling, characterisation, technology

"The tools"

2.1 p-i-n solar cell operation and modelling

In this section, the operation principles of amorphous silicon p-i-n solar cells are introduced and discussed. The goal is to define a suitable solar cell model that later on can be used to explain the measured solar cell behaviours. This model is designed to represent all the major mechanisms involved in the solar cell operation, but also an attempt was made to keep the number of modelling parameters as low as possible so that the modelling has a maximal transparency.

2.1.1 Light absorption

The first step of the photovoltaic energy conversion in semiconductor based solar cells is the optical absorption of photons in the semiconductor material, leading to the creation of free electron-hole pairs. This absorption can be regarded independently of the subsequent steps of separation and collection of the resulting electrical carriers in the semiconductor junction.

Figure 2.1 shows the optical absorption of hydrogenated amorphous silicon (a-Si:H) as a function of the wavelength of the light. Additionally, the absorption of crystalline silicon, and the AM1.5 [MAT84] solar spectrum power density are plotted. The most relevant feature of the absorption curve of a-Si:H is the greater absorption in the wavelength region from 300 - 700 nm compared to that of crystalline silicon. It is this high optical absorption that makes amorphous silicon a suitable thin film solar cell material.

The horizontal lines in Figure 2.1 give an estimate of the absorption limit of films with different

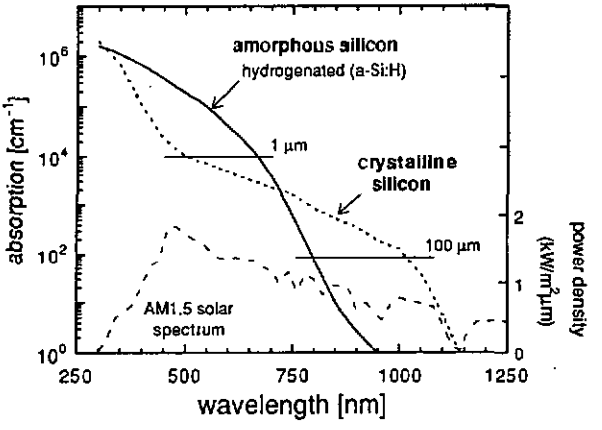

Figure 2.1: Optical absorption coefficients for hydrogenated amorphous silicon (a-Si:H) and crystalline silicon and AM1.5 /100 mW/cm² solar spectrum power density (dashed line, from [MAT84]).

thicknesses. At a thickness of 1 µm, an a-Si:H film can absorb the light up to wavelengths much longer than a crystalline silicon film of the same thickness. The sharp decrease of the absorption of a-Si:H at higher wavelengths on the other hand makes it virtually impossible to exploit the fractions of the sun spectrum above 750 nm with a-Si:H (by alloying a-Si:H with germanium (a-SiGe), the absorption can be extended to about 900 nm).

Figure 2.2 shows the photocarrier generation rate G(x) in a-Si:H, as a function of the penetration depth x, as produced by the AM1.5 solar spectrum (at 100 mW/cm^2)

$$G(x) = \int_0^{\infty} p_{AM1.5}(\lambda) \cdot \frac{\lambda}{h \cdot c} \cdot \alpha(\lambda) \cdot e^{-x \cdot \alpha(\lambda)} \cdot d\lambda \tag{2.1}$$

and the resulting cumulative photo generation current J_{light} (L)

$$J_{light}(L) = q \cdot \int_0^{L} G(x) \cdot dx \tag{2.2}$$

The generation rate sharply decays in the first few tenths of a micrometer, and for thicknesses greater than 0.5 µm the resulting photo current saturates towards a value of ~20 mA/cm^2. In practice, two effects lead to deviation from this theoretical curve. First, different loss mechanisms reduce the usable photo current. The losses include reflection and transmission losses in non-photovoltaically-active overlayers, etc. On the other hand, various "optical enhancement" schemes can increase the photo current by lengthening the optical path of the light. For example the absorption probability is increased by a reflection at the back side of the layer (if the reflection is 100 %, the thickness required to absorb a given photo-current is reduced to one half, as indicated in Figure 2.2), and by other than perpendicular angles of incidence of the light as realised by using textured substrates (see chapter 2.3).

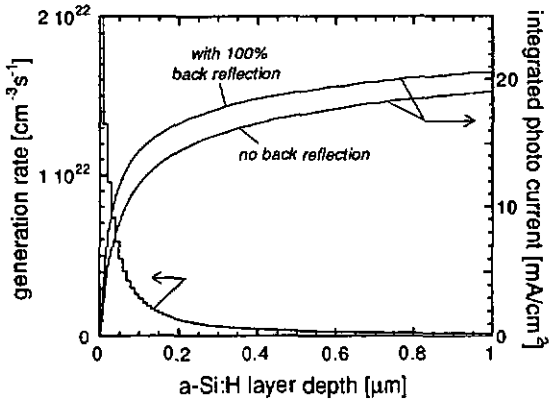

Figure 2.2: Calculated generation rate as a function of penetration depth, and totally generated photo current to this depth for single and double light pass, in an amorphous silicon (a-Si:H) layer (same absorption coefficient as in Figure 2.1) and for the AM1.5/100 mW/cm^2 solar spectrum (Figure 2.1).

2.1.2 Carrier collection in p-i-n solar cells

To produce electrical power available on external electrical terminals, i.e. to realise photovoltaic energy conversion, the photo-generated electrons and holes have to be separated in a suitable electronic device. It is thereby crucial to prevent the recombination of the electrons and holes in the absorbing material itself. Typically, the separation is achieved by electrostatic barriers that are induced in the solar cell material through an appropriate doping scheme.

Due to the high recombination probability in amorphous silicon, p-i-n diodes have proven to be the most successful solar cell design for a-Si:H [CAR76]: In a p-i-n device, the electrostatic barrier between a p-doped and a n-doped layer (the built-in potential V_{bi}) is used to induce an electric field into a non-doped, intrinsic layer (i-layer), which extends over most of the solar cell (Figure 2.3). In this intrinsic layer, the electric field enhances the carrier transport to a degree that allows for the collection of the photocarriers before they recombine. This is in contrast to the situation in other photovoltaic materials (e.g. crystalline silicon) where the recombination is low enough that the carriers can be transported to a very narrow electric field zone by diffusion alone (p-n solar cells).

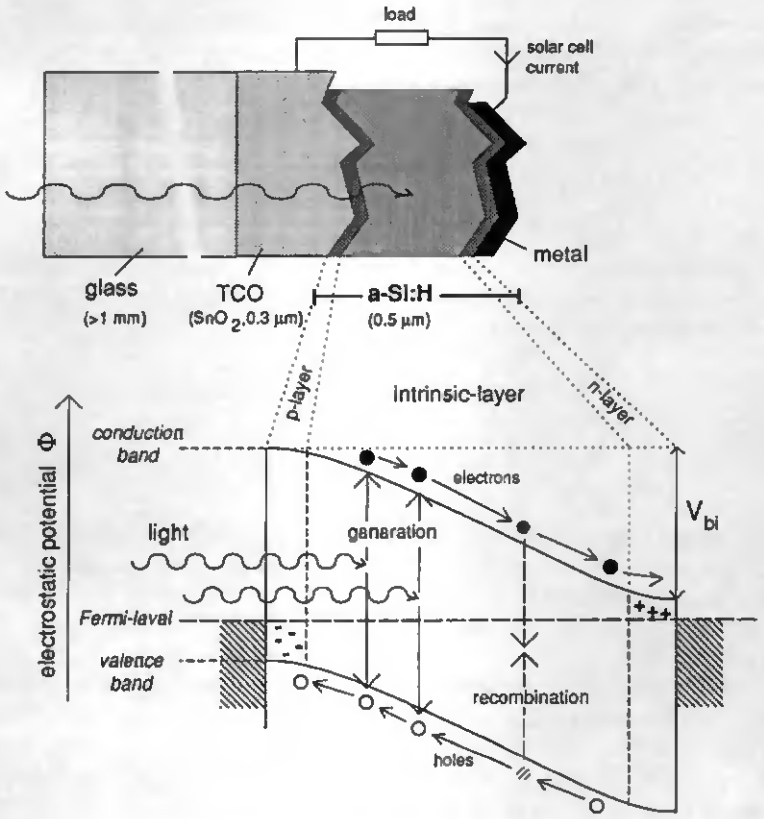

Figure 2.3: Schematic physical structure (top), and schematic band-diagram and photocarrier collection (bottom) in an a-Si:H p-i-n solar cell.

In the highly doped p- and n-layer of a-Si:H p-i-n solar cells virtually all photocarriers are lost because of an even increased recombination as compared to intrinsic a-Si:H material, i.e. these layers are 'photovoltaically dead'. The thickness of the doped layers is therefore reduced to the minimum needed to form the barrier; this thickness is of the order of 100 - 200 Å. But even such very thin, non-active layers cause significant current losses, specially in the doped layer at the illuminated surface, where the generation rate is very high (see Figure 2.2). To further reduce those losses, low absorption silicon-carbon window layers are typically employed as p-layers (see section 2.3.2).

2.1.3 Basic transport equations

The carrier transport in amorphous silicon devices can be described by the five general semiconductor equations. They include the Poisson's equation

$$\frac{dE(x)}{dx} = \frac{q}{\varepsilon_r \varepsilon_0} \cdot (p(x) - n(x) + Q(x, p(x), n(x))) \tag{2.3}$$

relating the derivative of the electrical field E to the local charge (free electrons n, free holes p, and space-charge Q), the current density equations, combining the two driving forces of carrier movement, the drift and the diffusion, to the total hole (j_p) and electron (j_n) currents

$$j_p(x) = q\mu_p p(x)E(x) - kT\mu_p \frac{dp(x)}{dx} \tag{2.4}$$

$$j_n(x) = q\mu_n n(x)E(x) + kT\mu_n \frac{dn(x)}{dx} \tag{2.5}$$

and the two continuity equations, assuring the conservation of the total number of electrons and holes in the described system (the local spatial derivative of the currents is proportional to the local difference generation and recombination)

$$\frac{dj_p(x)}{dx} = q \cdot (G(x) - R(p,n,x)) \tag{2.6}$$

$$-\frac{dj_n(x)}{dx} = q \cdot (G(x) - R(p,n,x)) \tag{2.7}$$

This set of equations defines a system of five coupled, first-order differential equations for the local variables n, p, j_n, j_p, and E. The set of equations does not have a general analytical solution, because of the non-linearity introduced by the product terms $p(x)\cdot E(x)$ and $n(x)\cdot E(x)$ in the current density equations (Eqns. 2.4 and 2.5). Also the space-charge Q, and the recombination R, are in a-Si:H typically non-linear functions of n and p (see model for the gap-states, section 2.1.5). In the present work, numerical solutions are obtained by discretising the differential equations (to difference equations) and by solving the resulting system of linear, algebraic equations with standard numerical techniques.

Eqns. 2.3 to 2.7 describe the transport in a one-dimensional device. Possible multi-dimensional effects due to e.g. the roughness of the solar cell substrate (Fig. 2.3) are thus not considered in the following considerations.

2.1.4 Modelling range and boundary conditions

To model the actual p-i-n solar cell device, one has to define the range over which the transport equations shall be solved. Different concepts have been used in the past (see [ARC91]). Especially the question of how to treat the doped layers has been debated. In the present work the transport equations are solved only within the intrinsic layer, and boundary conditions defined at the doped-layer/intrinsic-layer interfaces.

This focus on the i-layer is justified as all experimental evidence indicates that the doped layers indeed are photovoltaically non-active, with the light absorbed in the doped layer not contributing to the photo current, not even when the electrical field in the doped layers is increased by reverse bias voltage (see Figure 2.12). Also, the photovoltaic conversion in the active part of the solar cell is found to be independent of the doped layer thickness, once the necessary thickness to form the barrier has been reached (Figure 2.33, left). But there is a further, more pragmatic reason to choose boundary conditions at the limits of the i-layer only: The basic problem with modelling of amorphous silicon is that many material parameter values are not precisely known. Even basic material parameters, such as the carrier mobilities, are only approximately known, and their exact values remain a matter of scientific debate. Doped materials, as used in p- and n-layer of the p-i-n solar cell, are thought to have quite different material parameters than those of the intrinsic layer [BEY84, STR91], but they are known to an even lesser degree. With the in-depth modelling of the doped layers, the number of ill-defined parameter is tripled, jeopardising the transparency of the model. If on the other hand only the i-layer is modelled, the doped layer influence is completely described by only five i-layer boundary condition parameters, making the modelling attempts much more concise.

Built-in potential

The boundary condition with the most obvious influence on the modelled p-i-n solar cell behaviour is the built-in potential V_{bi}. The built-in potential represents the difference of the electrostatical potential between the p-layer and the n-layer material, or the height of the internal barrier. If an external voltage V_{ext} is applied to the solar cell, it is deducted from the built-in voltage.

$$V_{bi} - V_{ext} = \int_{x=0}^{\infty} E(x)dx \tag{2.8}$$

The built-in potential in a-Si:H solar cells is generally assumed to be close to 1.1 V. The difference with respect to the bandgap of amorphous silicon (1.7 - 1.8 eV) is lost in form of the remaining energy differences between the band-edges and Fermi-level positions in the doped layers (see Figure 2.3). The same boundary condition is typically also applied in models that include the doped layers [ARC90]. Because in the present case the full built-in voltage is assumed to be applied over the i-layer alone, the part of the potential lost in the doped layer space-charge regions is neglected. But it can be easily shown that these potential drops are very small with respect to the total built-in potential (approx. 10 mV in each doped layer).

Interface recombination currents

The additional 4 boundary conditions define the current densities at the interfaces x = 0 and x = L. In general they have the form

$$j_p(0) = - q S_{p0} (p_{equ}(0)-p(0)) \quad (2.9)$$

$$j_p(L) = q S_{pL} (p(L)-p_{equ}(L)) \quad (2.10)$$

$$j_n(0) = q S_{n0} (n(0)-n_{equ}(0)) \quad (2.11)$$

$$j_n(L) = -q S_{nL} (n_{equ}(L)-n(L)) \quad (2.12)$$

where S_{yx} is the interface recombination velocity of the carrier y at the interface x, and $y_{equ}(x)$ is the thermal equilibrium density of the carrier y at the interface x [FON81, ARC90].
For the present case where the boundaries are defined at the doped layer/intrinsic layer interfaces, these equations can be further simplified. In the equations for the minority carrier currents $j_p(L)$ and $j_n(0)$, the respective thermal equilibrium electron and hole densities can be omitted, as they are much smaller than the corresponding carrier densities under illumination.

$$j_p(L) = q S_{pL} p(L) \quad (2.13)$$

$$j_n(0) = q S_{n0} n(0) \quad (2.14)$$

Making this simplification allows only for true interface recombination loss currents, i.e. that the minority carriers recombine at the interface, and that no minority carriers can leave the doped layers, corresponding to the above assumption of photovoltaically inactive doped layers. The S values reflect the degree of interface passivation, or in other words the recombination strength of the interface. S values in the range of 10^3 - 10^5 cm/s were found to give a good fit to the measured p- and n-side collection efficiencies, and the solar cell open circuit voltage. These values are below the upper limit given by the thermal velocity of 10^7 cm/s, and thus indicate a relatively good interface passivation.
The boundary conditions for the respective majority carriers (Eqns. 2.9 and 2.12) can also be simplified. For majority carriers, the interfaces behave as ohmic contacts, and the corresponding S values are very high [FON81]. Considering the maximal amplitudes of the majority carrier currents flowing through these contacts under solar cell operation conditions, and the equilibrium carrier densities in the doped layers (see below), the relative change of the majority carrier density at the interface caused by the current flow remains negligible. This allows then to simply assume a constant majority carrier concentration that is independent of the current density:

$$p(0) = p_{equ}(0) = \text{constant} \quad (2.15)$$

$$n(L) = n_{equ}(L) = \text{constant} \quad (2.16)$$

The values for these majority carrier densities can be estimated from the conductivities of the doped layers. For a conductivity of $10^{-5}\,\Omega^{-1}\text{cm}^{-1}$ for the p-layer (see section 2.3.2), and $10^{-2}\,\Omega^{-1}\text{cm}^{-1}$ for n-layer bulk material, with mobilities of 1 cm^2/Vs for holes and 10 cm^2/Vs for electrons, one obtains the respective carrier densities $p_{equ}(0)=10^{14}\ \text{cm}^{-3}$ and $n_{equ}(L)=10^{16}\,\text{cm}^{-3}$.
The majority carrier concentrations at the interfaces influence the modelled solar cell behaviour through the out-diffusion of majority carriers into the i-layer. For example in a simplified case in

which the electric field E is assumed constant, and the recombination is neglected, the distribution of the out-diffusing carriers is exponential, with a characteristic depth kT/qE. As the shape of the tail originates from a balance of drift and diffusion, its characteristic depth is independent of the carrier mobility.

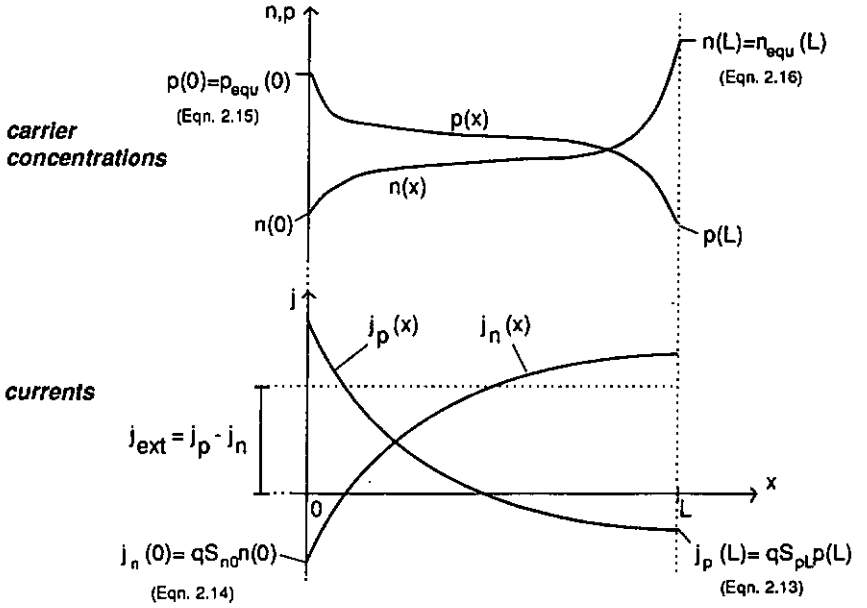

Figure 2.4: Carrier concentrations (top) and currents (bottom) of electrons and holes, coupled by the 4 boundary conditions (Eqn. 2.13-2.16) at the intrinsic layer interfaces (x=0 is the p-i interface, x=L the n-i interface).

At high electric fields, the majority carrier tails can only influence the i-layer carrier concentrations in the close vicinity of the doped layers (small characteristic length of outdiffusion, as in Figure 2.4). With increasing forward voltage the electric field is reduced until the majority carriers diffuse through the whole i-layer to reach the opposite interfaces. The carriers are there lost by interface recombination, constituting a current of the opposite sign of the active photocurrent. The sharp onset of this current at high forward voltage determines the open-circuit voltage V_{oc} (or rather the difference between V_{oc} and V_{bi}). For a given built-in potential V_{bi}, the modelled V_{oc} thus depends on both the doped layer majority carrier density on one side, and the effectiveness of the interface recombination (S) at the opposite doped layer interface. The increase of either the majority carrier density or the recombination velocity increases the current flow, and correspondingly decreases the V_{oc}.

With the above assumed higher majority carrier concentrations at the n-layer interface, it is the onset of the electron injected current that determines the V_{oc} in the present model. Experimental studies on the effects of p-i interface buffer-layers seem to confirm this description of the V_{oc} being governed by electron injection and p-i interface recombination [SAK89].

The above way to define the boundary conditions at the i-layer interfaces, and not to model in depth the doped layers, has been criticised in a recent publication [RUB92]. In that study, a numerical p-i-n solar cell model including the doped layers was employed to calculate the apparent

recombination velocities S at the doped layer/i-layer interfaces. As a result, the apparent S values were found to strongly vary as a function of the voltage applied to the solar cell, seemingly contradicting the constant S values assumed in this work. But the analysis of the cited model reveals that those changes of the S values are due to a sign change of the interface minority carrier flow from recombination to carrier extraction, as the internal voltage increases (reverse bias). This sign change is equivalent to minority carrier collection from the doped layers, a behaviour that does not agree with the experimental findings of 'photovoltaically dead' doped layers. In this view, the cited results can thus definitely not invalidate our simplified model, which in fact explicitly excludes collection from the doped layers.

2.1.5 Model of the gap states

In addition to the doped layer boundary conditions, the behaviour of an amorphous silicon p-i-n solar cell is determined by the properties of the intrinsic layer material. The key characteristics of amorphous silicon materials arise from a high density of localised states in the forbidden gap. These states influence the solar cell behaviour in two ways: by trapping free carriers, they accumulate charge that determines the electric field distribution in the i-layer (Eqn. 2.3), and secondly they represent the pathway for the photocarrier recombination, the process that directly competes with the collection of the photocarriers (see Eqns. 2.6 and 2.7).
The exploration, characterisation, and modelling of the localised gap-states in amorphous silicon has been the object of a vast research effort. But as the amorphous network allows for a continuous distribution of different kinds of states over the whole energy-gap, it has proven extremely difficult to identify the exact nature of all of these states. Correspondingly, a variety of different gap-state models are currently under consideration. The gap-state models used in the present work represent a particular choice among the various approaches proposed in the literature. Again, an attempt was made to apply the most simple concepts to allow for a maximal modelling transparency.
Typically, three classes of localised states are distinguished: dangling-bond states, band-tail states, and dopant/impurity states. Figure 2.5 shows the schematic distribution of these states in the gap.

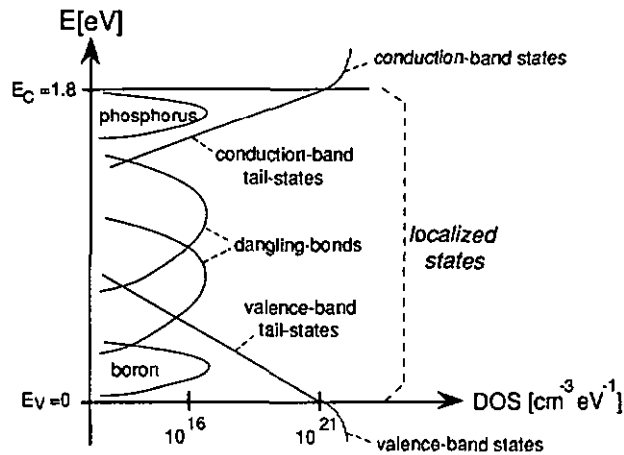

Figure 2.5: Schematic distribution of the localised and extended electronic states in hydrogenated amorphous silicon.

Dangling bond states

Non-terminated, free silicon bonds, known as dangling-bonds, generate localised states with energy levels near the middle of the gap. These dangling-bonds are normally occupied by one electron, and neutral, but they can either capture a second electron and become negatively charged, or they may loose the electron (capture a hole) and become positively charged. With their energy level near mid-gap, probability of re-emission of a captured carrier from a dangling-bond is low, making these states very effective recombination centres.

The results from materials investigations, as well as the measurement of p-i-n solar cells (see chapter 3) show evidence of both negatively and positively charged dangling-bonds. It is however unclear whether one kind of defect state can take all three occupations (negative/neutral/positive = amphoteric states) [VAI86], or whether two classes of dangling-bonds favour each only two of the three possible occupations (neutral/negative: acceptor-like states, and neutral/positive: donor-like states) [LEE91]. For the sake of simplicity, a model with amphoteric states was chosen for the present work [VAI86]. The use of a model employing two classes of defects leads to an additional modelling parameter, because then the total densities of both kinds of defects have to be specified [KOP92]. In the adopted model, a possible distribution of the dangling-bond states in energy is also neglected, leading to a further parameter reduction. The doubly occupied state D^- is assumed to be offset from the energy of the single occupied state D^0 by the correlation energy E_U. Figure 2.6 shows the different transitions between the free carriers and the dangling-bond states.

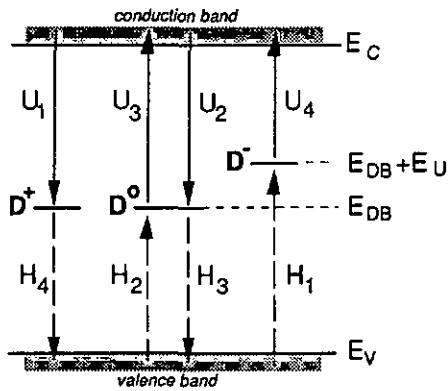

Figure 2.6: Schematic representation of the transitions between the free carriers (extended states) and the dangling-bond states D^+, D^0, D^-. The full arrows are electron transitions, the broken arrows are hole transitions.

The transitions are linked to the concentrations of the free carriers, and to the occupation of the dangling-bonds by the capture and emission rates (Shockley-Read expressions)

$$\begin{aligned} U_1 &= N_{DB} f^+ c_n^+ & H_1 &= N_{DB} f^- c_p^- \\ U_2 &= N_{DB} f^0 c_n^0 & H_2 &= N_{DB} f^0 c_p^0 \\ U_3 &= N_{DB} f^0 e_n^0 & H_3 &= N_{DB} f^0 e_p^0 \\ U_4 &= N_{DB} f^- e_n^- & H_4 &= N_{DB} f^+ e_p^+ \end{aligned} \qquad (2.17)$$

$U_{1,2,3,4}$ are electron transitions, $H_{1,2,3,4}$ are hole transitions. The capture rates c and emission rates e are as follows:

$$\begin{aligned} c_n^+ &= n v_{th} \sigma_n^+ & e_n^0 &= \frac{1}{2} N_C v_{th} \sigma_n^+ \exp\left(\frac{E_{DB} - E_C}{kT}\right) \\ c_n^0 &= n v_{th} \sigma_n^0 & e_n^- &= 2 N_C v_{th} \sigma_n^0 \exp\left(\frac{E_{DB} + E_U - E_C}{kT}\right) \\ c_p^- &= p v_{th} \sigma_p^- & e_p^0 &= \frac{1}{2} N_V v_{th} \sigma_p^- \exp\left(\frac{E_V - (E_{DB} + E_U)}{kT}\right) \\ c_p^0 &= p v_{th} \sigma_p^0 & e_p^+ &= 2 N_V v_{th} \sigma_p^0 \exp\left(\frac{E_V - E_{DB}}{kT}\right) \end{aligned} \tag{2.18}$$

The capture rates are straight forward. The emission rates are formally the same as for a simple two-state defect [TAY72], except the factors 1/2 and 2 that arise from thermal equilibrium occupation considerations of the amphoteric dangling-bond defects [VAI86]. In the present work, it shall further only be distinguished between the cross section of charged and un-charged states, but not between electron and hole capture. The 4 cross sections in Eqn. 2.18 are then represented by the two parameters

$$\sigma_{DB}^0 = \sigma_n^0 = \sigma_p^0 \tag{2.19}$$

$$C = \frac{\sigma_p^-}{\sigma_p^0} = \frac{\sigma_n^+}{\sigma_n^0} \tag{2.20}$$

The steady state conditions require that no charge be accumulated, neither in the dangling-bonds as a whole, nor in any single one of their occupation states (here in D^+):

$$U_1 + U_2 - U_3 - U_4 = H_1 + H_2 - H_3 - H_4 \tag{2.21}$$

$$U_1 - U_3 + H_4 - H_2 = 0 \tag{2.22}$$

Using

$$f^- + f^0 + f^+ = 1 \tag{2.23}$$

the occupation f^-, f^0, f^+ of the three dangling-bond states can be determined as a function of the free carrier densities n and p from Eqns. 2.17 and 2.19-2.21:

$$f^+ = \frac{1}{1 + a + a/b} \qquad f^0 = \frac{1}{1 + 1/b + 1/a} \qquad f^- = \frac{1}{1 + b + b/a} \tag{2.24}$$

with

$$a = \frac{c_n^+ + e_p^+}{c_p^0 + e_n^0} \qquad b = \frac{c_p^- + e_n^-}{c_n^0 + e_p^0} \tag{2.25}$$

The total dangling-bond charge Q_{DB}, and the total dangling-bond recombination R_{DB}, to be used in the solar cell transport equations, are

$$Q_{DB} = N_{DB} (f^+ - f^-) \tag{2.26}$$

$$\begin{aligned} R_{DB} &= U_1 + U_2 - U_3 - U_4 \ (= H_1 + H_2 - H_3 - H_4) \\ &= N_{DB} f^0 \left[\frac{c_n^+}{a} + c_n^0 - e_n^0 - \frac{e_n^-}{b} \right] \end{aligned} \tag{2.27}$$

Under illumination, the emission rates from states in the centre of the gap are small with respect to the capture rates. Consequently, it is the density and the capture cross sections of the dangling-bonds that are the main modelling parameters of the illuminated solar cell behaviour, whereas the parameters related to the energetical position of the dangling-bonds have virtually no influence; to model the illuminated solar cell behaviour, it is thus justified to neglect distribution in energy of the defect levels.

Band-tail states

The band-tail states are thought to originate from distorted covalent silicon-silicon bonds in the amorphous network. Normally these bonds are occupied by two electrons, and thus neutral. Depending on their kind of distortion, the bonds are predisposed to either capture a third electron, or to lose one of their electrons (i.e. to capture a hole). The bonds that capture an (excess) electron are energetically similar to an extended state in the conduction-band, and they are referred to as conduction-band tail-states, whereas the bonds that capture holes are energetically close to the valence-band, and thus referred to as valence-band tail-states. The energy levels of the tail-states are shallow with respective to the band-edges. Therefore, thermal re-emission rates are high.
The amorphous network requires that a range of distorted Si-Si bonds be present, and correspondingly the tail-states are distributed in energy. The concentration of states is thought to decrease rapidly with decreasing energy level below the band-edge, i.e. there are many shallow states, and very few deep states. Typically, the density of the tail-states is taken to decrease exponentially as a function of energy, with a characteristic energy E_{0C} for the conduction-band tail, and E_{0V} for the valence-band tail.

$$N_{CBT}(E) = N_{CBT0}\exp(\frac{E_C - E}{E_{0C}}) \tag{2.28}$$

$$N_{VBT}(E) = N_{VBT0}\exp(\frac{E - E_V}{E_{0V}}) \tag{2.29}$$

The total density of states at the valence band side is found to be much higher than the one on the conduction band side, the characteristic energies being as follows: $E_{0V} \approx 50$ meV and $E_{0C} \approx 30$ meV.
It will be shown later in this work that over the range of i-layer thicknesses and illumination intensities that are used for a-Si:H solar cells, the space-charge and the recombination associated with the tail-states can typically be neglected (chapter 3). This is because for the free carrier densities found under sun-light illumination, there are not enough occupied tail-states to yield a sizeable space-charge or a recombination intensity comparable to that of the dangling-bonds. However, under high light-intensity, and in solar cells with very thick i-layers, the tails can significantly influence the solar cell behaviour (see section 3.2.3). Furthermore, the tail-state considerations are necessary in order to model the effect of the dopants (see below, and chapter 4).
As indicated above, the band-tail states are considered to have only two charge states. Their occupation f (fullness) thus obeys the Shockley-Read statistics of a level at the energy E_t

$$f = \frac{c_n + e_p}{c_n + c_p + e_n + e_p} \tag{2.30}$$

with the respective capture and emission rates of electrons and holes

$$c_n = n\, v_{th}\sigma_n \qquad e_n = v_{th}\sigma_n N_C \exp\left(\frac{E_t - E_C}{kT}\right) \tag{2.31}$$

$$c_p = p\, v_{th}\sigma_p \qquad e_p = v_{th}\sigma_p N_V \exp\left(\frac{E_V - E_t}{kT}\right)$$

Different from the case of the dangling-bonds, the modelling of the tail-states requires that the detailed energy level distribution be taken into account. This is because the net influence of the tail-states is the product of the two strongly varying quantities of an increasing number of states, and a sharply decreasing occupation of these states. This particular behaviour can not be modelled by concentrating a fixed number of states at one single energy level. Normally, the Shockley-Read statistics have to be numerically integrated over the whole distribution of the tails [ARC91, KOP92]. Alternatively, approximate analytical solutions can be found, based on the concepts of Taylor and Simmons [TAY72]. In the following, such a solution is developed for the conduction-band tail.

The occupation f(E) (Eqn. 2.30) of a continuous distribution of states is approximated in three energy ranges:

$$E > E_{tn}: \qquad f(E) = 0 \tag{2.32}$$

$$E_{tn} > E > E_{tp}: \qquad f(E) = \frac{c_n}{c_n + c_p} \tag{2.33}$$

$$E < E_{tp}: \qquad f(E) = 1 \tag{2.34}$$

with the characteristic energies

$$E_{tn} = E_{FN} + kT\ln\left(\frac{c_n + c_p}{c_n}\right) \qquad E_{tp} = E_{FP} - kT\ln\left(\frac{c_n + c_p}{c_n}\right) \tag{2.35}$$

based on the pseudo Fermi-levels for electrons and holes

$$E_{FN} = E_C + kT\ln\left(\frac{n}{N_C}\right) \qquad E_{FP} = E_V - kT\ln\left(\frac{p}{N_V}\right) \tag{2.36}$$

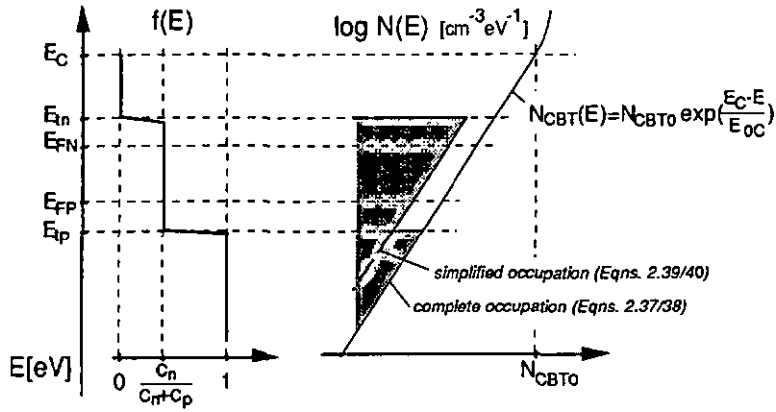

Figure 2.7: Approximated occupation function for electrons f(E) under non-equilibrium condition (under illumination) according to Taylor and Simmons [TAY72], and its influence on the occupation of the conduction-band tail.

The total conduction-band charge density is then the integrated product of the occupation function times the density of conduction-band states

$$Q_{CBT} = \int_{E_V}^{E_C} f(E) N_{CBT}(E) dE = \int_{E_V}^{E_\varphi} N_{CBT}(E) dE + \frac{c_n}{c_n + c_p} \int_{E_\varphi}^{E_m} N_{CBT}(E) dE \tag{2.37}$$

and the total conduction-band recombination is equal to the total charge between the two characteristic energies E_{tn} and E_{tp} times the capture rate for holes c_p

$$R_{CBT} = \frac{c_n c_p}{c_n + c_p} \int_{E_{tp}}^{E_{tn}} N_{CBT}(E) dE \tag{2.38}$$

For the case of an illuminated solar cell, the characteristic energies E_{tn} and E_{tp} are always separated to an extent that the contribution of the states below E_{tp} can be neglected (Figure 2.7, simplified occupation). This allows to further simplify the expressions

$$Q_{CBT} = \frac{c_n}{c_n + c_p} \int_{-\infty}^{E_{tp}} N_{CBT}(E)\, dE = N_{CBT0}\, E_{0C} \left[\frac{c_n}{c_n + c_p}\right]^{1-\frac{kT}{E_{oc}}} \left[\frac{n}{N_C}\right]^{\frac{kT}{E_{oc}}} \tag{2.39}$$

$$R_{CBT} = \frac{c_n c_p}{c_n + c_p} \int_{-\infty}^{E_{tp}} N_{CBT}(E)\, dE = N_{CBT0}\, E_{0C}\, c_p \left[\frac{c_n}{c_n + c_p}\right]^{1-\frac{kT}{E_{oc}}} \left[\frac{n}{N_C}\right]^{\frac{kT}{E_{oc}}} \tag{2.40}$$

The charge and recombination of the valence-band tail are obtained in the same way

$$Q_{VBT} = \frac{c_p}{c_n + c_p} \int_{E_{tp}}^{\infty} N_{VBT}(E)\, dE = N_{VBT0}\, E_{0V} \left[\frac{c_p}{c_n + c_p}\right]^{1-\frac{kT}{E_{ov}}} \left[\frac{p}{N_V}\right]^{\frac{kT}{E_{ov}}} \tag{2.41}$$

$$R_{VBT} = \frac{c_n c_p}{c_n + c_p} \int_{E_{tn}}^{\infty} N_{VBT}(E)\, dE = N_{VBT0}\, E_{0V}\, c_n \left[\frac{c_p}{c_n + c_p}\right]^{1-\frac{kT}{E_{ov}}} \left[\frac{p}{N_V}\right]^{\frac{kT}{E_{ov}}} \tag{2.42}$$

The above equations only hold if the characteristic energies of the tails (E_{0C}, E_{0V}) are larger than the thermal energy kT. For steeper density of states distributions, the Taylor-Simmons approximation is no more physically meaningful, and the occupations have to be numerically integrated [VAI86].

The expressions developed here for the tail-state charge and recombination are very similar to analytical solutions presented elsewhere [VAI86, HUB93]. The slight differences of Eqn. 2.39-2.42 with respect to those solutions arise from the different treatment of the boundary conditions towards the middle of the gap. But these boundary conditions are only significant if the two pseudo Fermi-levels are close together, i.e. in the case of very low illuminations.

In one of the cited investigations [HUB93], an additional occupation of the tail-states in the regions $E > E_{tn}$, and $E < E_{tp}$ was considered (in the above model, zero occupation was assumed in these ranges (Eqn. 2.32)). But as the thus considered additional occupation is just located very near the critical characteristic energy, it seems that the influence of these additional 'trap-states' will stay within the general errors of the Taylor-Simmons approximation itself. This view is indirectly

confirmed by the fact that the expressions found for those 'trap-states' are formally almost identical with the above expressions (Eqns. 2.39 and 2.41).

Dopant states

The fact that a-Si:H is easily doped with boron (p-type) and phosphorus (n-type) requires the existence of corresponding dopant-states. The 4-fold coordinated phosphorus atom is expected to introduce a state between mid-gap and the conduction-band, positively charged when empty, and neutral if occupied by an electron. Correspondingly, one expects a boron state between mid-gap and the valence band, in its empty state negatively charged, and neutral when occupied by a hole.
There is no general agreement as to the detailed distribution and energy levels of the dopant states. This is because they are hidden under the large densities of tail-states present in the region of the band-edges, and therefore difficult to measure.
Experimentally, the doping can be used to control the Fermi-level over a wide range. At high doping concentrations the doping effect becomes increasingly inefficient, and eventually the Fermi-level cannot be moved closer to the band-edge. The saturation has been attributed to the Fermi-level entering the sharply increasing density of states in the band-tails [STR91]. In this model, it is the increasing band-tail charge that compensates the ionised dopants. The fact that n-type doping yields higher peak conductivities than p-type doping is then explained by the narrower band-tail at the conduction-band. Alternatively, the saturation of the Fermi-level could be interpreted as the energy-levels of the dopant-states being deep in the gap.
In the present solar cell model, the simulation of dopants is restricted to the simulation of very low level doping in the intrinsic layer of the solar cell (chapter 4). The dopant states are considered to be close to the band-edges, and thus always ionised. The total dopant charge is

$$Q_{DOP} = N_D - N_A \tag{2.43}$$

With the dopants always ionised, the dopant charge is not neutralised by dopant occupation if the Fermi-level approaches the band-edge. But a suitable neutralisation effect is achieved by the simultaneous simulation of the band-tails (see section 4.2.1).
The doping of amorphous silicon was also found to influence the defects at mid-gap. With increasing doping levels, additional defects are detected at mid-gap [STR82, STR91]. However, for the very low-level doped materials investigated by this work, it will be shown that it is reasonable to neglect this effect (to be discussed in chapter 4).

Finally, the total space charge density and total recombination of all gap states to be used in the transport equations (Eqns. 2.3, 2.6, and 2.7) are

$$Q(x,n,p) = Q_{DB} + Q_{VBT} - Q_{CBT} + Q_{DOP} \tag{2.44}$$

$$R(x,n,p) = R_{DB} + R_{VBT} + R_{CBT} \tag{2.45}$$

The dependencies in x indicate the possibility to model spatially varying material properties within the thickness of the i-layer.

2.1.6 Modelling parameters and modelling operation

The complete set of modelling parameters of the p-i-n solar cell model is given in Table 2.I. Also, the standard set of numerical values used in the present work are given there (to be referred to as to the 'standard modelling parameters'). Most of the parameters will be kept constant for all modelling cases. The modelling parameters to be varied in the course of this work are specially marked in Table 2.I.

Variations of the solar cell modelling parameters, and of the solar cell operating conditions yield the desired understanding of the solar cell operation. The solar cell operating conditions include the illumination spectrum and intensity as well as the external voltage applied. The illumination is represented by the photocarrier generation rate G(x) in the intrinsic layer, calculated from absorption and the illumination spectrum. Besides the internal variables (n(x), p(x), $j_n(x)$, $j_p(x)$, E(x), or the quantities derived from these), each operation condition yields an external solar cell current j_{ext}. This current can be determined at any i-layer location x_0, by taking the difference between the hole and the electron currents (see Figure 2.4)

$$j_{ext} = j_p(x_0) - j_n(x_0) \tag{2.46}$$

The calculation of j_{ext} as a function of varying operation conditions is the basis for the simulation of the 'external' solar cell behaviour, i.e. current-voltage curve JV, spectral response SR, and dynamic inner collection efficiency DICE (see chapter 2.2).

Table 2.1: Modelling parameters (the listed numerical values are referred to as to the 'standard modelling parameters' in the text)

(intrinsic layer material parameters)			
ε_r	[-]	11.7	relative dielectric permitivity
v_{th}	[cms^{-1}]	10^7	thermal velocity
μ_n*	[cm^{2}V^{-1}s^{-1}]	10	electron mobility
μ_p*	[cm^{2}V^{-1}s^{-1}]	1	hole mobility
E_C	[eV]	1.8	energy of the conduction-band edge
E_V	[eV]	0	energy of the valence-band edge
N_C	[cm^{-3}]	$3\cdot10^{21}$	effective density of states in the conduction-band
N_V	[cm^{-3}]	$3\cdot10^{21}$	effective density of states in the valence-band
E_{DB}	[eV]	0.8	energy of the D^+/D^0 dangling-bond state
E_U	[eV]	0.3	correlation energy ($E(D^-)$-E_{DB})
σ^0_{DB}	[cm^2]	10^{-15}	cross section of the neutral dangling-bond state
C^*	[-]	10	cross section ratio of the dangling-bond state (charged/neutral)
N_{DB}*	[cm^{-3}]	10^{15}	dangling-bond density
N_{CBT0}†	[cm^{-3}eV^{-1}]	$3\cdot10^{21}$	density of states at the conduction-band edge
N_{VBT0}*,†	[cm^{-3}eV^{-1}]	$3\cdot10^{21}$	density of states at the valence-band edge
E_{0C}†	[meV]	30	characteristic energy of the conduction-band tail-states
E_{0V}†	[meV]	45	characteristic energy of the valence-band tail-states
σ_n^{CBT}†	[cm^2]	10^{-15}	cross section of the conduction-band tail-states for electrons
σ_p^{CBT}†	[cm^2]	10^{-14}	cross section of the conduction-band tail-states for holes
σ_p^{VBT}†	[cm^2]	10^{-14}	cross section of the valence-band tail-states for electrons
σ_n^{VBT}†	[cm^2]	10^{-15}	cross section of the valence-band tail-states for holes
N_A*	[cm^{-3}]	0	density of ionised acceptors
N_D	[cm^{-3}]	0	density of ionised donors
(intrinsic layer boundary conditions)			
V_{bi}	[V]	1.1	built-in potential
S_{n0}	[cms^{-1}]	$3\cdot10^4$	surface recombination velocity for electrons at the p-i interface
S_{pL}	[cms^{-1}]	$3\cdot10^3$	surface recombination velocity for holes at the n-i interface
$p_{equ}(0)$	[cm^{-3}]	10^{14}	equilibrium hole density at the p-i interface
$n_{equ}(L)$	[cm^{-3}]	10^{16}	equilibrium electron density at the n-i interface
L	[µm]	0.5	intrinsic layer thickness

*: modelling parameters to be changed in the course of this work

†: for some simulations, the tail-states are not modelled

2.2 Device characterisation

A sensible device characterisation is essential for successful development and optimisation of solar cells. Beyond the mere measurement of the actual photovoltaic performance, it is through the detailed analysis of the completed solar cell device alone that the effects of design and material variations can be assessed, that the different loss mechanisms can be analysed, and that the solar cell models can be improved and verified.
Many solar cell characterisation methods were originally devised for crystalline silicon solar cells. Later, many of these methods were also applied to other solar cell technologies. But often it was overlooked that some methods are very specific to a given technology, and yield ambiguous or erroneous results if applied to another technology. Some of these problems have also 'haunted' amorphous silicon solar cells (e.g. dark current analysis, surface photovoltage, diffusion- and collection length measurements).
In the following sections, different issues of amorphous silicon solar cell characterisation are addressed. A set of characterisation methods is presented and discussed that is judged to be well suited to amorphous silicon p-i-n solar cells, and that will be later applied in chapter 3 and 4.

2.2.1 Current-voltage curve

The measurement of the current-voltage (JV) curve under illumination is the most basic solar cell measurement. A schematic JV-curve of an amorphous silicon p-i-n solar cell under illumination is given in Figure 2.8.

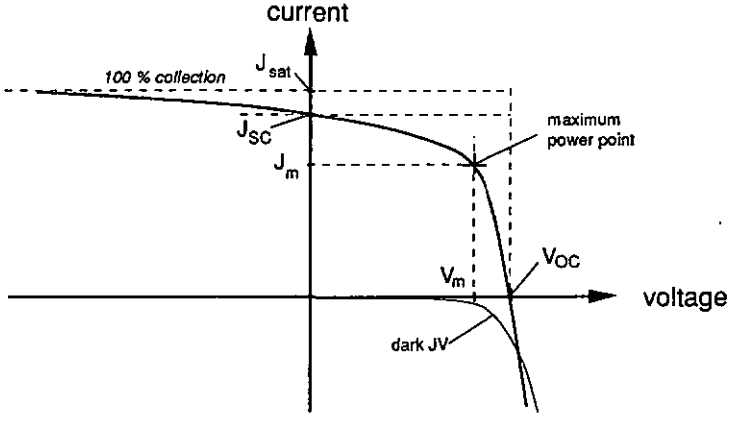

Figure 2.8: Schematic illuminated JV-curve of an amorphous silicon p-i-n solar cell. The cross marks the maximum-power-point.

The JV-curve measurement allows to determine the electric power output of a solar cell, the main parameter of interest to any solar cell development effort. The solar cell efficiency η is derived by dividing the maximum electrical power output density P_m by the intensity of the incident light I_{light}:

$$\eta = \frac{P_m}{I_{light}} = \frac{J_m \cdot V_m}{I_{light}} \tag{2.47}$$

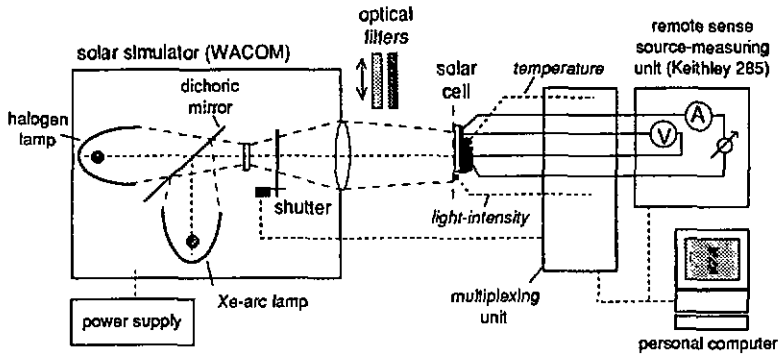

Figure 2.9: Schematic JV set-up used for the present work, including a WACOM 2-source AM1.5 solar simulator, and computer controlled 4-wire JV measurement.

The specification of an efficiency must always be related to an illumination with a defined spectral distribution and to a defined temperature. As standard conditions to determine the efficiency of solar cells for terrestrial use, the AM1.5 solar spectrum at 100 mW/cm^2 ([MAT84], see Figure 2.1) and a solar cell temperature of 25°C is most accepted. Figure 2.9 shows the schematic set-up used for JV-measurements of this work.

Fill factor, and saturated fill factor

Besides the determination of the maximal power output, the JV-curve is used to determine open-circuit voltage V_{oc} and the short-circuit current J_{sc} (see Figure 2.8). The relation of the product of those two parameters to the maximum power output defines the solar cell fill factor FF:

$$FF = \frac{P_m}{J_{sc} \cdot V_{oc}} = \frac{J_m \cdot V_m}{J_{sc} \cdot V_{oc}} \qquad (2.48a)$$

In amorphous silicon solar cells, the fill factor FF of the JV-curve has often been regarded as a measure of the quality of the intrinsic layer [FAU84, KAL89]. But by its definition the value of the fill factor is intrinsically connected to the amplitude of the short-circuit current (J_{sc}), which in a-Si:H solar cells is a complex function of both the totally generated photo current and also the voltage dependent collection within the i-layer. Due to its dependence on J_{sc}, the quantity of the fill factor can thus be completely uncorrelated with the quality of the i-layer (e.g. can a-Si:H p-i-n cells have very high fill factors even if the photocarriers of large sections of the i-layer are not collected at all (see Figure 4.5)).
For amorphous silicon p-i-n solar cells, a much less ambiguous definition of the fill factor is found if the maximum power point is not related to the current at short-circuit, but to the saturated current (J_{sat}):

$$FF_{sat} = \frac{J_m \cdot V_m}{J_{sat} \cdot V_{OC}} \quad (= \frac{J_{SC}}{J_{sat}} \cdot FF) \qquad (2.48b)$$

The saturated current J_{sat} is defined as the current which is asymptotically approached while increasing the reverse voltage (see Figure 2.8). The hypothesis is that the saturated current

corresponds to the complete collection of all photo-generated carriers generated in the i-layer of the p-i-n solar cell. For practical devices, it cannot be proven whether such a saturated current actually exists. But the results from a vast number of measurements of many different amorphous silicon p-i-n solar cells (degraded, low-level doped; see e.g. Figures 3.3/4.5) all show a pronounced saturation behaviour of the currents at reverse voltages. Only for very severe collection problems the reverse voltage break-down might prohibit the application of a high enough voltage.
The thus defined 'saturated fill factor' FF_{sat} (Eqn. 2.48b) seems to be a more reasonable photovoltaic parameter, relating to the fraction of the maximal possible photo current that is actually collected at the maximal power point independently of the detailed current amplitude at short-circuit. This is illustrated in Figure 3.5, showing a very good scaling of the FF_{sat} with the p-i-n solar cell efficiency during a light-soaking experiment.

Dark JV- curve

For crystalline solar cells, the dark JV-curve yields substantial insights into the solar cell operation (determination of the recombination mechanism, etc.). In amorphous silicon p-i-n solar cells, differently from crystalline silicon solar cells, the dark and illuminated curves intersect at forward voltages (Figure 2.10). The decrease of the illuminated JV-curve towards forward voltages can thus not be explained with the increase of the dark current alone. In fact, the negligible amplitude of the dark current at the maximum power voltage indicates that the actual performance of the solar cell is governed by a mechanism entirely different of the dark current mechanism. On the other hand, this is contrasted by the fact that the open-circuit voltage of solar cells was found to scale directly with the amplitude of the dark current [SAK89].
Also, JV-curves of different light intensities, including the dark curve, were found to intersect in a single, well defined point [KUS89]. This point was then used for some detailed interpretation

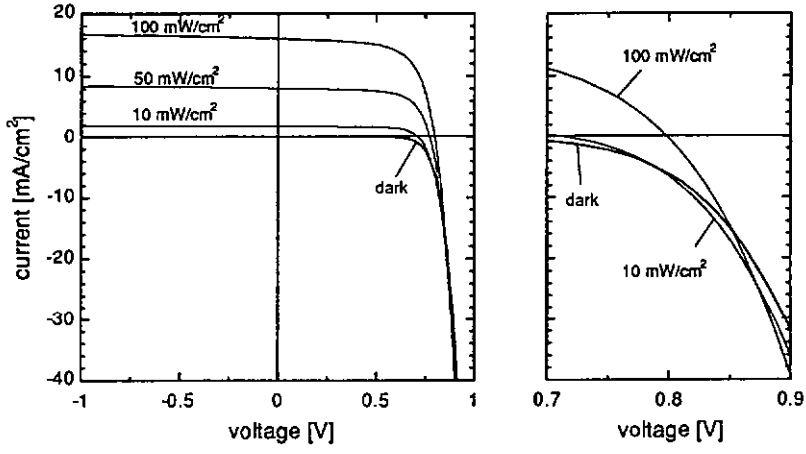

Figure 2.10: JV-curves of a typical amorphous silicon p-i-n solar cell (silicon carbide p-layer, i-layer thickness 0.5 µm, textured TCO, same as in Figure 3.3) for the AM1.5 solar spectrum at different intensities, and in the dark. Right: the same data, but intersection voltage range only.

[KOP92]. But for the solar cells analysed in the present work, no well defined intersection point was found, but the intersection was smeared out over a certain voltage range (Figure 2.10, right). In the present work, given the difficulty of interpretation, the analysis of the dark JV-curves was not further pursued.

2.2.2 Spectral response

Photons incident on a photovoltaic device have a certain probability to be absorbed and to create one electron-hole pair, which is then contributing with another probability to the external solar cell current. The product of these two probabilities, as a function of the energy of the photon, or the corresponding wavelength λ, is the spectral response. It is determined as the proportion of change in the external solar cell current $j_{ext}(\lambda)$ to the incident monochromatic photon flow $\Phi(\lambda)$

$$SR(\lambda) = \frac{\Delta j_{ext}(\lambda)/q}{\Phi(\lambda)} \quad \text{with} \quad \Phi(\lambda) = \frac{I(\lambda)}{hc/\lambda} \tag{2.49}$$

Link to the solar cell current under linear conditions

The spectral response is particularly useful if it can be associated with a range of linear correspondence between illumination and solar cell current. In this case, the spectral response represents the direct transfer function between any arbitrary light spectrum (total intensity I_0, power density distribution $\pi(\lambda)$), and the total light-generated solar cell current J_{light}:

$$J_{light}(I_0) = q \cdot I_0 \cdot \int_0^\infty SR(\lambda) \cdot \frac{\pi(\lambda)}{hc/\lambda} \cdot d\lambda \tag{2.50}$$

with

$$I_0 = \int_0^\infty p(\lambda)\, d\lambda \tag{2.51a}$$

and

$$\pi(\lambda) = \frac{p(\lambda)}{I_0} \qquad \left(\int_0^\infty \pi(\lambda)\, d\lambda = 1\right) \tag{2.51b}$$

Differential spectral response, and the generalised link to the solar cell current

In solar cells, linear operation can not generally be assumed. To address the most general case, differential spectral response techniques must be employed. Figure 2.11 shows the set-up employed in the present work. A light-chopper is used to measure the differential current signal produced by a monochromatic AC probe-beam in presence of an continuous bias-light. Similar set-ups have been described elsewhere [KUS87].

The differential spectral response corresponds still to the basic definition of Eqn. 2.49, but it refers to the amplitude of the probe-light $\Phi(\lambda)$ being much smaller than the typical light intensities of the operating solar cell. The differential spectral response is measured in the solar cell that operates at a given bias-light, and at a given voltage. The small amplitude of the probe-light assures that the probe-light does not significantly disturb the bias condition. This conditioo is checked by verifying that $SR(\lambda)$ is independent of the amplitude of $\Phi(\lambda)$. It should be noted that in the dark (without bias-light) the differential spectral response is not defined because the above condition is violated.

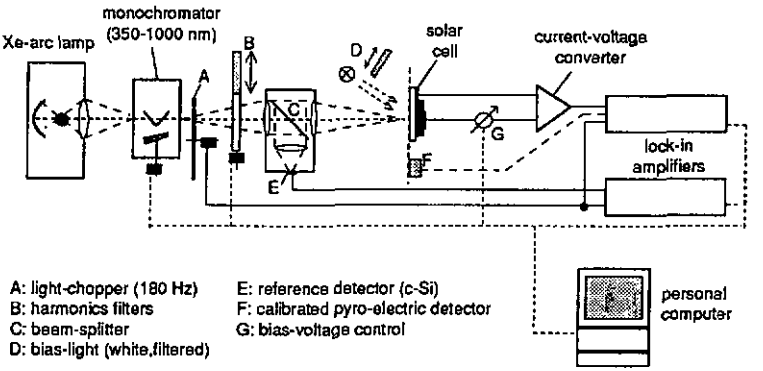

Figure 2.11: Schematic set-up for the measurement of the differential spectral response. Lock-in technique is used to measure the low-level differential solar cell currents.

With a well behaved, differentiable current-intensity relation (no hysteresis etc.), the differential spectral response is then the spectrally resolved derivative of the current-intensity relation at the given bias-light intensity I_x:

$$\frac{dJ_{light}}{dI}(I_x) = q \cdot \int_0^\infty SR(I_x,\lambda) \cdot \frac{\pi(\lambda)}{hc/\lambda} \cdot d\lambda \tag{2.52}$$

The total light-generated current is then the integrated differential spectral response, from zero to the full intensity I_0:

$$J_{light}(I_0) = q \cdot \int_0^{I_0} \left(\int_0^\infty SR(I,\lambda) \cdot \frac{\pi(\lambda)}{hc/\lambda} \cdot d\lambda \right) dI \tag{2.53}$$

The currents as described in Eqn.(2.51) and Eqn.(2.53) refer to the light-generated solar cell current alone, without taking into account a light-independent dark current. The total external solar cell current is thus

$$J_{ext}(I_0) = J_{light}(I_0) + J_{dark} \tag{2.54}$$

In amorphous silicon solar cells, the dark current can typically be neglected, except at high forward voltages.

Saturated spectral response : distinction between optical ond collection losses

For amorphous silicon p-i-n solar cells, a linear operation is obtained under saturation at reverse bias voltage, as defined in section 2.2.1. Analogous to the definition of the saturated current J_{sat}, also a saturated spectral response $SR_{sat}(\lambda)$ is defined as the spectral response measured at a voltage sufficiently high that the response becomes voltage independent for all wavelengths. Under this condition, the spectral response is also independent of the amplitude of both bias-light and probe-light, and the simpler spectral response versus current relation according to Eqn. 2.50 applies.

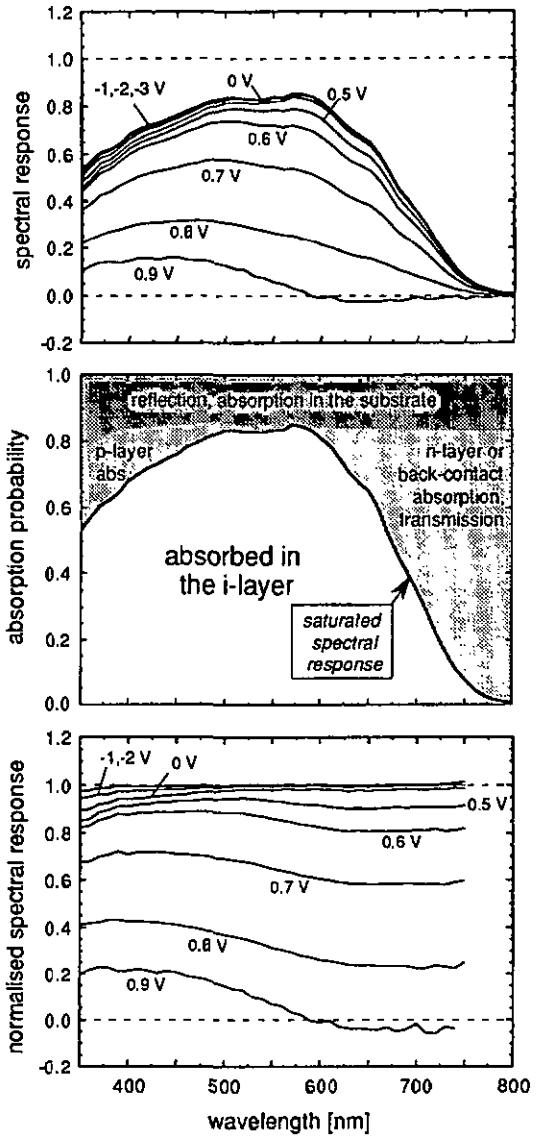

Figure 2.12: Top: measured voltage dependent differential spectrol response of a typical amorphous silicon p-i-n solar cell (silicon carbide p-layer, i-loyer thickness 0.5 μm, iextured TCO), with 100 mW/cm^2 white bias-light. The saturated spectral response allows to discriminate between optical losses (middle), and a differential i-layer collection probability (bottom).

The attractiveness of $SR_{sat}(\lambda)$ is that it enables to discriminate between the optical and the collection losses (see Figure 2.12). The optical losses, such as reflection, transmission, and parasitic absorption in the doped and other non-active layers, correspond to the difference between $SR_{sat}(\lambda)$

and unity. The i-layer collection losses, on the other hand, can be further characterised by the analysis of the voltage dependency of the spectral response. To this end, the voltage dependent spectral response is normalised with respect to $SR_{sat}(\lambda)$:

$$SR_{norm}(I,V,\lambda) = \frac{SR(I,V,\lambda)}{SR_{sat}(\lambda)} \tag{2.55}$$

The normalised spectral response SR_{norm} describes the probability of a photon, once absorbed in the i-layer, to yield an electron in the external solar cell current. Again, it is a differential probability, characteristic of a particular voltage and bias-light. The wavelength dependency of this collection probability can theo be used to locate the collection losses within the i-layer. This was extensively done in the past [e.g. MIT85, KUS87, KOP92].
However, without further treatment, the information can only be of qualitative nature, because the positional information is only indirect, via the change in the absorption profile depth of the different wavelengths. Therefore, it is only possible to distinguish between collection close to the illuminated interface (short wavelength light), and the average collection from the whole i-layer (long wavelength light). In section 2.2.3 it will be shown how a quantitative position dependent collection probability can be extracted from the wavelength dependent collection efficiency.

Generalised collection analysis based on the bias-light dependent spectral response

Whereas the analysis of the optical losses is straightforward, the interpretation of the voltage dependent i-layer collection losses requires a more careful analysis. As seen above, in a general, non-linear case, the spectral response data is only representative of the differential collection probability at the measurement bias-condition. At any given bias-condition, the differential collection probability thus represents the wavelength dependency for a small signal variation of the bias-light, but not necessarily the wavelength dependency of the overall collection of the bias-light itself. In Figure 2.13, the schematic relation between the total solar cell current, and the bias-light intensity is depicted. In this graph, the differential collection probability for a certain bias-light intensity determines the slope of the curve (Eqn. 2.52). Case 1 represents the general, non-linear

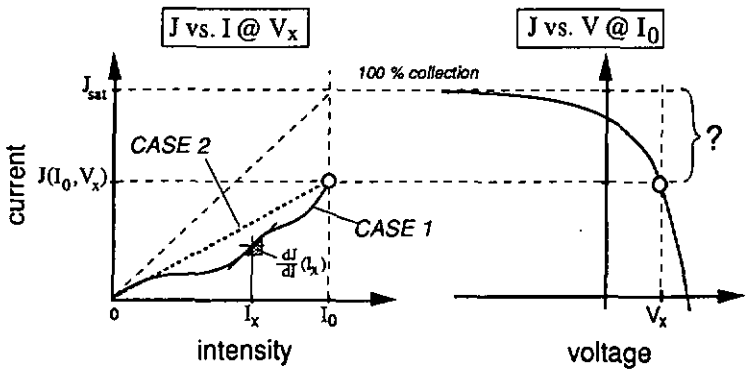

Figure 2.13: Schematic current-intensity dependency at a given voltage V_x, for a general, non-linear (case 1), and a linear (case 2) behaviour, and its relation to a singular point on the JV-curve.

case. Clearly, no single slope, but only the integration of the slope according to Eqn. 2.53 can explain the total current collection. In many cases however the slope at a certain bias condition might be a useful qualitative information describing the local trends.
In some cases, depending on the nature of the effect that governs the collection, the differential collection probability can be independent of the bias-light intensity. This is equivalent to the current-intensity relation being linear, and the slope in Figure 2.13 being constant (case 2). In this special case, one single differential spectral response measurement, taken at an arbitrary bias-light intensity, fully describes the collection of the total current (Eqn. 2.50 is applicable).

Figure 2.14 shows measured examples of both a strongly non-linear case (case 1), and of a very linear case (case 2). The non-linear case is a thick p-i-n cell, illuminated from the n-side, and the linear case is a thin, light-soaked p-i-n cell, illuminated from the p-side. The underlying mechanisms of these behaviours will be addressed in chapter 3. For both samples, at a given

Case 1:

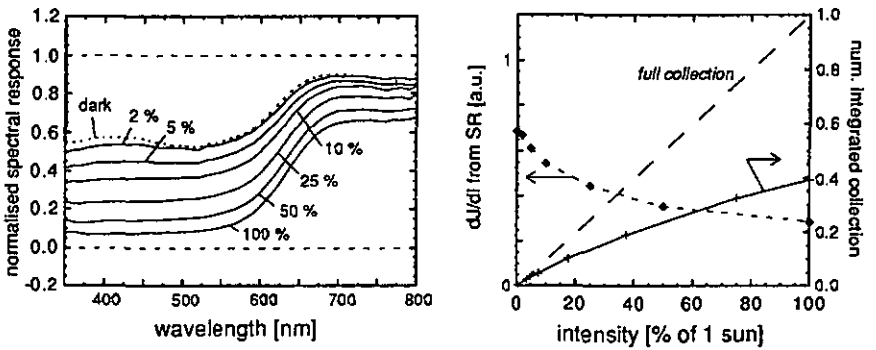

Case 2:

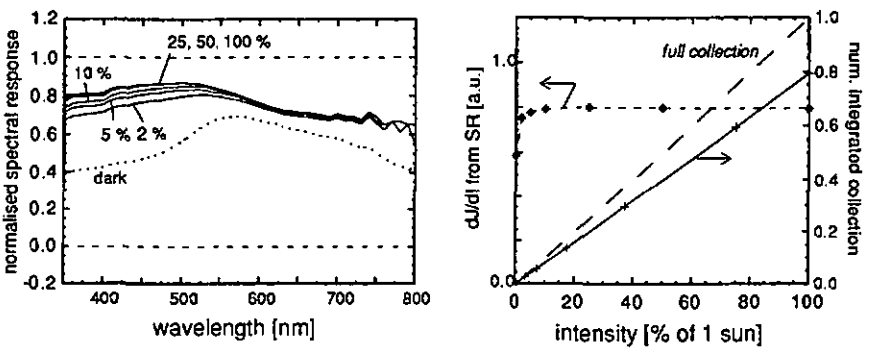

Figure 2.14: Current vs. intensity analysis for a strongly non-linear (case 1, top), and an approximately linear case (case 2, bottom). Left: normalised spectral response as a function of the bias-light intensity; Right: dJ/dl, as a function of intensity, from the bias-light dependent spectral response, and integrated total collection as a function of intensity.
Case 1: p-i-n solar cell, i-layer thickness 2 µm, illumination from the n-side, non-linearity due to the valence-band tail-states (see section 3.2.3), 0 V external voltage, total collection at the full light-intensity: 41 %.
Case 2: p-i-n solar cell, i-layer thickness 0.5 µm, illumination from the p-side, light-soaked for 400 hours, linear because operation governed by the dangling-bonds (see section 3.2.2/3.2.3), 0.4 V external voltage, total collection at the full light-intensity: 77 %.

voltage, the spectral dependent collection was measured with the bias-light varying between the dark and the full bias-light intensity. Clearly, in the non-linear case, the differential collection probability is a strong function of the bias-light intensity, and dJ/dI is varying correspondingly. Only by integration of dJ/dI over the full range of bias-light, according to Eqn. 2.52, the total current collection is thus accurately determined.

It should be noted that with the data of one single bias-light intensity alone, the total current collection of case 1 can not be determined (e.g. the data at 100 % intensity yields an erroneous total collection (24 %), whereas the integrated result (40 %) compares well with the total collection (41 %)). In the linear case (case 2), the differential collection probability is nearly constant as a function of the bias-light intensity, and both the integration, and the simple formula (Eqn. 2.50) yield the correct total collection value.

Remark: In the second, overall very linear case, a strong shift of the collection probability is observed if the bias-light is completely suppressed (dark). This illustrates the general danger of using dark spectral response for interpreting the collection in (illuminated) p-i-n solar cells. This is because without bias-light (in the dark), the differential spectral response condition of a negligible probe-beam is violated, and thus no correlation with the differential collection of the bias-light current, as described by Eqn. 2.52, can be presumed.

By performing the discussed spectral analysis of the solar cell current collection for different voltages, the complete JV-curve can be analysed and reconstructed. This analysis was done for the very non-linear case of the 2 µm thick solar cell illuminated with white light from the n-side (Figure 2.14, case 1). Between the actually measured JV-curve and the spectral response, integrated over the whole range of the bias-light intensity according to Eqn. 2.53, an excellent agreement is found. For comparison, the results of the spectral response analysis with only one bias-light intensity (Eqn. 2.51) are also given, showing large discrepancies. This is typical for the situation of a strongly non-linear collection.

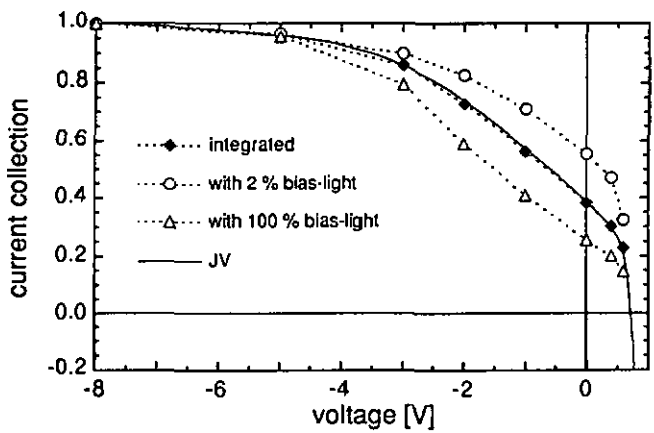

Figure 2.15: JV-curve at 100 % white light intensity (full line), compared with the voltage dependent spectral response analysis (symbols) of the same solar cell. The spectral response was measured at different bias-light intensities, ranging from 2 - 100 % of the white light intensity. The full symbols represent the integrated current according to Eqn. 2.53, the open symbols represent the results of an analysis with only a single bias-light intensity, evaluated by Eqn. 2.51. Solar cell: n-side illuminated, 2 µm thick i-layer (same cell as in Figure 2.14, top).

The excellent performance of the differential spectral-response analysis is thus demonstrated. Through this analysis, which universally links the spectral response and JV-curve, many results of the literature, reporting discrepancies between JV and spectral response [MIT85], can now easily be understood and explained.

Because the complete analysis over the whole range of bias-light intensity requires a substantial measurement effort, the simple analysis at one given bias-light intensity is in many cases still justified. Considering the special complication of the spectral response without bias-light (see e.g. chapter 3.3), the spectral response should then always be taken at sufficient bias-light intensity. As a rule of thumb, a bias-light with an intensity of 50 % of the full JV-light should give a reasonable trend of the collection determining the JV-curve. However, it must be kept in mind that in the general, non-linear case, one single spectral response alone can not explain the quantitative collection.

Spectral response higher than 100 %

While measuring the spectral response with bias-light illumination, under certain conditions normalised spectral response values higher than unity are found (Figure 2.16). This might at first glance appear unphysical. But as shown in various studies [MAR84, RUB94], the phenomenon can be understood as the effect of the detailed influence of the probe-light on the collection of the bias-light, such that for particular bias conditions (bias-light, and bias-voltage) more than one electron-hole pair is collected from the i-layer per absorbed photon of the probe-light. Typically, the coupling between the probe-light and the bias-light is through the i-layer electric field, with the coupling being such that the change of the electric field in the i-layer caused by the probe-light carriers is overall favourable to the collection of the bias-light carriers (see section 3.2.2). Obviously, the effect is not observed in the dark spectral response, because in the dark no bias-light carriers are available to be triggered by the spectral response probe-light. Also, the effect must vanish while approaching saturation, because in this case fewer and fewer carriers are available to be influenced by the probe-light (see Figure 2.16).

The fact that these effects can be observed has led to the conclusion that spectral response with bias-light might not be properly correlated with the collection of the bias-light, and thus with the

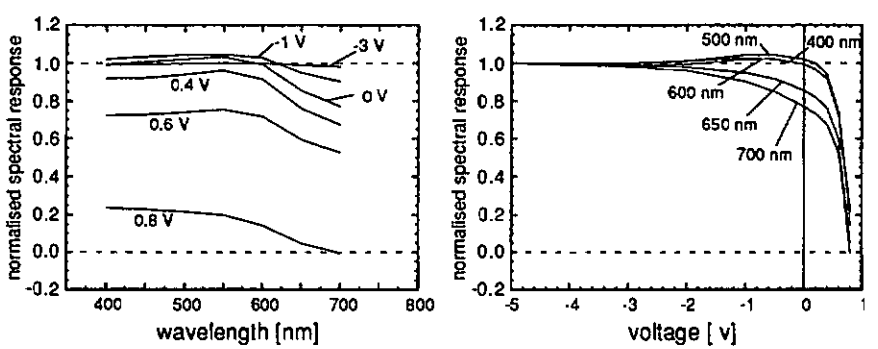

Figure 2.16: Normalised p-side spectral response of a solar cell with differential collection probabilities higher than unity. The bias-light is red-light (λ > 610 nm). The solar cell has an i-layer thickness of 1.5 µm, and is light-soaked.

solar cell performance in general [BEN93]. In opposition to this view it must be clearly stated that the phenomenon of SR > 1 is by no means in contradiction with the generalised collection analysis as described above. It has to be kept in mind that the spectral response under bias-light is only a differential collection at a specific bias-light intensity. According to Eqn. 2.52, the spectral response defines the derivative dJ/dI of current-intensity relation, as depicted in Figure 2.13. In principle, the derivative of the current-intensity relation can now take any positive (or negative) values, provided that the total current stays lower than the current of the full collection. Over a limited range of the intensity the slope can thus be higher than the slope of the full collection, and the current rises faster than the intensity. Under such conditions, the differential collection, as measured by the normalised spectral response, is higher than 100 %.
The occurrence of SR > 1 is not limited to cases of strongly non-linear operation. Also in a linear case, the normalised spectral response can for some wavelengths be larger than unity. The excess collection of these wavelengths is then compensated by the collection of other wavelengths staying below 100 %, such that the total dJ/dI remains below full collection. A typical case for such behaviour is the collection of p-side blue light in degraded solar cells illuminated with red bias-light (Figure 2.16, see also chapter 3).

2.2.3 DICE analysis

The spectral response measurement was shown to directly yield the differential i-layer collection probabilities as a function of the wavelength. For the development and engineering of the collection within the i-layer of a p-i-n device, one is actually interested in obtaining the position dependence of the collection within the i-layer. As discussed, the wavelength dependent plots alone allow only

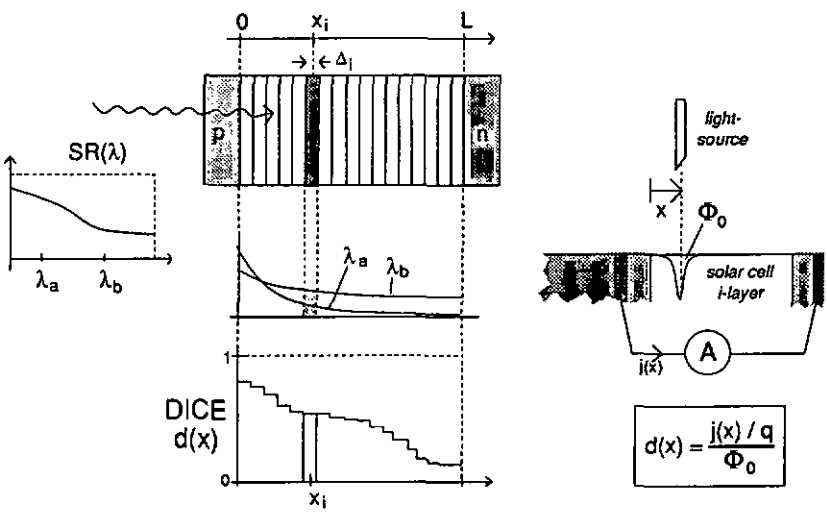

Figure 2.17: Division of the solar cell i-layer in slabs for the DICE analysis. In each slab, the collection probability has a well defined magnitude. An imaginary direct measurement of the DICE values is also indicated. Due to the actual physical dimensions of amorphous silicon solar cells, this measurement can not be realised.

for a very coarse positional discrimination.
The determination of an actual depth profile of the collection requires the numerical analysis of the spectral response data by the Dynamic Inner Collection Efficiency (DICE) method. The original method has been introduced by Takahama [TAK86], and it has since been applied in a number of different investigations [ONI91, LIN92, SAE92].
For the DICE analysis, the i-layer is imagined to be divided in slabs, with the number of slabs n determining the maximal positional resolution of the analysis. In each slab, the collection probability, i.e. the probability of a light-generated electron-hole pair contributing to the external solar cell current, is thought to have a certain value, which is the DICE value d. The DICE value d, as a function of the i-layer position x is thus the sought position dependent collection probability d(x). It is important to note that this collection probability is an existing, physically reasonable quantity. Given the technical possibility to illuminate the i-layer of a p-i-n solar cell laterally, the DICE value could be directly measured as the position dependent proportion between the locally generated carriers, and the resulting solar cell current.

The DICE equations

The measured wavelength dependent collection probability (the normalised spectral response $SR_{norm}(\lambda)$) is linked with the DICE values through a set of linear equations:

$$\begin{bmatrix} SR_{norm}(\lambda_1) \\ SR_{norm}(\lambda_2) \\ . \\ . \\ SR_{norm}(\lambda_n) \end{bmatrix} = \begin{bmatrix} \phi_{11} & \phi_{12} & . & \phi_{1m} \\ \phi_{21} & \phi_{22} & & . \\ . & & & . \\ \phi_{n1} & . & . & \phi_{nm} \end{bmatrix} \cdot \begin{bmatrix} d(x_1) \\ d(x_2) \\ . \\ d(x_m) \end{bmatrix} \qquad (2.56)$$

The coefficients ϕ_{ij} of the linear equations are the pure optical probabilities of a photon with a given wavelength λ_i to be absorbed in slab number j of the i-layer. These coefficients arise from the i-layer absorption coefficients, and other optical parameters. In the simplest case, considering a single light-pass through the i-layer, they are as follows

$$\phi_{ij} = \frac{\Phi_{ij}}{\sum_{j=1}^{n} \Phi_{ij}} \qquad (2.57)$$

with

$$\Phi_{ij} = \exp(\alpha(\lambda_i)\cdot(x_j - \Delta_j/2)) - \exp(\alpha(\lambda_i)\cdot(x_j + \Delta_j/2)) \qquad (2.58a)$$

Considering two passes through the i-layer, with a back contact reflection $R(\lambda)$, the optical model can be improved. In the present work, the following formula, employing $R(\lambda) = 1$, was used.

$$\begin{aligned} \Phi_{ij} = {} & \exp(\alpha(\lambda_i)\cdot(x_j - \Delta_j/2)) - \exp(\alpha(\lambda_i)\cdot(x_j + \Delta_j/2)) \\ & + R(\lambda_i)\cdot\left[\exp(\alpha(\lambda_i)\cdot(2L - x_j - \Delta_j/2)) - \exp(\alpha(\lambda_i)\cdot(2L - x_j + \Delta_j/2))\right] \end{aligned} \qquad (2.58b)$$

It is fundamental that the relation between the DICE values and spectral response only takes the linear form of Eqn. 2.56 if a differential spectral response is considered (as defined in section 2.2.2). This is because the linear superposition of the contributions from the different slabs

is only given under differential spectral response conditions. If the bias-conditions in the i-layer would be influenced by the spectral response measurement itself (as in the dark spectral response), Eqn. 2.56 can not assumed to be valid, and the DICE profile cannot be calculated.

Link to the solar cell currents

Being based on a differential spectral response, the DICE values themselves are again differential collection probabilities, representative only of a well defined bias condition. Analogous to the spectral response (section 2.2.2), the general link to the solar cell currents are easily found. In the following, Φ_G is the total integrated carrier generation rate in the i-layer at the full bias-light, and L is the i-layer thickness.

$$\Phi_G = \int_0^L G(x)\,dx \tag{2.59}$$

$$\gamma(\lambda) = \frac{G(x)}{\Phi_G} \quad \left(\int_0^L \gamma(x)\,dx = 1\right) \tag{2.60}$$

Analogous to Eqns. 2.52 and 2.53:

$$\frac{dJ_{light}}{d\Phi}(\Phi_x) = q \cdot \int_0^L d(\Phi_x, x) \cdot \gamma(x) \cdot dx \tag{2.61}$$

$$J_{light}(\Phi_G) = q \cdot \int_0^{\Phi_G} \left(\int_0^L d(\Phi, x) \cdot \gamma(x) \cdot dx \right) d\Phi \tag{2.62}$$

Solution and errors of the DICE analysis

With the spectral dependent collection SR_{norm} measured at n different wavelength points, Eqn. 2.56 defines a system of m linear equations for the m unknown DICE values d. With n > m, the determination of the DICE values appears to represent an ordinary optimisation problem to be solved by a least-square approach. But in the practical application of the DICE method, it turns out that the DICE equations are extremely ill-conditioned. Considering the typical precision of the inputs, the system is actually underdetermined, independent of the number of spectral response measurements m being larger than the number of unknown DICE values n [PRE86]. This means that there is a wide distribution of solutions that differ only very slightly in their optimisation error, and the DICE solution with the smallest error has very large and physically meaningless values.
Due to this difficulty, the DICE values are typically determined by the singular value decomposition (SVD) method [PRE86] rather than by a least-square optimisation: With the SVD method, the solution space of the DICE profiles can be tightly controlled and adjusted by the rank parameter in order to correspond to the measurement resolution.
The mechanisms governing the solution of the DICE equations become apparent through suitable simulations. Different from an actual physical measurement, in the simulation an arbitrary DICE profile is fixed, and is thus known. From this DICE profile, the corresponding spectral response can be directly calculated with Eqn. 2.56. Next, the resulting spectral response is perturbed with a

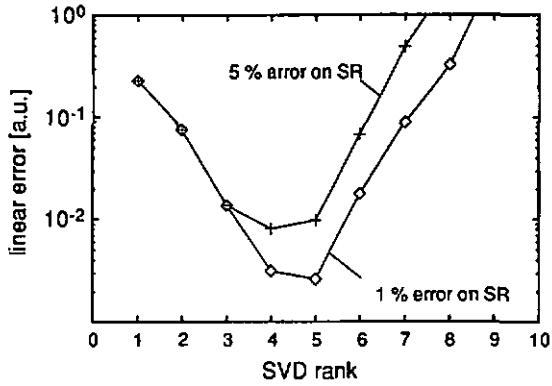

Figure 2.18: Linear error in reproducing a flat DICE profile (d(x)=const.) as a function of the rank of the SVD, if the spectral response is perturbed by a random error of 5% or 1% (see text for details on the testing procedure).

random error to simulate the unavoidable resolution limits of the spectral response measurement. The perturbed spectral response then serves as input to simulate the solution of the DICE equations. The comparison of the obtained DICE profiles with the original profile yields an error that quantifies the performance of the DICE analysis.

Figure 2.18 shows the error in reproducing an ideally flat DICE profile (d(x) = const.) as a function of the rank of the SVD. First, starting at very low ranks, the solutions gradually become better with increasing rank (the error is reduced as the solution space is enlarged). But beyond a certain optimal rank, the solution becomes worse again, as the collection grows towards very high and fast oscillating, unphysical values. The turning point depends on the simulated spectral response resolution: with increasing measurement resolution, the optimal rank is increased, and also the quality of the solution is improved. From Figure 2.18 it is apparent that with realistic measurement resolutions it is impossible to reach optimal ranks beyond 5 or 6. The capability of the DICE analysis to reveal the features of the collection probability distribution will thus always have certain well defined limitations.

Figure 2.19 shows the solution space for rank 4 and 5. The solution space is the set of position

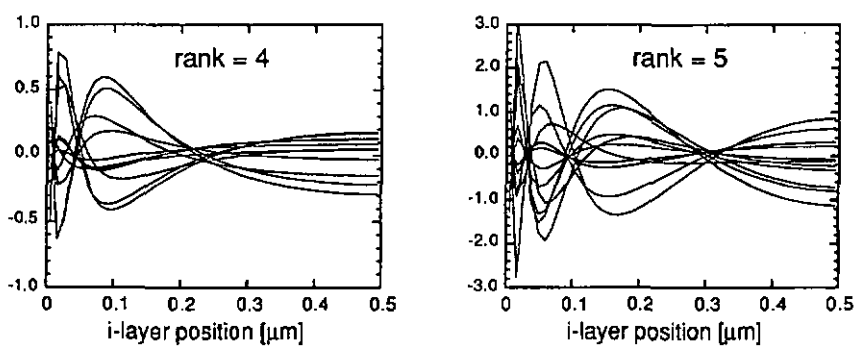

Figure 2.19: Solution space of the DICE solutions for rank 4 and 5 of the SVD (the DICE collection profiles, analysed with these ranks, are linear combinations of the depicted functions).

dependent functions, out of which the DICE solution will be composed by linear combination. Clearly, the functions of the solution space become increasingly resembling and finally turn flat with increasing distance to the interface from which the spectral response was measured.
This can now explain the fact that in all DICE applications found in the literature, the DICE profiles show a lot of detail near the p-i interface, but become always flat towards the n-i interface [TAK86, ONI91, LIN92, SAE92].

Bifacial DICE analysis

Whereas a strong asymmetry in resolution capability seems to be intrinsic to the standard DICE approach, there is a possibility to significantly improve the resolution in the back and middle of the i-layer. This is achieved by employing the combined spectral response measured from the p-side and spectral response measured from the n-side to generate the i-layer DICE profile.
This bifacial DICE analysis requires p-i-n devices with transparent back-contacts. This is not the case in a solar cell for optimised performance, but any p-i-n solar cell can usually be contacted with a transparent conductive oxide (TCO), or a semitransparent metal contact instead of its normal, opaque contact. The actual i-layer collection distribution, which is to be analysed, will typically not be affected by this different contact.

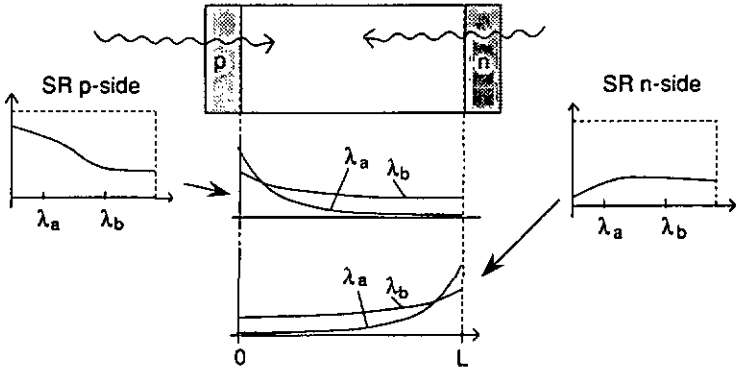

Figure 2.20: Schematic bifacial p-i-n cell , and schematic absorption profiles of the bifacial spectral response probe-lights, for the bifacial DICE analysis.

The p-side and n-side normalised spectral responses SR_p and SR_n are linked to the DICE values d through the bifacial DICE equations:

$$\begin{bmatrix} SR_p(\lambda_1) \\ SR_p(\lambda_2) \\ \vdots \\ SR_p(\lambda_n) \\ \hline SR_n(\lambda_1) \\ SR_n(\lambda_2) \\ \vdots \\ SR_n(\lambda_n) \end{bmatrix} = \begin{bmatrix} \phi_{11} & \phi_{12} & \cdots & \phi_{1m} \\ \phi_{21} & \phi_{22} & & \vdots \\ \vdots & & & \vdots \\ \phi_{n1} & \cdots & \cdots & \phi_{nm} \\ \hline \phi_{1m}' & \cdots & \phi_{12}' & \phi_{11}' \\ \vdots & & \phi_{22}' & \phi_{21}' \\ \vdots & & & \vdots \\ \phi_{nm}' & \cdots & \cdots & \phi_{n1}' \end{bmatrix} \cdot \begin{bmatrix} d(x_1) \\ d(x_2) \\ \vdots \\ d(x_m) \end{bmatrix} \qquad (2.63)$$

In the simplest case, the p-side and n-side coefficients ϕ_{ij} and ϕ_{ij} ' are equal and correspond to the coefficients of the single sided analysis (Eqn. 2.57):

$$\phi_{ij} = \phi_{ij}\text{ '} = \phi_{ij}\text{ (single side, Eqn. 2.57)} \tag{2.64}$$

In a more refined approach, differences in reflection behaviour between the p-side and the n-side illumination, as well as other differences in the respective optical paths would have to be considered (see below). In the present work, $\phi_{ij} = \phi_{ij}$ ' was assumed.

Resolution of the bifacial DICE onolysis

Simulations show that with the bifacial DICE analysis, for a given spectral response perturbation, the optimal ranks are higher than in the single sided analysis. In Figure 2.21, the error in reproducing an ideally flat DICE profile is plotted as a function of the SVD rank. For the bifacial analysis, optimal ranks of 7 to 8 are found for a spectral response perturbation of 1 %.

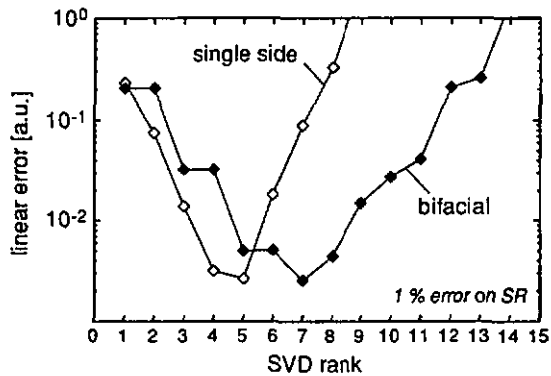

Figure 2.21: Linear error in reproducing a flat DICE profile (d(x)=const.) as a function of the rank of the SVD, for single sided, and bifacial analysis. The spectral response perturbation is 1 %.

By comparing the rank versus error behaviour of the two DICE methods, an empirical relation between the respective ranks is found as follows

$$\text{rank}_{\text{optimal}}^{\text{bifacial}} = 2 \cdot (\text{rank}_{\text{optimal}}^{\text{single sided}} - 1) \tag{2.65}$$

This relation was found to be valid independent of the amplitude of the spectral response perturbation. It was however not investigated to what extent it might depend on the shape of the employed DICE test functions.

The increased ranks and the symmetry of the bifacial DICE equations with respect to the middle of the i-layer (Eqn. 2.63) produce a distinct change of the solution space of the sought collection profile. Figure 2.22 illustrates the solution space for the ranks 7 and 8. Different from the single side situation (Figure 2.19), the distribution of the solution space functions is symmetric with

respect to the centre of the i-layer. Fast changing functions towards the interfaces hint at a high resolution capability in these regions, and at a lower resolution towards the centre of the i-layer.

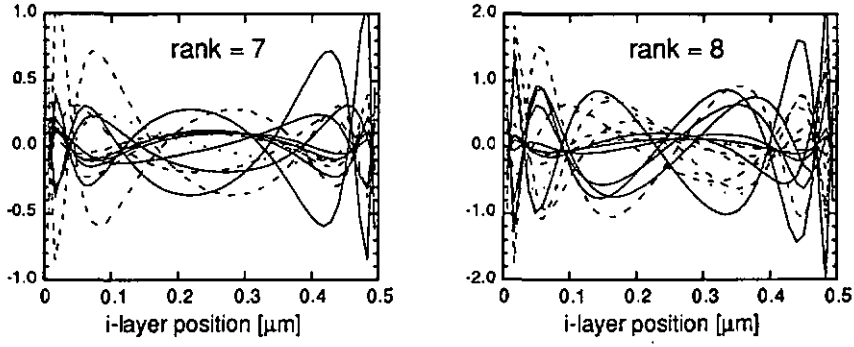

Figure 2.22: Solution space for the bifacial DICE analysis with rank 7 and 8 of the SVD (the DICE collection profiles, analysed with these ranks, are linear combinations of the depicted functions).

The difference in position dependent resolution capability between the two DICE approaches is illustrated in Figure 2.23. The Figure shows the error in resolving a ramp shaped collection profile, as a function of the ramp position within the i-layer. As a result, the error of the single sided analysis grows very large with increasing distance of the ramp position to the measurement interface. Differently, the resolution capability of the bifacial analysis is symmetric with respect to the i-layer, with the minimal resolution (maximal error) in the middle of the i-layer. If the two methods are compared, clearly the bifacial analysis is advantageous, as its resolution power is on the average much improved. Also, its resolution is more evenly distributed over the i-layer.

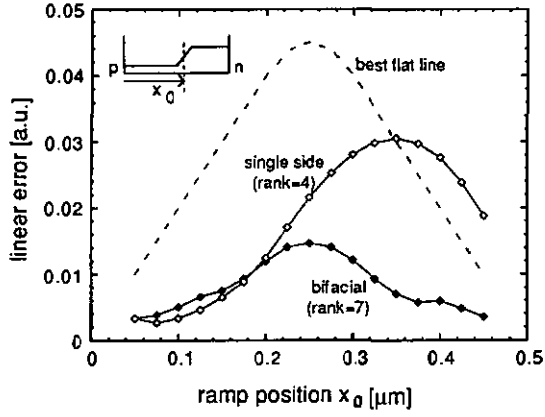

Figure 2.23: Error of the single sided and the bifacial DICE analysis in reproducing a ramp shaped DICE profile as a function of the ramp position within the i-layer. As a reference, the error of the best flat (d(x)=const) collection profile is also given (worst case, no position resolution).

Practical application of the DICE analysis

In chapter 3 and 4, the bifacial DICE analysis as described above is applied extensively for practical solar cell characterisation. In these applications, the uncertainties of the optical solar cell parameters (absorption coefficient, contact reflection) were generally very large. To avoid unphysical results due to these errors, the rank of the SVD had to be reduced to relative low values of 4 or 5, that yield a correspondingly reduced measurement resolution.
To be able to exploit the advantage of higher ranks, and thus higher resolutions, the optics of the solar cells to be analysed would have to be known more precisely. Most important, the solar cells to be investigated would have to be deposited on flat substrates. With textured substrates, the optical path is extremely complex, and a precise quantitative description very difficult. Also, the actual contact reflections for both the p-i and the n-i interface would have to be determined in a suitable way. By such improvements, ranks of 7 or 8, and the corresponding increase in resolution seems possible.

2.2.4 Electric field measurements by µs charge collection

It was shown above that spectral response data can be used to obtain the carrier collection probability as a function of the i-layer position. In practical work it becomes important to gain some insight into the underlying reasons for this collection probability. The performance of amorphous silicon solar cells is the result of the direct competition between carrier separation and carrier recombination within the intrinsic layer. A measured collection probability gives the result of these competing processes, but it does not offer a direct explanation of how these come about.
The major driving force of the carrier separation in amorphous silicon p-i-n cells is the electric field within the i-layer (see chapter 2.1). Due to charged gap states, the electric field in the i-layer is often not constant, but shows an amplitude that varies strongly as a function of the i-layer position. To understand the detailed collection in the p-i-n solar cells, a direct measurement of the electric field distribution within the i-layer would thus be very valuable.
Different methods have been proposed to measure the electric field distribution [STR83, VAN89, DIE91]. All these methods employ the fundamental link between the amplitude of the displacement current (j_{disp}) of charges moving in the i-layer (ΔQ), and the local electric field (E_{local})

$$j_{disp} \sim \mu_Q \cdot E_{local} \cdot \Delta Q \qquad (2.66)$$

The p-i-n cell to be measured is illuminated by a short pulse of strongly absorbed light. This creates a number of electron-hole pairs near the illuminated interface. Depending on the measurement side, either the electrons (p-side illumination) or the holes (n-side illumination) will move through the i-layer under the influence of the electrical field, giving rise to externally measurable, transient displacement currents. Typically, the observed current transients have durations up to about 1 µs.
Two effects are critical in the interpretation of these current transients. Firstly, the moving carriers are subject to capture and release in shallow tail-states (multiple trapping), leading to a rapid dispersion of the travelling charges. Due to this dispersion, the externally measured current results from a distribution of charges that simultaneously move under different local electric fields. This

fundamentally complicates the interpretation of the measured currents. And secondly, travelling carriers may get permanently (with respect to the measurement time) lost by capture in deep states. Again, the treatment of these losses leads to an increasing complexity of the analysis.
In the original method of Street [STR83], neither dispersion nor capture losses are considered. The analysis is simple, but subject to large errors. In the Vanderhaghen's analysis [VAN89], the problem of dispersion is intrinsically treated, without a fundamental increase of the experimental difficulty. The drawback of the method is that it can not address a general electric field distribution (see below). Also, permanent capture losses are not addressed. With the differential delayed field method [DIE91], capture losses can be considered, but not the effects of the dispersion. Also, the intrinsic experimental difficulties of that method are considerable, and place basic limitations on the resolution.

Vanderhaghen's method

In the present work, the Vanderhaghen's method [VAN89] was employed to characterise p-i-n solar cells (Figures 3.10 and 4.4). In this method, a constant electric field is superimposed over the to be measured electric field by applying a voltage step shortly prior to the light pulse. By the superposition of the constant electric field, the net i-layer electric field is exactly cancelled wherever the original electric field (prior to the voltage step) is equal in magnitude to the superimposed field. After the light-pulse, the light-generated carriers drift towards the location where the field is zeroed, giving rise to a measurable external displacement current.
The elegance of the scheme is that the integration of this displacement current yields directly the i-layer position of the zeroed electric field (Figure 2.24). To this end, the integrated current is normalised with respect to the integrated current at high reverse voltage, where the carriers can be assumed to pass through the whole i-layer (Q_0). The normalised integrated charge is then equal to the relative position of the zeroed field with respect to the total i-layer thickness. Due to the

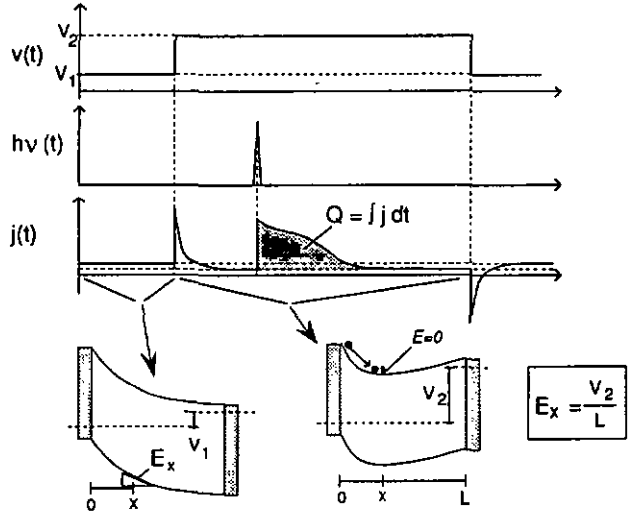

Figure 2.24: Schematic timing of the transient solar cell current during the electric field measurement according to Vanderhaghen [VAN89]. The measurement set-up used for the present work is described elsewhere [WYR92].

integration over time, the dispersion of the carriers in arrival time at the zeroed field location will not influence the result.

One integrated current transient thus determines the position of one given electric field strength. By varying the amplitude of the superimposed electric field, the position of other field strengths can be determined successively. The plot of electric field amplitude versus i-layer position can be interpreted as an electric field profile of the i-layer (Figure 2.25).

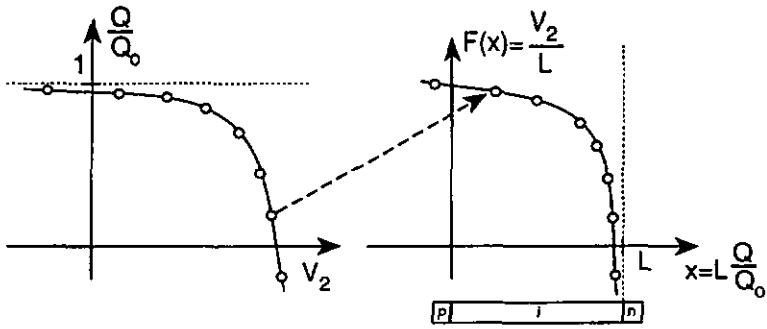

Figure 2.25: Correspondence between the normalised collected charge (see Figure 2.24), and the electric field profile within the solar cell i-layer.

Guidelines for the practicol interpretation of the field profiles

For the interpretation of the electric field profiles it is crucial to keep in mind that only the occurrence of electric fields with continuously decreasing amplitudes are correctly reproduced by Vanderhaghen's analysis scheme. If with increasing i-layer depth the electric field increases, the corresponding amplitudes are not detected, and only if the electric field falls below the lowest amplitude yet detected, again a correct value can be extracted. Obviously, from the measured collection curve itself, it cannot be determined whether zones with an increased field strength are being hidden in the plot.

Figure 2.26 shows different schematic electric field profiles, and how they are resolved by measurements from the p-side or the n-side. Clearly, the bifacial measurement can extend the domains of correct electric field representation (cases 1 and 2). It is a useful concept to imagine the measured field profiles always as a lower limitation to the actual electric field. In the case of bifacial measurements, the higher of both profiles represents this lower limit. There might however always be high field features within the i-layer that have no indication whatsoever in the measured profiles (case 2 and 3). An indication as to whether the measurement gives reasonable results is that the measured field profiles have comparable values with the known average electric field (V_{bi}/L). If the measured electric fields are substantially below the average electric field over large parts of the i-layer, this is an indication that zones with high electric fields are not being detected. As mentioned, carrier losses due to capture can also represent a source of error. These losses reduce the integrated displacement current, and lead therefore to a systematic underestimation of the i-layer depth. The corresponding error is increasing with growing i-layer depth.

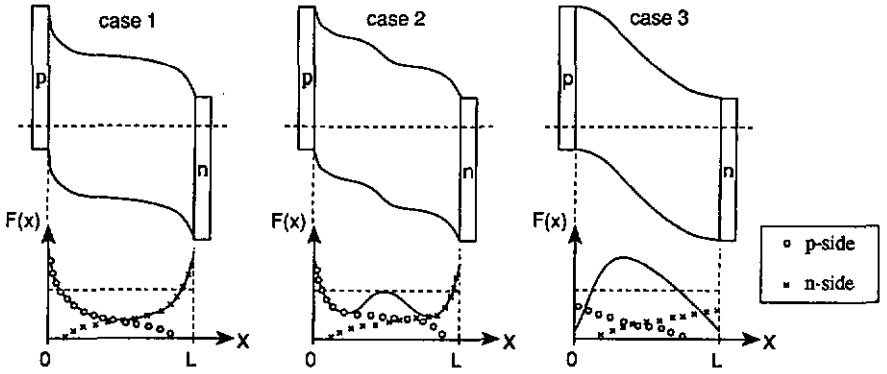

Figure 2.26: Different schematic band-diagrams (top) and the corresponding electric field distribution (bottom), including the electric field profiles that are expected to be retrieved by the method of Vanderhaghen [VAN89] for p-side (electron transit, round symbols) and n-side analysis (hole transit, cross symbols). The horizontal dashed lines indicate the average i-layer electric field.

Difficulties may also arise while measuring the electric field in illuminated p-i-n cells. This is because for a valid measurement the displacement current integration time must stay smaller than the dielectric relaxation time of the superimposed, pulsed electric field (see above). This is typically the case in the dark [WYR92]. With increasing illumination intensity, the dielectric relaxation time of amorphous silicon is however quickly decreasing, leading to an upper limitation of acceptable bias-light intensities for the electric field measurement in p-i-n cells.

Despite its obvious drawbacks, the described measurements of current transients can be a useful tool for p-i-n characterisation, offering a direct access to one of the main parameters of amorphous silicon solar cell operation, the electric field. As seen above, the method is not foolproof, and the necessary care must be taken when interpreting its results.

2.3 Fabrication technology of a-Si:H solar cells

This section addresses the fabrication of the solar cells devised and analysed throughout this work. With the actual technology of amorphous silicon solar cell deposition not being the primary issue of this work, the section does not attempt to be comprehensive. Rather it is limited to the few topics that have been found decisive for the development of 'state-of-the-art' single junction solar cells in the given technology environment (see below). Also, the technological basis for the low-level i-layer doping of chapter 4 is introduced.

All amorphous silicon films and solar cells described in this work have been deposited by plasma enhanced glow discharge employing a plasma excitation frequency of 70 MHz. The use of plasma excitation frequencies in this range has been referred to as to the "VHF-glow-discharge method". The use of VHF frequencies instead of the most commonly used, lower frequencies (13.56 MHz, DC) was found to significantly influence the growth and the material properties of amorphous silicon. In particular the use of VHF frequencies was found to increase the deposition rates, to allow for the growth of very thick films with reduced internal stress, as well as to promote the growth of microcrystalline films. These different issues have been the object of a large number of publications, of which [SHA92] gives a good overview.

As mentioned, the influence of the plasma excitation frequency was not systematically studied in the present work. Rather 70 MHz deposition was employed to develop standard type amorphous silicon p-i-n solar cells. In no case solar cell behaviours strikingly different from those of cells fabricated with standard methods were found. Future studies will thus have to address the question whether the "VHF method" could result in solar cells with improved performance over conventionally produced solar cells (e.g. through the use of microcrystalline layers, improved intrinsic materials, etc.). Equally, it is clearly beyond the scope of this work to show to what extent VHF deposition will enhance the industrial fabrication of a-Si:H solar cells by its superior deposition rates and/or reduced powder formation.

2.3.1 Reactor design and intrinsic a-Si:H layer deposition

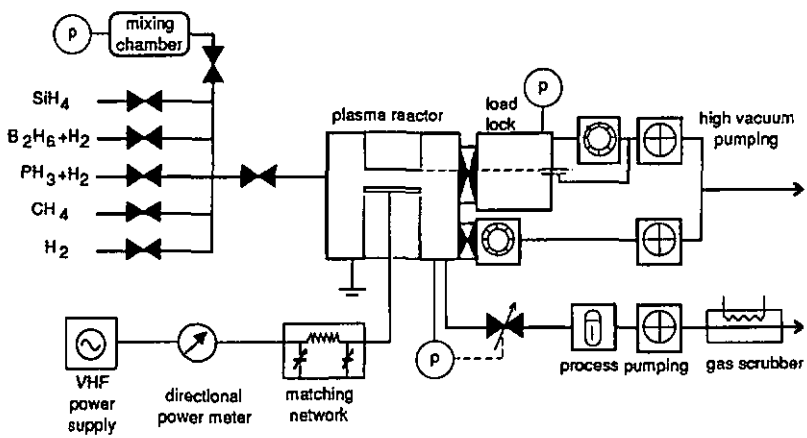

Figure 2.28: Schematic gas supply, pumping systems, and RF-power supply of the VHF plasma deposition set-up

Figures 2.28 and 2.29 give the details on the plasma deposition system employed. The system is a single chamber system. Whereas often multiple chamber systems are employed for solar cell fabrication, the present work can be considered as a demonstration how also in single chamber systems high performance solar cells can be fabricated (similar experiences were made elsewhere [BEN93]).

The system is equipped with a separated loading chamber (load-lock). This allows a much higher sample throughput through a reduction in pumping times. In fact, the actual vacuum standard (base pressure) in the deposition chamber is systematically improved as many deposition cycles are executed without opening the deposition chamber to the atmosphere. Also, the load-lock enables an added versatility in the layer deposition sequence through the possibility to apply chamber treatment steps while the sample is stored in the load-lock (see section 2.3.3).

Special care was taken in designing the elements defining the actual deposition zone. Basically the system is of the capacitive type with a grounded electrode (Fig. 2.29, B) and a powered electrode (Fig. 2.29, C), but the deposition zone is separated form the relatively spacious bulk of the chamber by a mechanical enclosure (Fig. 2.29, H). This enclosure serves several purposes:

- It confines the flow of the deposition feed gas. As the gas is directly injected into the inner enclosure, the pick-up of impurities or contaminants from the outer zones (lower temperatures) of the chamber is reduced. By an evenly distributed injection (shower-head) on the whole the electrode circumference, the homogeneity of deposition is improved.
- The enclosure confines the plasma zone to an environment of elevated temperature. Although the confinement is not actively heated, it reaches temperatures close to those of the electrodes through passive heating. By the higher temperature, the formation of powder and the contamination (out-

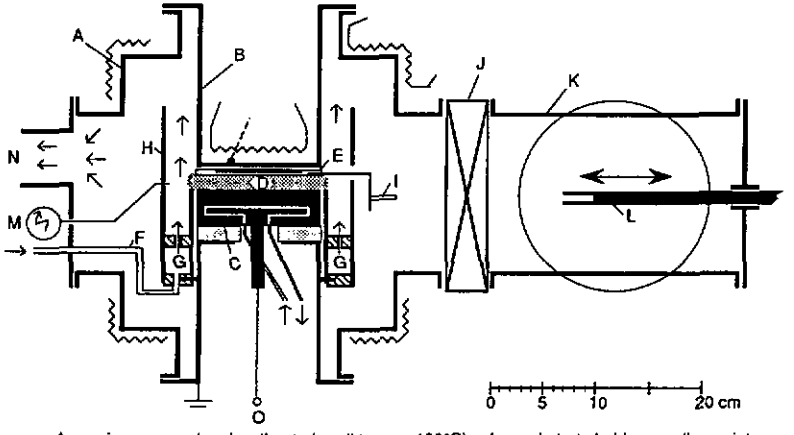

A: main vacuum chamber (heated, wall temp. ~100°C)
B: grounded electrode (heated, max. temp. 350°C)
C: powered electrode (heated by hot air , ~150°C)
D: plasma zone (electrodes spacing 1.6 cm)
E: substrate/substrate holder
F: process gas conduit
G: circular gas distribution channel/shower head
H: plasma zone enclosure (passively heated)
I: substrate holder coupling point
J: gate valve
K: load-lock chamber (separately pumped)
L: substrate holder manipulator
M: plasma ignition
N: process pump port
O: HF feeder point

Figure 2.29: Geometrical internal configuration of the VHF glow discharge deposition system for a-Si:H solar cell fabrication

gassing) is reduced.

- Further, the confinement limits the deposition of both film and powder onto mechanical parts that can be removed from the system for cleaning, a feature which greatly facilitates the system maintenance.

The above concept bears still a large improvement potential. In a future system, it would be desirable to (a) strongly reduce the ratio of plasma zone over total chamber volume, (b) to assure an active heating of the plasma zone enclosures to provide an isothermal deposition environment, (c) to apply the gas injection directly through the electrode to further homogenise deposition, (d) to increase the deposition area in order to reduce boundary effects and to allow for results more relevant to actual industrial solar cell fabrication.

Intrinsic layer deposition:

The original publications on the 'VHF-method' describe the deposition of intrinsic a-Si:H films at deposition rates as high as 25 Å/s [SHA88]. Those films have been produced under conditions of strong silane depletion, and the deposition rate was limited by the silane flow to the reactor [SHA88]. Also, the deposition conditions were characterised by a very strong powder formation. The films produced at those conditions were shown to exhibit a material quality equivalent to those produced with standard procedures at lower deposition rates. This was confirmed by the fabrication p-i-n solar cells of 8 % efficiency employing those conditions for i-layer deposition [FIS91].
Nevertheless, for a controlled fabrication of solar cells, the deposition regime as described above is rather problematic. First, because the powder formation directly causes shunting problems in the solar cells. Then, because the accumulation of powder in the reactor leads to a drift of the reactor characteristics that prohibits multiple solar cell deposition sequences and requires a reactor cleaning after each deposition. Additionally, in a regime of strong silane depletion it is very difficult to achieve a homogeneous deposition rate over the whole electrode area.

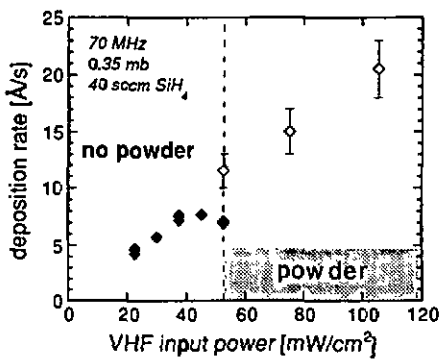

Figure 2.30: Deposition rate as a function of VHF input power density (as measured at the entrance of the matching network). The electrode area is 133 cm^2. The substrate temperature is approx. 220°C. For the i-layer of all solar cells described in this work, the power density was 25 mW/cm^2. Error bars indicate deposition-rate variation over the substrate area.

For these reasons, a regime of high silane flow (silane surplus), and a reduced RF input power was adopted for the solar cell i-layer deposition. In this regime, the deposition rate is limited by the RF input power, as shown in Figure 2.30. With increasing RF power density, at low powers an about linear correspondence between power and deposition rate is found, and no visible powder accumulation is observed in the reactor (as determined by inspection after deposition). Also, the films show a good uniformity. With raising power density, again powder formation is observed, together with an increasing thickness inhomogeneity of the deposited films. In the vicinity of the powder threshold, and at higher RF powers, the deposition is also subject to instabilities (slow oscillations due to powder build-up and release).
While stable, powder-less deposition was found up to about 8 Å/s (at 40 mW/cm^2 RF input power), in this regime and in the described reactor, the solar cells described in this work employed films deposited at 4 - 5 Å/s (~ 25 mW/cm^2). The films deposited under those conditions showed again so called standard device quality properties.

2.3.2 Amorphous silicon carbide (a-SiC:H) 'window layers'

To reduce the solar cell p-layer absorption losses, boron doped silicon carbon alloys were developed to be used as p-side 'window layers'. At a plasma excitation frequency of 70 MHz, films were deposited from silane/methane mixtures. Low concentrations of diborane were added for p-type doping. At methane concentrations of 60 - 75 % in the feed gas, a characteristic increase of the optical gap was indicating substantial carbon incorporation into the deposited film (Figure 2.31, left). In agreement with the literature [LEC90], the doping with diborane was found to in turn compete with the widening of the optical gap, i.e. the absorption is increasing with rising doping concentration (Figure 2.31, right). Figure 2.32 shows the 'curve of merit' formed by different a-SiC:H(B) films deposited at 70 MHz. The values of conductivity obtained as a function of the optical gap are in fact in the close range of what is typically found for standard deposition techniques (to be compared e.g. with [LEC90]).

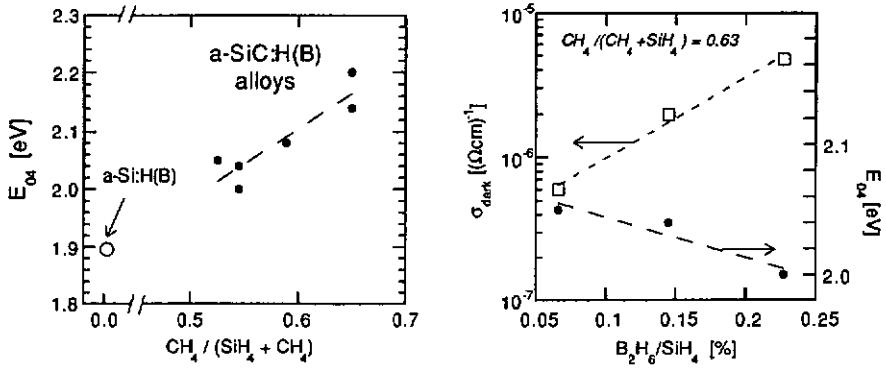

Figure 2.31: Boron doped a-SiC:H films, deposited by VHF (70 MHz) deposition, at a power density of 25 mW/cm^2 and at a pressure of 1 mb. Left: Energy of 10^4 cm^{-1} absorption (E_{04}) as a function of the methane to silane ratio. Right: dark conductivity and E_{04} as a function of diborane doping for a constant methane to silane ratio.

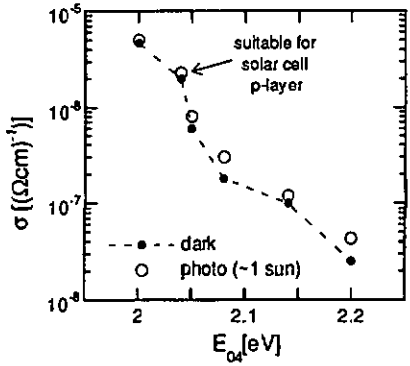

Figure 2.32: 'Curve of merit' for different boron doped a-SiC:H films deposited by VHF deposition at 70 MHz.

An a-SiC:H(B) film with a dark conductivity of $2 \cdot 10^{-6}(\Omega cm)^{-1}$ and E_{04} of 2.04 eV was applied as solar cell p-layer. The optimal thickness was determined by the onset of the V_{oc} break-down while varying the p-layer deposition time (Fig. 2.33, left). Employing this p-layer, the spectral response in the short wavelength range, and thus the total solar cell current was clearly enhanced over cells not employing carbon alloyed p-layers (Fig. 2.33, right).

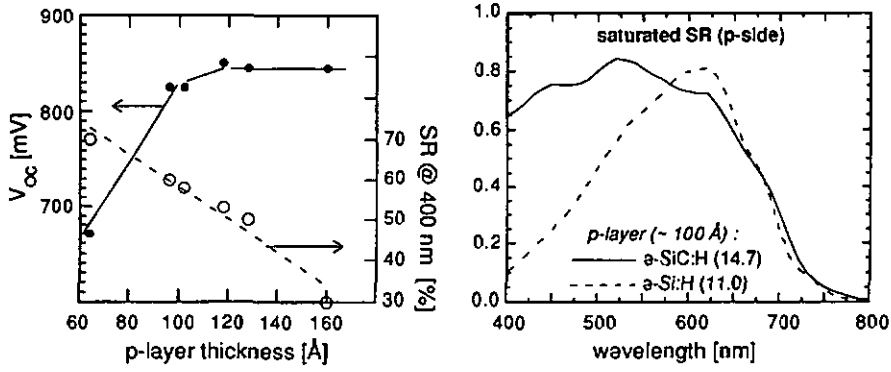

Figure 2.33: Application of a-SiC:H(B) films as p-window layer in p-i-n solar cells. Left: a-SiC:H p-layer thickness optimisation. Right: comparison of p-side spectral response of solar cells with and without a-SiC:H window layer. In brackets: saturated current in mA/cm².

2.3.3 Doped layer to i-layer cross-contamination

Because all layers of the solar cell are deposited in the same chamber, the control of the dopant cross-contamination of the i-layer is crucial in single chamber p-i-n solar cell fabrication. In the described reactor, for the deposition of p-i-n solar cells with SiC p-layers and microcrystalline n-layers, interestingly phosphorus contamination was found to be dominant. If solar cells were deposited in a continued p-i-n-p-i-n-.. sequence, the solar cells showed the characteristic decrease of the red-light collection of phosphorus i-layer doping (Figure 2.34, left; see also section 4.2.2). It should be noted that the decrease is only in the forward voltage range, whereas at 0 V the current is

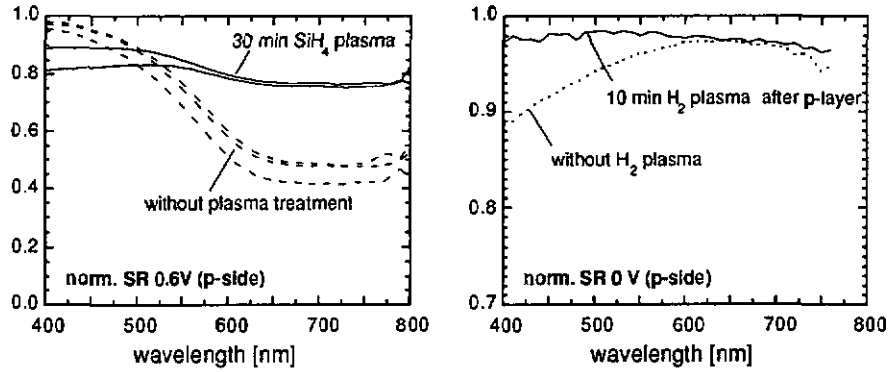

Figure 2.34: Left: Influence of i-layer phosphorus contamination on the normalised spectral response at forward voltage, and effect of a 30 min silane plasma prior to the solar cell deposition. Right: Boron contamination, and improvement by a hydrogen plasma step after the p-layer deposition, with the sample stored in the load-lock (normalised spectral response at 0 V).

still well saturated. Obviously, the i-layer phosphorus contamination must originate from the n-layer deposition of the previous solar cell. The problem was successfully addressed by the deposition of an i-layer on a dummy substrate (i^*) prior to each p-i-n solar cell deposition (i^*-p-i-n-i^*-p-i-n-....). As shown in Figure 2.34, left, the collection of red light was increased, resulting in an overall high collection at 0.6 V forward voltage.

Boron contamination of the i-layer is indicated by a decrease of the p-side blue light collection (see section 4.2.1). Only small boron contamination from the p-layer was found if silicon-carbide p-layers were employed (this is in contrast to non-alloyed p-layers, where typically a strong boron contamination was observed). Still, some indication of boron contamination is also seen in solar cells with SiC p-layers (Fig. 2.34, right). It was found that this contamination can be restrained by applying a hydrogen plasma step (H_2) after the p-layer deposition, while the substrate with the finished p-layer is pulled back to the load-lock chamber. For a continuos series of solar cell depositions in the single chamber system the following sequence was finally adopted: i^*-p-H_2-i-n-i^*-p-H_2-i-n-.... .

2.3.4 Low-level i-layer doping

Chapter 4 of this work deals with p-i-n solar cells that are low-level doped in the i-layer. The doping schemes employed are not constant in the whole i-layer, but they vary locally as a function of the i-layer position (grading). To achieve the required minute dopant concentrations in the 1 ppm range, the standard dopant gases, which are supplied at concentrations of about 1000 ppm in hydrogen, are first diluted to the 10 ppm range in a mixing chamber (Figure 2.28). During the i-layer deposition, gas from the mixing chamber is then added to the silane flow to produce the desired low doping concentrations.

Graded doping profiles could not be achieved by directly regulating the flow from the mixing chamber, because the exchange rate of the feed gas in the deposition chamber was too slow. The different gradings were therefore realised by a sequence of depositions with constant doping, interrupted by pumping cycles (stair-cases).

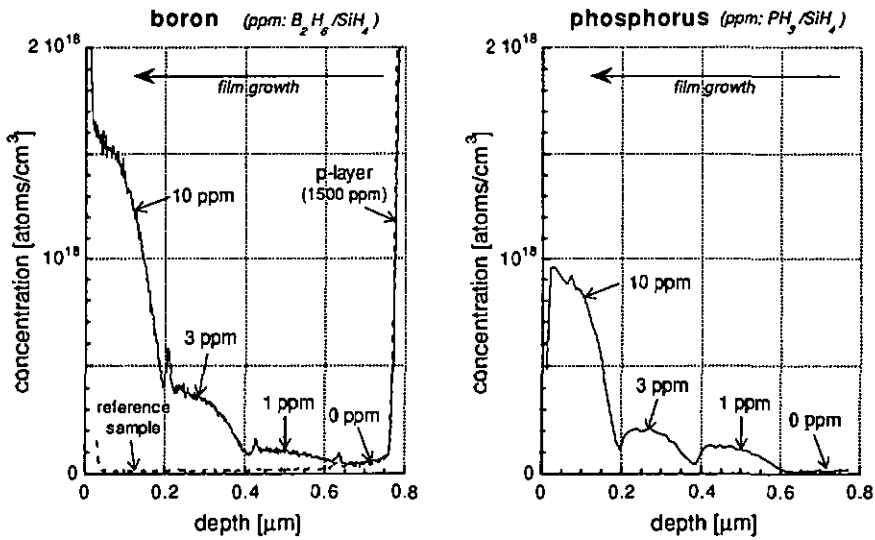

Figure 2.35: Secondary ion mass spectroscopy (SIMS) of layer stacks formed by differently doped layers, deposited on c-Si substrates. The sequence is a highly boron doped a-SiC:H layer (p-layer of Fig. 2.33/2.34, approx. 100 Å), followed by 4 low-level doped layers of 2000 Å thickness under i-layer deposition conditions (Fig. 2.30). Left: low-level boron doped stack; right: low-level phosphorus doped stack. Between each layer, the deposition is interrupted, and the chamber is pumped to a pressure of 10^{-6} mb (no plasma treatment).

Figure 2.35 shows the dopant concentrations in the solid, as measured by *SIMS* (secondary ion mass spectroscopy), of two graded doped structures. The measurements show that graded dopant concentrations in the 1-10 ppm range can be effectively controlled. Also the concentrations at the 1 ppm level are clearly above the back-ground concentration of both boron and phosphorus. The first layer of both structures is a strongly boron doped SiC p-layer. This allows to also assess the boron cross-contamination induced by the p-layer deposition (Figure 2.35, left). A decreasing boron

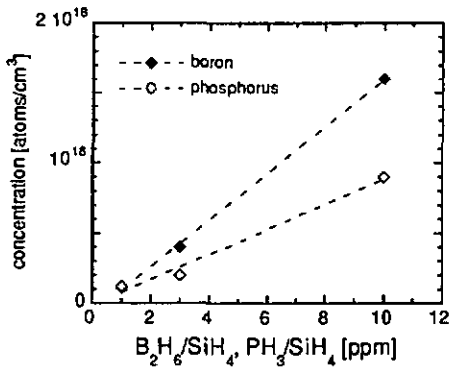

Figure 2.36: Concentration of dopants in the solid as a function of the gas phase doping, for diborane and phosphine low-level doping (solid concentrations: from SIMS data of Fig. 2.35, 'shoulder' values).

concentration is found in the zone neighbouring the p-layer. Close to the interface, the measured boron concentration is about equivalent to 0.5 ppm diborane doping. This rather high contamination could be due to the fact that for the samples of Figure 2.35 no hydrogen plasma treatment occurred after the p-layer deposition (see above). Also, the systematic errors of the SIMS analysis in resolving fast concentration changes over several orders of magnitude could lead to an overestimation of the boron concentration in the vicinity of the p-layer.
In Figure 2.36, the measured dopant concentrations in the solid are plotted as a function of the gas-phase concentration, based on the different layers of the structures of Figure 2.35. It is shown that at these low concentrations, the incorporation efficiency of the doping is independent of the doping concentration (linear correspondence). By assuming a total silicon density of $4 \cdot 10^{22}$ cm^{-3}, for both diborane and phosphine doping a dopant incorporation efficiency in a range between 1 and 2 can be derived.

2.3.5 High efficiency p-i-n solar cells

Based on the basic technology outlined above, some efforts were made to implement further elements that are known to increase the solar cell conversion efficiency:

Silicon carbide p-i buffer layers

Intrinsic, constant band-gap silicon carbide buffer layers were introduced between p- and i-layer. Figure 2.37, left, shows the effect of the buffer layer thickness on V_{oc} and fill factor. With increasing buffer layer thickness, the V_{oc} is found to increase. But beyond a certain thickness, the fillfactor rapidly decreases, defining an optimal buffer layer thickness. The analysis of the spectral response at forward voltages in fact shows that it is a reduced collection from the bulk of the i-layer that causes the fillfactor decrease, whereas the collection for the p-i interface stays high. This indicates that the buffer layers might have high defect densities, causing a loss of built-in potential at the interface.

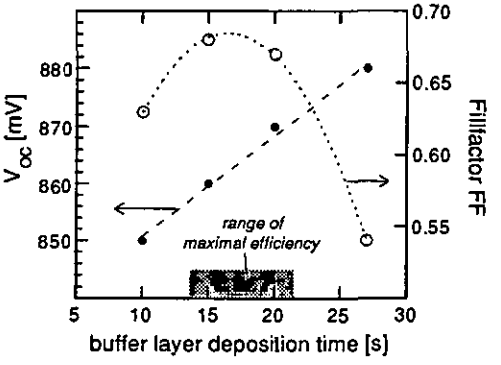

Figure 2.37: Characteristic influence of a constant band-gap a-SiC:H p-i interface buffer layer on the solar cell JV parameters. The buffer layer is deposited at 70 MHz, at a power density of 25 mW/cm^2, and at a pressure of 1 mb. The feed gas composition is SiH_4:CH_4:H_2 =1:1:3.2.

While it is generally observed that the buffer layers increase the initial state efficiencies, the role of the buffer layer regarding the solar cell stability is still debated. In some cases, the use of a buffer layer was shown to be detrimental to the stabilised solar cell performance [ARY87], on the other hand do the solar cells with the best stabilised efficiencies [ICH91] employ buffer layers. According to recent results the capability of buffer-layers in increasing the stabilised solar cell performance depends on whether they contain some small amount of boron doping [REC94]. In the present work, the main investigations on stability and low-level doping (chapters 3 and 4) were conducted on solar cells without buffer layers.

Optical confinement

To reach high efficiencies, it is further crucial to optimise the 'optical confinement' measures. The important factors are the TCO (transparent conductive oxide) coated substrate, and the back contact. Figure 2.38 shows the influence of different TCO qualities and different back contacts on the solar cell spectral response (based on identical amorphous silicon p-i-n deposition sequences). As expected, it is the absorption probability of red light that is enhanced by increased light scattering (TCO texture) and the higher back contact reflectivities. The highest total current is obtained by an optimally textured TCO (Asahi "U"), and the use of an ITO/Ag back contact.
Figure 2.39 shows the initial state JV-curve of a p-i-n solar cell, entirely deposited by VHF glow-discharge, and employing both a SiC buffer layer at the p-i interface, and an optimised optical confinement as discussed.

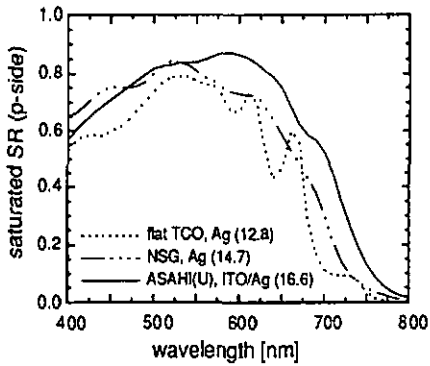

Figure 2.38: Effect of different TCO types and different back contacts on the saturated solar cell spectral response. All TCO's are SnO_2 layers. In brackets: saturated currents in mA/cm².

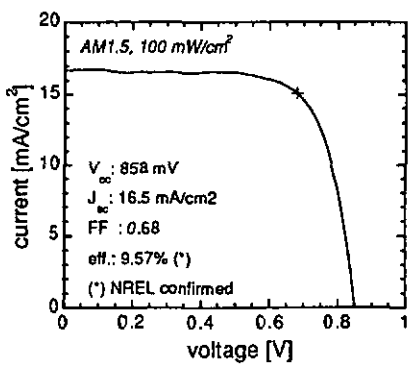

Figure 2.39: JV-curve of a high efficiency p-i-n solar cell entirely deposited by VHF-glow-discharge. The solar cell is deposited on ASAHI"U" type TCO, employing the following structure: a-SiC:H(B) p-layer (100 Å), a-SiC:H p-i buffer layer, a-Si:H i-layer (5000 Å, 4.5 Å/s), μc-Si:H(P) n-layer (300 Å), ITO/Ag back contact. The active solar cell area is 0.0625 cm². The (initial) efficiency was confirmed by NREL.

3 Light-induced degradation of amorphous silicon p-i-n solar cells

"The problem"

3.1 Issues in a-Si:H solar cell degradation

Following the discovery of amorphous silicon solar cells in 1976 (2.4 % efficiency) [CAR76], the reported solar cell efficiencies showed a rapid increase, reaching values as high as 13 % after ten years [GUH86]. Only gradually it became apparent that reported solar cell performances were not stable, but that the solar cells showed decreasing power outputs if they were exposed to light. Long-term light-exposure tests showed that the degradation slowed down with time, leading to a stabilised power output. Yet, the first commercial amorphous silicon modules exhibited poor stabilised efficiencies of only 3 - 4 %.

In the last years, the main focus of a-Si:H solar cell research has consequently been on the investigation of the mechanisms of this light-induced efficiency degradation. Sofar, there seems to be some agreement that the efficiency degradation is caused by a light-induced increase of dangling-bond defects in the amorphous silicon materials [WRO90]. Beyond that, many fundamental questions still remain open. For example, the actual microscopic mechanisms of defect creation and removal have not yet been identified. The metastability of the light-induced defects (they can be removed by thermal annealing) indicates that different processes influence the evolution of the defect concentrations. Recent investigations show that the defect densities are actually the result of competing defect creation and defect removal [YAN91, HAT92, FUJ93]. Correspondingly, defect densities tend to reach a true steady state with time, with the stabilised defect densities being a function of both the incident light intensity [YAN91, HAT92], and the sample temperature [YAN91, HAT92, FUJ93].

This view is confirmed by the results of various field tests [UCH86, CHI91, RAG92], which show a rapid slowing of the degradation after a few weeks of outdoor exposure, leading to a virtually

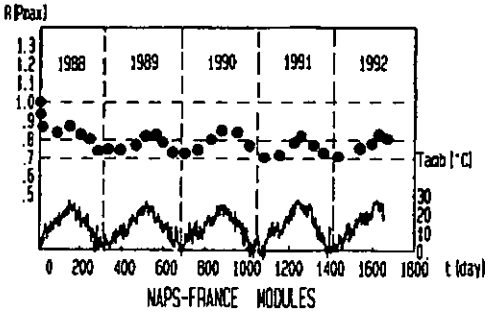

Figure 3.1: Evolution of the relative maximal power R(Pmax) of 4 amarphous silicon single-junction modules during long-term outdoor exposure. R(Pmax) = 1 corresponds to an initial module efficiency of 5.2%. T_{amb} is the daily averaged ambient temperature at the exposure site [from RAG92].

stable performance that is slightly oscillating in an annual cycle according to the seasonal ambient temperatures (higher efficiencies during summer due to a seasonal thermal annealing of the of light-induced defects, see Figure 3.1).
Besides the exploration of the degradation mechanisms in standard amorphous silicon materials, a continued effort is made in the search for new, more stable a-Si:H materials. Despite a large number of investigations, no clear-cut progress beyond what is generally called 'standard device quality material' has been achieved so far. Therefore, the question still remains open as to whether the light-induced defect densities typically found in today's best materials should be considered as a fundamental property of amorphous silicon materials, or whether alternative ways of amorphous silicon fabrication do exist that can produce materials which exhibit lower defect densities.

Current trends in increasing the stabilised solar cell efficiencies

Despite the lack of clear advances in the field of the amorphous silicon materials development, a continuous increase of stabilised solar cell efficiencies has been reported over the last years. These improvements have been realised not through a reduction of the light induced defect creation itself, but through more refined solar cell structures. The mayor improvements have been achieved by reducing the intrinsic layer thickness of the p-i-n solar cells [UCH86]. By the thickness reduction, the electric field within the i-layer is increased, and the collection probability is enhanced with respect to a thicker cell having the same defect density. In order to compensate the reduced light absorption, several cells are typically stacked to form a multijunction cell (e.g. p-i-n-p-i-n). In these stacked cells, the electric fields are higher than in a single p-i-n cell with the same total thickness, while the same amount of light is absorbed as in a single p-i-n cell (Figure 3.2). Such optimised, 2-fold stacked solar cell structures have exhibited stable efficiencies of 10 % as small area devices [JCH90], and stable efficiencies of 9 % in large area, pilot production modules [JCH92].

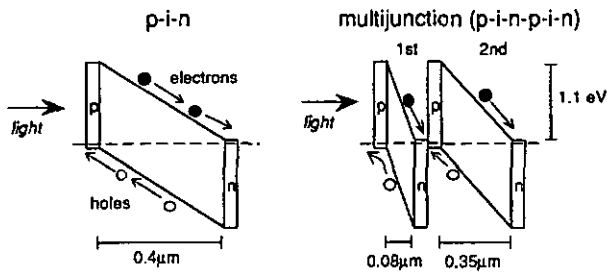

Figure 3.2: Schematic band-diagrams of single junction (p-i-n) and 2-fold multijunction (p-i-n-p-i-n) amorphous silicon solar cells.

In order to generate equal currents in both component cells of these 2-fold multijunction cells, the i-layer thickness of the first and the second cell have to be largely different; due to the rapid decrease of the generation rate produced by the sun spectrum in amorphous silicon (see Figure 2.1), the first cell i-layer thickness is only a small fraction of the i-layer thickness of the second cell. Typically, the first cell is thin enough that it virtually does not degrade, and the degradation and the stabilised efficiency of the total multijunction is determined by the stability, and thus the thickness of the second cell [BEN88]. In the solar cells reported to have the highest stabilised efficiencies to date, the optimal thickness for the second cell was found to be around 0.4 µm [ICH93] (with a first

cell thickness of the order of 0.08 μm). Similar second cell i-layer thicknesses are employed elsewhere [CAT91].
In the remaining chapters of this work, the focus will be on the investigation of the light-induced degradation (chapter 3), and of possible improvement concepts (chapter 4) for single p-i-n solar cells with these i-layer thicknesses (typically 0.5 μm), because it is the degradation of this type of cell that directly limits today's best amorphous silicon solar cell efficiencies.

Issues in stability testing procedures

Along with the discussion of the mechanisms of light-induced degradation, there have been various attempts to accelerate degradation tests by employing very high light intensities. But recent results show that under these high light intensities the solar cells degrade beyond the final efficiency they would reach under normal sun-light exposure [FUJ93, YAN93]. The capability of accelerated degradation testing to predict the degradation of normal outdoor exposure is thus questionable.
In this work, in agreement with the current trend, the solar cells were exposed to continuos illumination at intensities close to one sun for light-soaking tests. A sodium vapour light-source was used, and the intensity was adjusted to yield the same solar cell saturated currents as measured under 100 mW/cm^2 / AM1.5. The difference in the spectral distribution of the sodium lamp emission with respect to the AM1.5 spectrum was shown to have negligible influence on degradation behaviour of p-i-n solar cells in another study [BEN88]. The solar cells were at open-circuit condition during degradation; a solar cell temperature of 30°C was maintained by forced air cooling. No special care was taken to demonstrate whether or not a true stabilisation of the solar cell performance was reached; exposure times of the order of several hundred hours were assumed to give reasonable estimates of the long term solar cell performances.

3.2 *p/n collection asymmetry of degraded p-i-n solar cells*

Beside the i-layer thickness, very early also the illumination side of the p-i-n solar cell has been found to be a key factor determining the stability of a-Si:H solar cells [UCH86], with many studies showing that solar cells illuminated through the p-layer suffer much less light-induced degradation than cells illuminated through the n-layer [UCH83, AIG84, PLA84, XI85]. Since then, exclusively p-i-n solar cells illuminated through the p-layer have been further investigated and developed. But amazingly, within the mayor on-going efforts to understand and counter-act the light-induced degradation, no further detailed analysis of the actual mechanisms causing the better stability under p-side illumination has been undertaken.
In this chapter, detailed measurements of bifacial p-i-n solar cells, combined with solar cell modelling, are employed to elucidate this asymmetric degradation behaviour of the p-i-n solar cells.

3.2.1 Basic measurements

JV-curves and efficiencies

Figure 3.3 shows JV-curves of a standard p-i-n solar cell as a function of light-soaking time. The i-layer thickness is 0.5 µm. The light-soaking is with light incident from the p-side at an intensity of about one sun (see chapter 3.1). At each state of light-soaking, the JV-curves are measured for various illumination conditions: 100 mW/cm^2 / AM1.5 illumination incident from the p-side, red light (AM1.5 with $\lambda > 610$ nm) incident from the p-side, and 100 mW/cm^2 / AM1.5 illumination incident from the n-side (through a transparent ITO back-contact).
In the annealed state, the solar cell currents stay close to complete collection (saturation) far into the range of forward voltages for all illumination conditions. The different absolute magnitudes of the currents are due to the differences of the total light generated currents.
With increasing light-soaking time, the currents stay constant at reverse voltages, but continuously decrease in the forward voltage range. The degree of the current decrease is found to strongly depend on the illumination condition during the measurement: for p-side AM1.5 illumination, a relatively small reduction is observed, for the red light illumination, a larger decay is found, and for n-side AM1.5 illumination, a much stronger decay of the current collection is noted. Figure 3.4 gives the corresponding evolution of the conversion efficiency for the different spectra: For p-side AM1.5 illumination, a relative efficiency degradation of 30 % is found after 425 hours, compared to 60 % degradation for n-side AM1.5 illumination. As mentioned above, previous stability investigations showed the same characteristic difference when comparing p-i-n and n-i-p cells [UCH83, TAK86/2, XI85], with the result that since then both industry and research exclusively focused on p-side illuminated solar cells.
Before further analysis of the p/n-asymmetry is carried out, a general aspect of a-Si:H solar cell characterisation shall be illustrated through the JV-curves of Figure 3.3: In chapter 2.2 it has been argued that the JV-curve fill factor (FF), which is often regarded as a solar cell 'quality' indicator, tends to be a rather misleading quantity for amorphous silicon solar cells. This is demonstrated in Figure 3.5, where the fill factor is plotted as a function of the relative solar cell efficiency during degradation, for both p- and n-side AM1.5 conversion: A very poor correlation is found between fill factor and the efficiency for the case of the n-side solar cell measurements, with the fill factor showing a fast 'stabilisation', while the efficiency continues to degrade at longer illumination times.

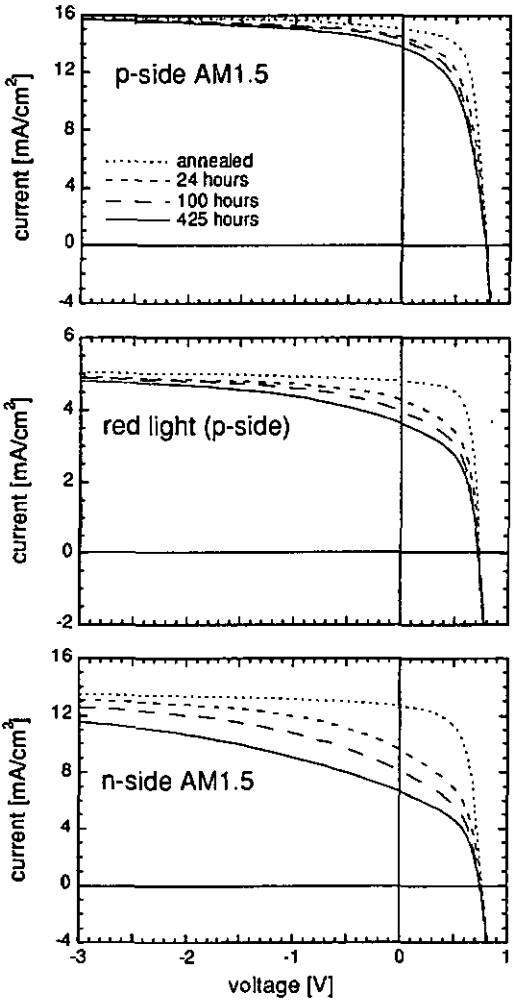

Figure 3.3: p-side AM1.5, red light (AM1.5, λ > 610 nm), and n-side AM1.5 JV-curves of a p-i-n solar cell with transparent back-contact, in the annealed state and for different times of light-soaking. Light-soaking was from the p-side, under Na-vapour lamp, at one sun intensity. The solar cell comprises an i-layer thickness of 0.5 μm, textured TCO, a-SiC:H p-layer, no p-i buffer layer, μc-Si:H n-layer, ITO back contact.

As outlined in chapter 2.2, the lack of correlation between fill factor and solar cell performance is typically due to the non-saturated short-circuit currents in amorphous silicon p-i-n solar cells. As seen in Figure 3.3, in fact during degradation the currents at 0 V (J_{SC}) undergo pronounced reductions. The degree of reduction is particularly important for the n-side AM1.5 illumination condition, thus explaining the levelling off of the fill factor as measured from the n-side.

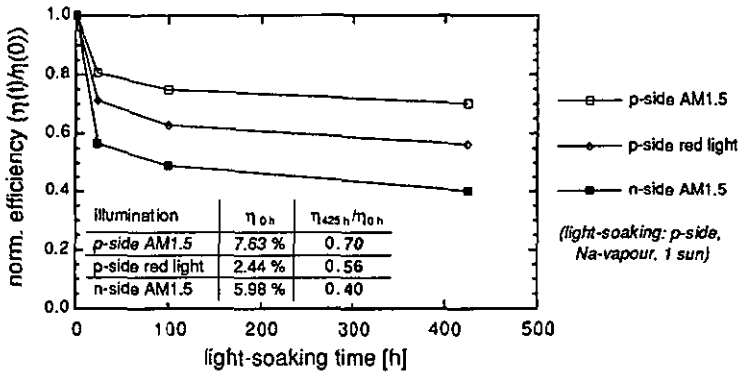

Figure 3.4: Relative efficiency change at different illuminations, as a function of light-soaking time (same data as in Figure 3.3). The corresponding initial efficiencies are given in the inset.

By referring the point of maximal power to the constant saturated current as measured at high reverse bias voltage, the saturated fill factor (FF_{sat}) was defined (Eqn. 2.48b). Figure 3.5 shows that the saturated fill factor is approximately proportional to the solar cell efficiency over the whole range of the degradation time, and independent of the relative changes in short-circuit current.

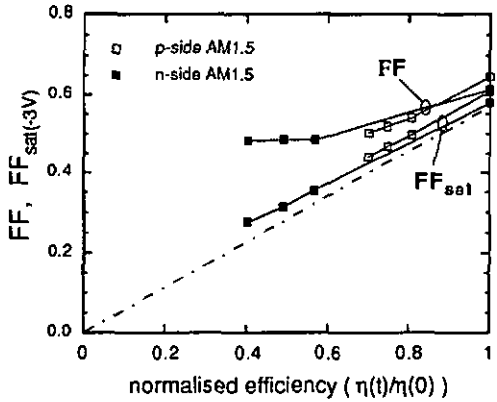

Figure 3.5: Fill factor (FF), and saturated fill factor (FF_{sat}, determined according to Eqn. 2.48b, with $J_{sat} = J_{-3V}$), versus the normalised efficiency during light-soaking, for p-side and n-side AM1.5 illumination (same data as in Figures 3.3 and 3.4).

Bifacial spectral response and DICE analysis

Figure 3.6 shows the voltage dependent spectral response, in the annealed state, and after 425 hours of light-soaking. The absolute spectral response (Figure 3.6 top) explains the lower n-side AM1.5 saturated currents as being due to a reduced short wavelength response through the ITO/n-layer absorption. All further aspects, which are related to the collection within the i-layer, are more easily analysed in the normalised spectral response; therefore, only normalised spectral response plots will

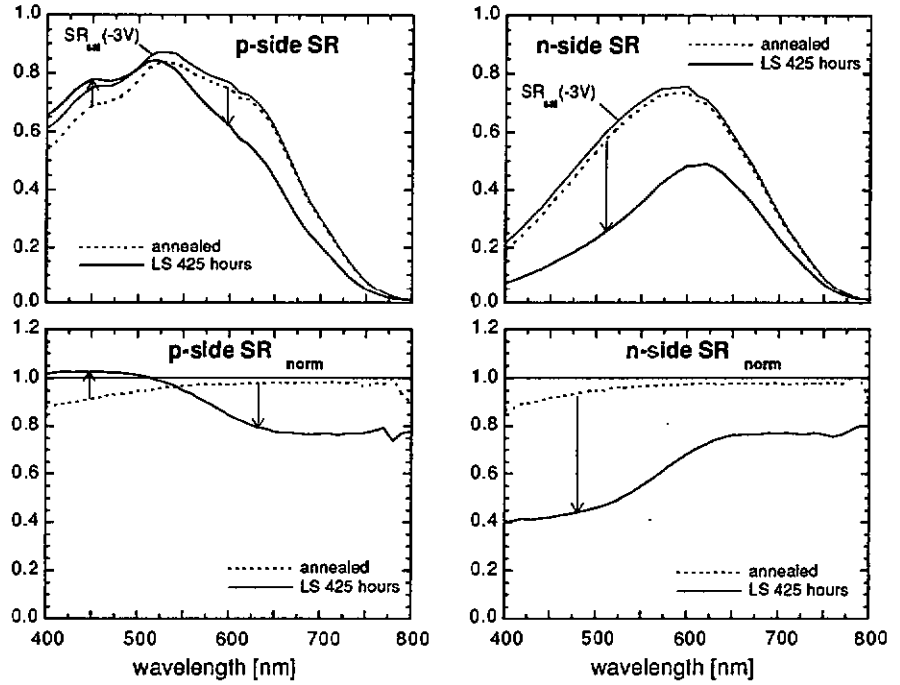

Figure 3.6: Absolute (top), and normalised (bottom, normalised with respect to -3 V), p-side and n-side spectral response at 0 V, in the annealed state, and after 425 hours of light-soaking (solar cell, and solar cell status same as in Figure 3.3). The spectral response was measured under red bias-light (λ > 610 nm).

be given in this section. Also, all spectral response measurements are performed under bias-light illumination. As shown in chapter 2.2, this is essential for the measured, differential spectral response data to be linked to the actual illuminated solar cell JV-curve. It will be shown in chapter 3.3 that this is particularly important for the present case of degraded p-i-n solar cells.

In the annealed state, the p-side and n-side collection at 0 V stay close to unity over the whole wavelength range, with exception of a minor drop at short wavelengths. This picture correlates well with the fact that the annealed state JV-curves have the same shapes even for very different illumination conditions (Figure 3.3).

After 425 hours of light-soaking, the spectral response shows pronounced wavelength dependencies: From the p-side, the collection in the long wavelength range is strongly decreased, whereas the collection in the short wavelength range is actually increased to near unity, showing a slight "SR > 1" effect (see section 2.2.2). A similar wavelength dependency of the p-side spectral response was documented in many independent investigations [UCH83, AIG84, PLA84, MIT85, KUS87, LI92, ISO94, WIN94] underlining the fact that this is a general characteristic of standard "state of the art" p-i-n cells, and not a particularity of the solar cells measured here.

The degraded state n-side spectral response shows a strongly decreased short wavelength response. The short wavelength response decreases in fact far below the long wavelength collection. Again, this spectral dependency is well documented by other investigations [UCH83, AIG84, PLA84,

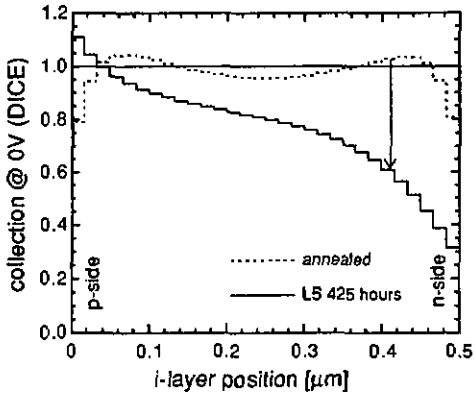

Figure 3.7: DICE collection probability as a function of the i-layer position at 0 V, in the annealed state, and after 425 hours of light-soaking. Spectral response data of Figure 3.6 was used as input for the DICE analysis (red bias light). The SVD rank is 4. the spectral response data is normalised with respect to -3 V.

KUS87] (Obviously, as the long wavelength collection represents the average collection from the whole i-layer, the n-side and p-side long wavelength collection are equal).

The p- and n-side spectral response was analysed by the bifacial DICE method (section 2.2.3). Figure 3.7 shows the resulting collection probability profiles: in the annealed state, the collection is high and uniform from the whole i-layer. After degradation, the collection is strongly asymmetric: the collection is high close to the p-i interface, and decreases monotonously with growing distance from the p-i interface, to reach its lowest value at the n-i interface.

Influence of the bias-light spectrum

The spectral response measurements (Figure 3.6) and corresponding DICE collection profiles (Figure 3.7) discussed above were determined with the solar cell illuminated with homogeneously

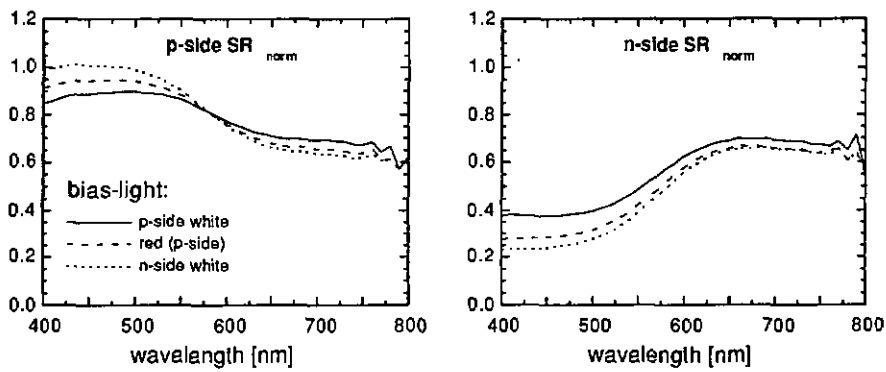

Figure 3.8: Bifacial normalised spectral response at 0V, as a function of the bias-light spectrum and direction (p-side white, p-side red, and n-side white light) of a light-soaked 0.5 μm p-i-n cell (solar cell same as in Figure 3.3, light-soaking > 500 h). The bias-light intensity was adjusted to yield a constant light-generated current of 1.2 mA/cm² for all bias-light spectra and directions.

absorbed bias-light (red light). These results are thus in principle only representative of the solar cell current under red light (see chapter 2.2.2). Figure 3.8 shows the influence of a variation of the bias-light spectrum on the spectral response of the degraded cell, covering the different illuminations used in Figure 3.3. The resulting spectra show that the overall trend seen under red light illumination, i.e. the decrease of the collection towards the n-side, is conserved under widely changing bias-light conditions. The observed amplification of the degree of p/n-asymmetry accompanying the shift of the illumination from the p- to the n-side will be discussed hereafter.

Light-intensity dependency of the collection (linearity)

The spectral response of p-i-n cells is only a differential measurement, and depends in a generalised case on the bias-light intensity (see section 2.2.2). But in the present case of a degraded cell with an i-layer thickness of 0.5 µm, the spectral response measurements are found to show virtually no dependence on the bias-light intensity over the range of intensities relevant for the normal solar cell use (see example shown in Figure 2.14). As a consequence, the degraded solar cells are expected to show a linear behaviour, i.e. solar cell currents linearly depending on the light-intensity.
This is confirmed by Figure 3.9, showing the p- and n-side AM1.5 JV-curves normalised with respect to the light intensity: the collection of the current is independent of the illumination intensity over the whole voltage range.

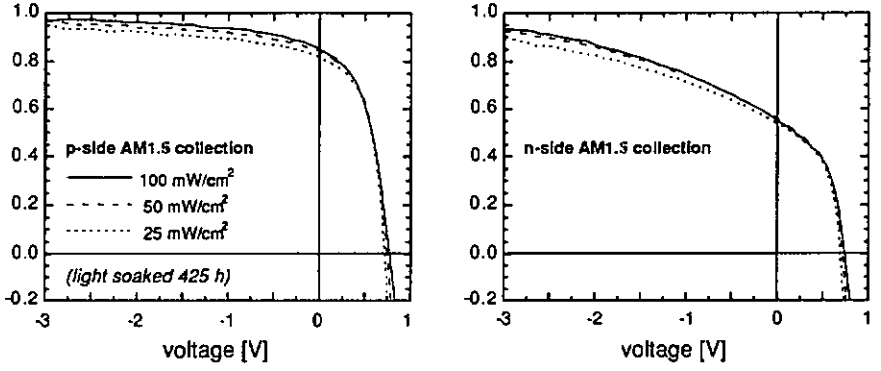

Figure 3.9: Normalised current collection (J(V)/J(-5V)) as a function of AM1.5 illumination intensity, for p-side (left) and n-side (right) illumination. The solar cell is the same as used in Figure 3.3, light-soaked for 425 hours.

With the p/n collection asymmetry shown to persist over wide ranges of bias-light spectra and intensities, it must be this asymmetry of the collection that explains the differences seen in the JV-curves between p- and n-side illumination after light-soaking (Figure 3.3):
Given the highly non-uniform generation profile of the AM1.5 light in a-Si:H (~ 50 % of the potentially absorbed photons are absorbed within the first 0.08 µm below the illuminated surface, see Figure 2.2), it is obvious that the conversion of p-side AM1.5 light is relatively insensitive to the characteristic change of the collection profile induced by the degradation. The conversion of n-side AM1.5 illumination in turn exhibits a much stronger degradation because most of the generation occurs in the n-i interface region that has a very low collection probability after degradation.

Electric field measurements

The i-layer electric field of the solar cells was measured by µs charge collection method (section 2.2.4). Figure 3.10 shows the electric field profiles in the annealed state, and after 160 hours of light-soaking, as measured from the p-side, and from the n-side. The electric field amplitudes in the annealed state indicate a relatively uniform electric field distribution over the whole i-layer (recall that away from the interfaces, the derived electric field profiles will always decrease due to the detailed measurement scheme). In the annealed state, the average of the measured electric fields is near to what is expected from a built-in potential of $V_{bi} = 1.1$ V ($2.2 \cdot 10^4$ V/cm). This indicates that there are no major errors in the annealed state electric field profiles.

After light-soaking, the electric fields are decreased in the whole i-layer. This is in contradiction with the assumption of an unchanged built-in potential before and after light-soaking (a constant built-in potential is generally assumed, as the open-circuit voltage V_{oc} does not significantly decrease under light-soaking). But as discussed in section 2.2.4, the discrepancy is explained by the influence of carrier recombination on the electric field measurement, leading to a systematic underestimation of the electric field in materials that have high recombination losses. The degree of underestimation grows with increasing distance from the measured interface.

Despite the draw-back concerning the absolute values, one can still compare the relative amplitudes of the electric fields in the light-soaked state, and one finds that the electric field is in general much stronger at the p-side than at the n-side of the i-layer. This indicates that after the light-soaking, in contrast to a symmetric electric field distribution in the annealed state, the electric field is asymmetrically distributed in the i-layer, with a higher magnitude at the p-side than at the n-side. Concerning the decrease of the electric fields towards the middle of the i-layer, it is unclear whether this reflects actually decreasing electric fields, or rather measurement artefacts due to increased recombination losses.

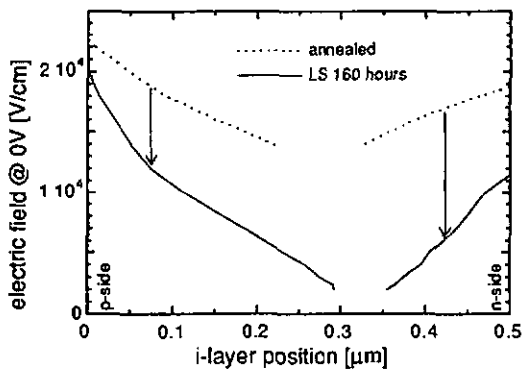

Figure 3.10: Electric field measured by the µs charge transient method (section 2.2.4), measured from the p- and the n-side, before and after 160 hours of one sun light-soaking. The solar cell corresponds to the standard cell as used in Figure 3.3. Low intensity (< 0.1 sun) red bias-light was applied during the measurement of the degraded state.

Influence of the light-soaking illumination profiles on the collection asymmetry

In the present work, as well as in many other investigations, the light-soaking was performed under a light-spectrum different from the AM1.5 solar spectrum. While it is often confirmed that these spectral differences have only minor effects on the outcome of the results [BEN88], it was elsewhere indicated that the light spectrum used for degradation has a strong influence on the resulting collection properties of the solar cells [DAL93].

In order to assess the sensitivity of the above results to the light spectrum used for degradation, a standard solar cell was degraded alternatively under three different light spectra (Figure 3.11). Strongly absorbed light incident from the p-side, light homogeneously absorbed over the whole i-layer, and strongly absorbed light incident from the n-side were applied, with the corresponding intensities adjusted to yield equal total light-generated currents in the i-layer. The spectral response shows two things:

First, the qualitative changes due to the degradation are the same for all light-soaking illuminations, i.e. the collection stays high for p-side short wavelength light, decreases for homogeneously absorbed light, and decreases even more for n-side short wavelength light. This result excludes that the collection asymmetry after the light-soaking is caused by a particular degradation spectrum only, but it demonstrates that the collection asymmetry is a general effect of the degradation in p-i-n cells.

Secondly, the illumination used for the degradation has a clear influence on the quantitative changes of the collection. With progressing shift of the illumination from the p-side to the n-side, the magnitude of the degradation does clearly increase. Light absorbed at the n-side of the i-layer thus appears to degrade the i-layer collection in the same way as light absorbed at the p-side, but the degradation is much faster. This interesting effect must be linked to the actual degradation mechanism of the solar cells itself, i.e. to the way the photogenerated carriers produce the i-layer defects. The difference seen in the 'degradation efficiency' between p-side and n-side illumination might in fact be an additional factor that impedes the use of solar cells illuminated from the n-side.

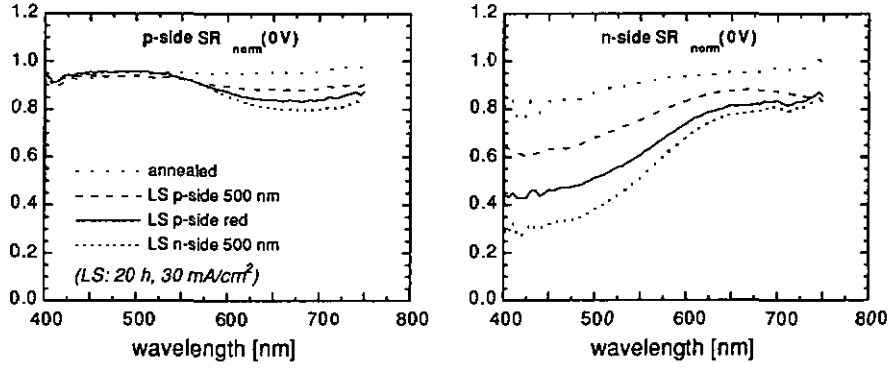

Figure 3.11: p-side and n-side normalised spectral response, in the annealed state, and after light-soaking (LS) with different illuminations: p-side 500 nm, p-side red (> 650 nm), n-side 500 nm light (the penetration depth of 500 nm light is approx. 0.05 μm). The light-soaking intensities were adjusted to yield a light-generated current of 30 mA/cm² (≈ 2 suns), the light-soaking time was 20 hours. The spectral response was measured under red bias-light.

Summarised measurement results

In summary, the above bifacial measurements of amorphous silicon p-i-n solar cells before and after light-soaking result in the following observations:

annealed state:

- the p-side and n-side solar cell performance under the AM1.5 spectrum are almost equal (differences are due to purely optical differences)
- the carrier collection is constant in the whole i-layer, and decreases uniformly at high forward voltages
- the electric field distribution is symmetric and nearly constant over the whole i-layer

after light-soaking:

- the n-side AM1.5 solar cell performance is decreased much stronger than the p-side performance
- the carrier collection is high at the p-*i* interface, and decreases gradually in the *i*-layer to reach a minimum at the n-i interface
- the carrier collection patterns, and the large signal JV-curves are linear, i.e. they show a non intensity-dependent behaviour
- the degree of the p-n collection asymmetry depends on the spectrum of the solar cell bias-light: under n-side bias-light the difference between the p- and the n-side collection is increasing, under p-side bias-light the difference is reduced; the asymmetry however persists for all bias-light conditions
- the electric field is higher at the p-side than at the n-side
- the same kind of p-n collection asymmetry is produced by both p-side or n-side light-soaking with strongly absorbed light
- the degradation of the carrier collection due to light absorbed at the n-side of the i-layer is stronger than the degradation due to light absorbed at the p-side (at a constant light-dose absorbed in the i-layer)

3.2.2 Collection asymmetry due to i-layer dangling-bonds and asymmetric carrier mobilities

Recombination and space-charge effects of the dangling-bonds

The degradation of amorphous silicon p-i-n cells is generally considered to be caused by an increase of the dangling-bond concentration in the i-layer (the alternative model of pure interface degradation is addressed, and discarded in section 3.3). The dangling-bonds influence the collection of carriers from the solar cell i-layer in two ways. Firstly, they represent an efficient pathway of carrier recombination, which directly competes with the collection of the photocarriers (Eqn. 2.6 and 2.7). And secondly, by capturing free carriers, the dangling-bonds accumulate considerable space-charge densities that distort the distribution of the electric field within the i-layer (Eqn. 2.3).

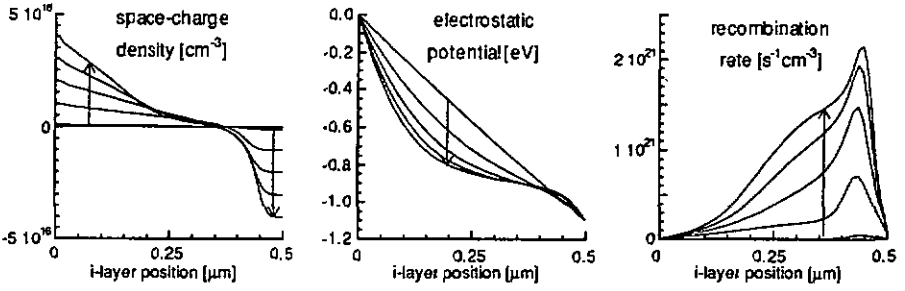

Figure 3.12: Numerically simulated dangling-bond charge, electrostatic potential, and recombination rate as a function of the i-layer position, for increasing dangling-bond densities. The arrows mark the evolution of N_{DB} over 0.1, 1, 2, 3, and 4 times 10^{16} cm^{-3}. The dangling-bond concentrations are homogenous over the whole i-layer. The illumination is homogeneously absorbed light generating 16 mA/cm^2, the external voltage is 0 V. The tail-states are not simulated, the other material parameters correspond to the standard parameters of Table 2.1.

Figure 3.12 shows the numerically simulated influence of an increasing i-layer dangling-bond concentration. The i-layer space-charge is seen to increase due to charged dangling-bonds. The highest charge concentrations are found towards the interfaces, where all local dangling-bonds are charged according to the local majority carrier polarity. The increasing space-charge leads to a progressing distortion of the electrostatic potential distribution, transforming the initially constant slope to a distribution having high electric field peaks at the interfaces, and low fields in the bulk of the i-layer. The carrier recombination increases accordingly, with the increase specially pronounced in those bulk regions that have a nearly flat electrostatic potential.

Asymmetric free carrier mobilities

The measurements have shown that after degradation, the collection from within the i-layer is not only reduced, but that the reduction occurs in a distinctly asymmetric way, resulting in an almost stable, high collection at the p-side of the i-layer, and increasing collection losses towards the n-side. If one assumes that the dangling-bonds have symmetric properties with respect to the two carrier polarities (position at mid-gap, amphoteric behaviour with equal cross sections for both electrons and holes), the dangling-bonds alone cannot be the cause of the p/n-asymmetry.

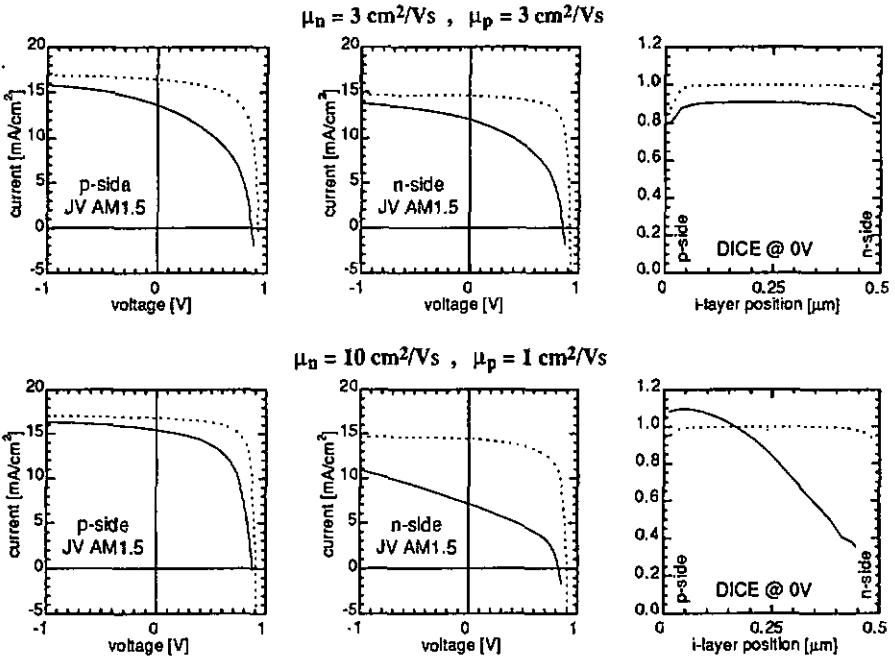

Figure 3.13: Numerically simulated JV-curves and collection profiles for different free carrier mobilities, for a dangling-bond density of $1 \cdot 10^{15}$ cm^{-3} (dotted lines), and of $2 \cdot 10^{16}$ cm^{-3} (full lines). The collection profile is simulated with 16 mA/cm^2 homogeneously absorbed light. All other parameters correspond to the standard parameters of Table 2.1 (w/o tail-states).

A most commonly admitted p/n-asymmetry of the a-Si:H material is a difference in the free carrier mobilities, with a higher electron than hole mobility. The proposed differences include factors ranging from 2 to 20 [e.g. STR91]. Figure 3.13 shows the influence of the degradation on the simulated p- and n-side AM1.5 JV-curves, and on the i-layer collection probabilities for a case with equal mobilities for electrons and holes, and for a case with the electron mobility 10 times higher than the hole mobility. The product of the two mobilities was kept constant to yield overall approximately constant losses. The annealed state and the degraded state are modelled with the respective, constant i-layer dangling-bond densities of $1 \cdot 10^{15}$ cm^{-3} and $2 \cdot 10^{16}$ cm^{-3} (see below).
In the case of equal mobilities, a symmetric behaviour is seen as well in the JV-curves as in the i-layer collection, independent of the defect density. For the case of a higher electron over hole mobility a relatively symmetric behaviour of the annealed state (low simulated defect density) is reversed in a clear asymmetric behaviour after degradation (high simulated defect density). Both the modelled changes of the JV-curve shapes and of the i-layer collection behaviour (e.g. the tendency to collection higher than unity in the p-i interface region after degradation, see also below) reproduce well the trends of the corresponding measurement results of Figures 3.3 and 3.7.
This model, employing a mobility difference and a constant density of amphoteric i-layer defects to explain the collection asymmetry, shall be analysed and discussed in the following. Some alternative explanations of a p/n-asymmetry that do not require to presume asymmetric mobilities will be addressed in later, separate sections. In these sections, explanations based on the tail-states,

on extrinsic i-layer charges, or on the degradation of interfaces will be discarded. Obviously, more subtle alternatives might also be based on an asymmetry in the properties or distribution of the dangling-bonds themselves (asymmetric cross sections for electrons and holes, energy distribution off mid-gap, non-amphoteric nature). Even a combination of several of the mentioned factors could be considered, as it was in the past often done in numerical modelling studies [KOP92]. But given the overall high uncertainty of the employed models in general, it seems more useful to concentrate on the simple concept of a mobility difference alone, and to investigate to what extent this concept can explain the measured solar cell behaviours.

The detailed influence of the mobilities on the degraded state operation of the p-i-n solar cell is illustrated in Figure 3.14. Free carrier densities, dangling-bond charge, electric field, and electrostatic potential are given for the two cases of equal and different mobilities treated above (Figure 3.13). Carrier mobilities affect most directly the free carrier concentrations. In an illuminated solar cell, the currents are imposed by the generation rate (Eqn. 2.6/2.7) that is equal for both electrons and holes. The local carrier concentrations are directly proportional to the respective light-induced currents, with the proportionality factor being the carrier mobility (Eqn. 2.4/2.5, neglecting the carrier diffusion). The resulting carrier concentrations in the i-layer are thus high for carriers with a low mobility, and lower for carriers with a high mobility.

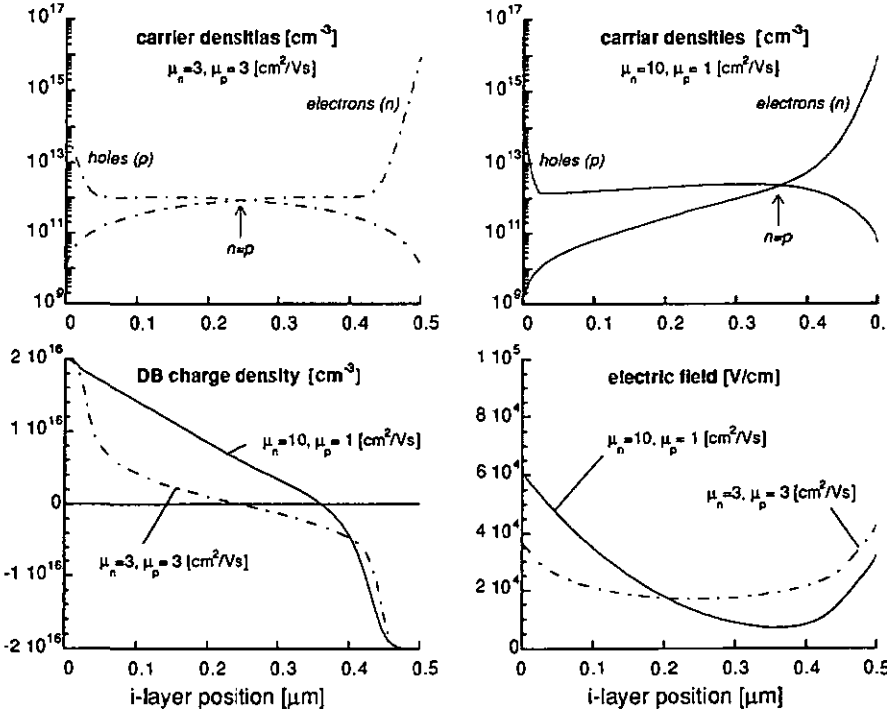

Figure 3.14: Numerically simulated carrier densities, dangling-bond charge, electric field, and electrostatic potential as a function of the i-layer position, for equal, and differing carrier mobilities for electrons and holes. The illumination is homogeneously absorbed light generating 16 mA/cm^2, the external voltage is 0 V. The dangling-bond density is 2·10^{16}cm^{-3}. All other parameters correspond to the standard parameters of Table 2.1 (w/o tail-states).

The plots of the carrier concentrations in Figure 3.14 (top) illustrate this mechanism: the hole concentration rises with the hole mobility reduced from 3 to 1 cm^2/Vs, and the electron concentration falls with the electron mobility rising from 3 to 10 cm^2/Vs. As a result, the concentration of holes becomes higher than the concentration of electrons over most of the i-layer in the case of a higher electron over hole mobility. This asymmetry in the carrier concentrations leads to a distinct effect on the dangling-bond charge distribution over the i-layer. In contrast to the case of equal mobilities, the higher hole concentration leads to a large increase in the depth of the positive space-charge. Due to these additional positive space-charge contributions in the centre of the i-layer, the electric field takes a strongly inhomogeneous distribution, with a high increase over the average (annealed state) electric field at the p-side, and a strongly reduced electric field in the back of the i-layer. It is this major asymmetry of the electric field due to a dominant positive dangling-bond charge that leads to the p/n asymmetries of the modelled i-layer collection and JV-curves of Figure 3.13. Also, the model of a dominating positive space-charge explains the measured difference between the p- and n-side electric field in the light-soaked p-i-n solar cells (Fig. 3.10).

Effect of changing i-layer carrier generation profiles

The deduction of a dominating positive space-charge and a corresponding non-uniform electric field, as demonstrated in Figure 3.14, has been made for the simplified case of a homogenous generation rate in the i-layer (red light). Under the illumination spectra that create high generation peaks close to the interfaces (like e.g. the AM1.5 solar spectrum), the different resulting carrier concentrations in the i-layer could be argued to lead to largely different space-charges and electric fields. Figure 3.15 shows the range of modification of the space-charge and the electric field, if in the numerical simulation the illumination is changing from p-side AM1.5 over red light to n-side AM1.5. If the generation is mostly at the p-side (p-side AM1.5), the ratio of free holes over electron densities decreases in the bulk of the i-layer. As a consequence, the simulations show a shrinking positive space-charge, and the electric field peak at the p-i interface is reduced in favour of a higher field in the back of the i-layer. The overall electric field asymmetry is reduced, but still the electric fields are the highest in the vicinity of the p-i interface. The change from red to p-side AM1.5

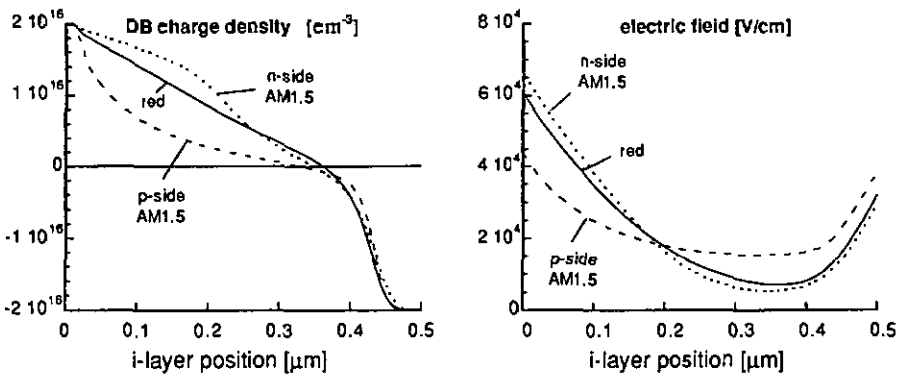

Figure 3.15: Numerically simulated dangling-bond charge and electric field as a function of the i-layer position, under illumination with p-side AM1.5, with homogeneously absorbed (red), or with n-side AM1.5 light. The external voltage is 0 V. The dangling-bond density is $2 \cdot 10^{16}$ cm^{-3}. All other parameters correspond to the standard parameters of Table 2.1 (w/o tail-states).

illumination thus does not reverse the trends observed under red light. While changing from red light to AM1.5 light incident from the n-side, the hole concentrations in the bulk increase, the positive space-charge grows further, and the electric field asymmetry increases.
The influence of the illumination spectrum on the electric field seen in the simulation can explain different features of the measured solar cell collection. The measured collectioos in Figure 3.8 have shown that the general trend of a high collection at the p-i interface and a reduced collection towards the n-side is conserved for all illumination spectra. This is in agreement with the fact that in the numerical simulation, independent of the generation spectrum, the electric fields always remain higher at the p-side than in the bulk and at the n-side. Figure 3.8 also shows that the difference between the p-side and the n-side collection gradually decreases as the generation shifts from the n-side towards the p-side. This is consistent with the behaviour seen in the simulated electric field, showing an increasing field inhomogeneity while the generation is shifted towards the n-side.

Collection higher than 100 % in the p-i interface region

Degraded solar cells were found to exhibit a collection higher than 100 % for short wavelength light incident from the p-side (Figures 3.6/3.7/3.8). This can be easily understood based on bias-light dependent electric field distribution of Figure 3.15. As discussed in section 2.2.2, the 'SR > 100 %' behaviour is due to an enhancement of the collection of the bias-light carriers by the probe-light, with the enhanced bias-light current increasing the probe-light collection beyond 100 %.
Under red (bias-)light illumination carriers accumulate and recombine in the low electric field region in the back of the i-layer. If in this situation the p-side spectral response for blue light is measured, the additional generation by the probe-light in the p-i interface region causes a differential increase of the electric field in the bulk of the i-layer (corresponding to a shift from the red towards the p-side AM1.5 illuminated case in Figure 3.15). This electric field increase in the bulk improves the overall electric field distribution in the i-layer, and thus differentially increases the collection probability of the red bias-light. In the present case, the efficiency of one probe-light carrier to cause the collection of one additional bias-light carrier is probably rather low (of the order of 10 %), but this small additional contribution is enough to increase an already high collection probability of the blue probe-light to values greater than 100 %.

Absolute number of the defect density, and its impact on the modelled solar cell behaviours

For the numerical simulations made in this section, the degraded state of the solar cells was modelled by an i-layer dangling-bond density of $2 \cdot 10^{16}\,cm^{-3}$. This value might appear rather low with respect to some numbers found in a-Si:H film measurements, where frequently values higher than $10^{17}\,cm^{-3}$ are cited [e.g. ISO92].
The performance of a modelled, defect limited solar cell depends in a first approximation only on the product of the dangling-bond density and dangling-bond cross section. This product is the pre-factor of the total recombination (Eqn. 2.27), and therefore determines directly the magnitude of the recombination losses in a modelled solar cell. In the present work, a fit of the measured red light JV-curve after 425 hours of light-soaking (Figure 3.3) was used to approximately determine this product. With electron and hole mobilities of 10 and 1 cm^2/Vs, $N_{DB} \cdot \sigma_{DB}^{0} \cdot v_{th} \approx 3 \cdot 10^{8}\,s^{-1}$ was found.

The question arises then of how to distribute the recombination rate between the density of the dangling-bonds, and their cross section. Concerning the above modelling results, the use of dangling-bond densities greater than $2 \cdot 10^{16}$ cm^{-3}, with correspondingly lower cross sections, was found in general to intensify the effects due to the electric field. At defect densities equal or higher than 10^{17} cm^{-3}, the modelled behaviours started to exhibit clear discrepancies to the measurements, such as unrealistically high 'SR > 100 %' behaviours.

A better alternative to a detailed parameter fitting is obviously the direct determination of the searched dangling-bond densities in an independent measurement. In the present work, two different measurements of the dangling-bonds density are proposed (sections 3.3 and 4.3). These measurements, which are directly performed in the degraded solar cells, consistently show values in the lower 10^{16} cm^{-3} range. This leads to the conclusion that this is the correct defect density for the degraded p-i-n solar cell case. To approximately reproduce the recombination losses seen in the measured degraded state JV-curves, consequently a dangling-bond cross section of 10^{-15} cm^2 was adopted for the solar cell model (see standard modelling parameters of Table 2.I).

Cross section ratio of neutral and charged dangling-bonds: influence on the space-charge

For a fixed product of dangling-bond density and neutral dangling-bond cross section, the major remaining parameter determining the dangling-bond behaviour under illumination (i.e. with neglected emission from the mid-gap defects) is the ratio of the cross sections (C) of charged and neutral dangling-bonds. Typically, the cross sections of charged states are modelled larger than the cross sections of neutral states in order to account for additional coulombic attraction of the charged state. In a-Si:H, widely varying ratios, including ratios of C > 100 [e.g. WYR92], were being inferred from different film measurements. In the above simulations, a ratio C = 10 was used. Figure 3.16 shows the simulated influence of the cross section ratio on the degraded state space-charges, and electric fields.

With increasing cross section ratio, the space-charges are decreasing, and the electric field distortion is reduced. This is because the increased cross section lowers the occupation probability of the dangling-bonds by a positive or negative charge. The basic electric field asymmetry, induced

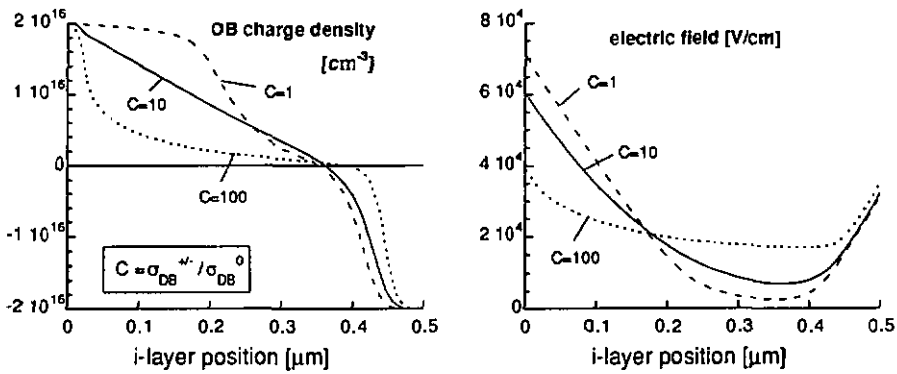

Figure 3.16: Numerically simulated dangling-bond charge and electric field as a function of the i-layer position, for different cross section ratios of the dangling-bonds. The cross section of neutral dangling-bonds is $1 \cdot 10^{-15}$cm^2 for all cases. Illumination is with homogeneously absorbed (red) light, the external voltage is 0 V, the dangling-bond density is $2 \cdot 10^{16}$cm^{-3}. All other parameters correspond to the standard parameters of Table 2.I (w/o tail-states).

by the different mobilities, is however found to persist, with its magnitude only lowered by a high cross section ratio. For a lower cross section ratio, the space-charges further increase in the centre of the i-layer, enhancing the electric field distortion.

Triangle shape of the positive space-charge

The triangle shaped positive space-charge for the case of the cross section ratio C = 10, and under homogeneously absorbed red light (Figures 3.14/3.15/3.16), can be shown to be characteristic of the ratio of the mobilities (C_μ) being equal to the ratio of the cross sections (C). By using a few approximations, the problem can be addressed by analytical considerations:
For a constant electric field, and a homogenous generation in the i-layer, the position dependent ratio of holes over electrons becomes approximately

$$\frac{n(x)}{p(x)} = \frac{1}{C_\mu}\left(\frac{x}{L-x}\right) \qquad (\text{with} \quad C_\mu = \frac{\mu_n}{\mu_p}) \tag{3.1}$$

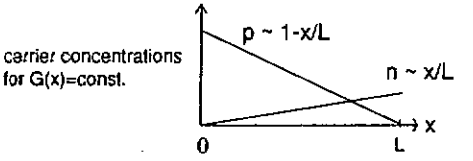

Figure 3.17: Schematic carrier concentrations in the i-layer, for constant generation rate G(x) (red light), constant electric field, no recombination, and for a hole mobility smaller than the electron mobility (no influence of the contacts).

The positive occupation of the dangling-bonds f^+ (Eqn. 2.24 and 2.25), if the emissions are neglected (Eqns. 2.25: e = 0), becomes

$$f^+ = \frac{1}{1 + C\frac{n(x)}{p(x)} + \frac{n(x)^2}{p(x)^2}} \approx \frac{1}{1 + C\frac{n(x)}{p(x)}} \tag{3.2}$$

With Eqn. 3.1 in Eqn. 3.2,

$$f^+ \approx \frac{1}{1 + \frac{C}{C_\mu}\left(\frac{x}{L-x}\right)} \tag{3.3}$$

And finally, for $C = C_\mu$, the positive dangling-bond occupation f^+ is found to take the triangle-shape seen in the above simulations

$$f^+ \approx \frac{1}{1 + \frac{x}{L-x}} = 1 - \frac{x}{L} \tag{3.4}$$

This analysis shows that despite elevated cross section ratios C, non-negligible charging of the dangling-bonds will occur in the central regions of the i-layer if the ratio of the mobilities C_μ is high as well. And it is those charges in the central region of the i-layer, even if they are lower in magnitude than those at the doped layer interfaces, that eventually govern the overall i-layer electric field distribution.

Summary on the modelling of the p/n asymmetry

In summary, it can be stated that the p/n asymmetry observed in the p-i-n solar cell performance after degradation is consistent with a constant density of amphoteric dangling-bond defects in the whole i-layer, and a free hole mobility smaller than the free electron mobility. In this model, a predominant positive charging of the dangling-bond defects in the centre of the i-layer leads to an electric field that is high towards the p-i interface, and low on the n-side of the i-layer.
With this model, the following measured features of light-soaked p-i-n solar cells are explained:

- asymmetric solar cell performance for p- and n-side illumination
- decreasing collection from p-side to n-side of the i-layer
- electric field asymmetry after light-soaking
- enhancement of the collection asymmetry under n-side bias-light, and reduced asymmetry under p-side bias-light (as compared to homogeneously absorbed bias-light)
- collection larger than unity effect in the p-i interface region, especially under red and n-side bias-light
- linear behaviour of the light-soaked state JV-curves (no intensity dependency)

With free electron and hole mobilities of 10 and 1 cm^2/Vs, and a dangling-bond density in the lower $10^{16}\,cm^{-3}$ range, a reasonable correspondence to the measured solar cell results can be found. Higher dangling-bond densities are found to further intensify the electric field distortions. The size of the positive dangling-bond space-charge in the central region of the i-layer is found to arise from a competition between the mobility ratio, and the ratio between the charged and neutral dangling-bond cross sections.

3.2.3 Assessment of the influence of the band-tail states

The non-linear behaviour of the band-tail states

The density of states in the valence-band tail is most commonly considered to be more important, and to start more deeply in the gap than the corresponding states at the conduction-band side. The influence of this p/n-asymmetry of the a-Si:H material on the p-i-n solar cells shall be investigated in the following section, in order to evaluate its possible influence on the i-layer collection.
Like the dangling-bonds, the tail-states influence the solar cell by contributing to both the i-layer space charge, and to the i-layer recombination. Due to their steeply rising densities in the neighbourhood of the band-edges, the tail-states exhibit however a very particular behaviour. Unlike the dangling-bond states, both recombination and charge depend here strongly on the absolute levels of the locally prevailing carrier densities. This is because the close vicinity of tail-states to the band-edge allows for a fast re-emission of captured carriers: For low carrier densities, the emission is much faster than the capture of carriers, and consequently the states are mostly empty, leading to low space-charge, and low recombination. With increasing carrier densities, the tail becomes more occupied, and space-charge and recombination rates increase accordingly. For the valence-band tail, this behaviour is easily illustrated by using the following simplifications:

$$p \approx a_p I \quad \text{(I: light intensity)}$$
$$n \approx a_n I$$
$$kT/E_{OV} \approx 0.5 \qquad (3.5\text{ a-d})$$
$$\sigma_n = \sigma_p$$

With these simplifications, the valence-band tail charge (Eqn. 2.41) and recombination (Eqn. 2.42) are found to scale with the illumination intensity in the following way (the behaviour of charge and recombination of the dangling-bonds, from Eqns. 2.26/27, is given in brackets)

$$Q_{VBT} \sim \sqrt{I} \qquad (Q_{DB} = \text{const} \neq f(I)) \qquad (3.6)$$

$$R_{VBT} \sim I^{\frac{1}{2}} \qquad (R_{DB} \sim I) \qquad (3.7)$$

From these expressions one expects pronounced intensity dependency, or 'non-linearity', of the solar cell operation in cases where the valence-band tail-states govern the solar cell operation. This contrasts the dangling-bonds governed operation, where no intensity dependency is expected.
The conduction-band tail could also cause an intensity dependent behaviour. But due to the difference in the distribution of the two tails, the onset of valence-band tail effects is expected at much lower carrier densities than the onset of a noticeable influence of the conduction-band tail.
If on the other hand the solar cell operation is governed by the charge and recombination of the dangling-bonds, a non intensity dependent, 'linear' behaviour is expected, as indicated above by a constant space-charge and a recombination proportional to the light intensity.
In degraded solar cells with a 0.5 µm thick i-layer, no marked intensity dependencies were found at standard one sun light intensities (Figure 3.9). From this it is concluded that the major p/n-asymmetry found in the i-layer collection after the degradation is neither caused by band-tail charge, nor by band-tail recombination.

Analysis of the collection at high intensities, and for thick i-layers

In order to assess under which conditions, if at all, the tail-states influence the operation of p-i-n cells, the analysis range was extended: Since no intensity dependencies were noted at one sun intensities, the onset of tail-state non-linear effects is expected to be at higher intensities. Also, p-i-n cells with thicker i-layers should be more sensitive to small space charge densities. Figure 3.20 shows the normalised current collection of an annealed p-i-n solar cell with a 2 µm thick i-layer, for illumination intensities from 6.25 to 250 mW/cm^2 AM1.5 light, for p- and n-side illumination. For this i-layer thickness, the AM1.5 spectrum can be considered as mostly absorbed near the illuminated interface. Under p-side illumination, electrons are thus majority carriers in most of the i-layer, leading to occupation of and thus sensitivity to the conduction-band tail, whereas for n-side illumination, holes are majority carriers, and the sensitivity is to the valence-band tail.

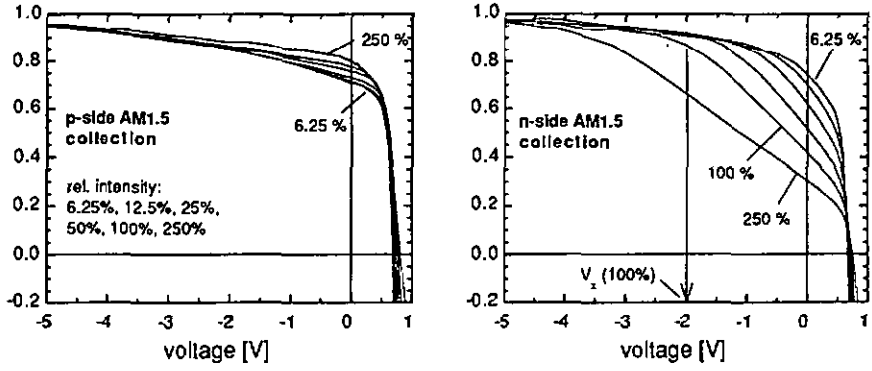

Figure 3.20: Current collection in a p-i-n solar cell with an i-layer thickness of 2 µm, for p-(left) and n-side (right) AM1.5 illumination with different intensities. 100 % intensity corresponds to 100 mW/cm^2. The solar cell is identical with the standard cell used in Figure 3.1, with exception of the i-layer deposition time. The solar cell is in the annealed state.

For the case of n-side illumination, the collection exhibits a very pronounced intensity dependency: with increasing intensity, the current collection is steadily decreasing. This reduction of the collection as a function of the increasing hole concentration seems thus to indicate a valence-band tail effect (Remark: the marked n-side intensity dependency represents a typical case of 'non-linear' solar cell behaviour; the bias-light dependent spectral response of the cell shown in Figure 3.20 is given in Figure 2.14, case 1).

For p-side illumination on the other hand, the collection remains largely independent of the intensity. The electron concentrations generated by the p-side illumination are thus too small to cause a notable occupation of the conduction-band tail.

The particular shape of the n-side collection is worth further considerations: At low intensities, the shape of the collection curve is very similar to what is typically found in thin cells, i.e. the collection drops in the characteristic exponential way at high forward voltage only (it should be considered that the collection at -3 V corresponds to the collection at 0 V of a 0.5 µm cell due to the reduced electric field). At higher intensities, the collection curves show a clear, threshold-like deviation from the low intensity curve, and the collection drops in a linear characteristic with

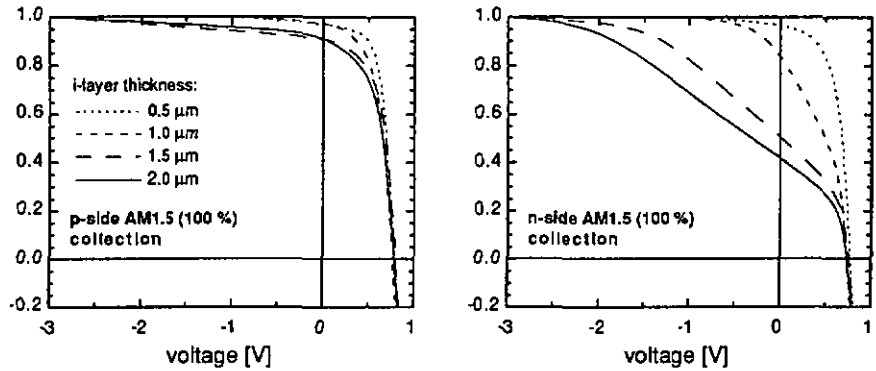

Figure 3.21: Current collection p-i-n solar cells for p-(left) and n-side (right) AM1.5/100 mW/cm^2 illumination, as a function of the i-layer thickness. The solar cell are identical with the standard cell used in Figure 3.1, with exception of the i-layer deposition time. The solar cells are in the annealed state.

increasing forward voltage. The threshold voltage of the deviation moves towards higher negative voltages with increasing intensity.

Figure 3.21 shows the collection at a constant intensity (100 mW/cm^2 AM1.5) for p-i-n cells with varying i-layer thickness. As a result the characteristic reduction of the n-side current collection gradually vanishes with decreasing i-layer thickness. For the cell with a 0.5 µm i-layer, the threshold and the characteristic linear shape of the collection curve are no more discernible.

Analytical model of the threshold voltage

Threshold-like behaviour in the JV-curves are a manifestation of electric field effects rather than of pure recombination effects: This is because effects due to recombination alone have to be gradual effects, which manifest themselves in the voltage dependent collection by the typical exponential 'Hecht-curve' shape. The electric field, or space-charge effects on the other hand can have sharp, threshold like effects if the potential distribution within the p-i-n cell interferes with limits imposed by the doped layer potentials (for other examples of threshold-like effects in the p-i-n solar cell collection see sections 3.3 and 4.2).

The threshold effect of the n-side collection can be explained as follows: At very low intensities, the hole density necessary to support the i-layer photocurrent is small, and the corresponding positive valence-band tail space-charge is small as well. In particular the total positive charge in the i-layer is small enough such that the electric field can still extend to the n-i interface. In this situation, approximately the whole photocurrent is collected. With increasing illumination intensity, the hole concentration in the i-layer is increasing further, and therefore the positive band-tail space-charge increases, until the electric field at the n-i interface is totally cancelled. Further illumination increase leads to an increasing fraction of the photocurrent being lost in the low field region. The actual growth of the losses, once the electric field is cancelled, is difficult to model. The model would have to take into account the detailed balance between the remaining, collected photocurrent that supplies the i-layer space-charge, and the photocurrent loss that reduces the space-charge.

An analytical model for the value of the threshold voltage is found as follows: The expression for the one sided abrupt junction [SZE85] relates a constant charge density to the total voltage drop over the space-charge region (V_i) and the space-charge width (w).

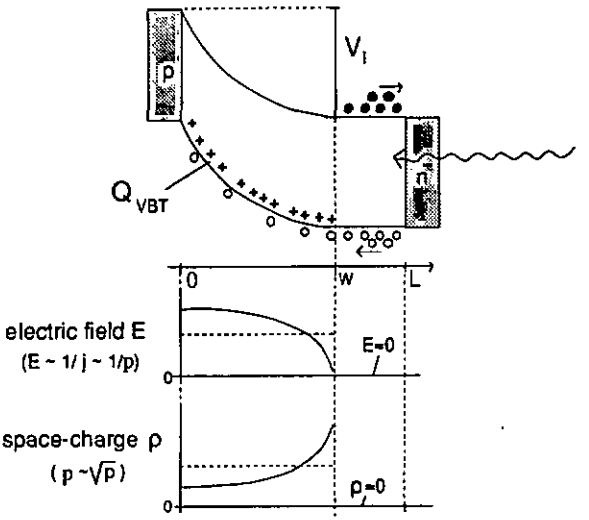

Figure 3.22: Schematic influence of the valence-band tail space-charge on the collection of n-side illumination with strongly absorbed light.

By assuming, in a simplifying manner, that the valence-band tail charge Q_{VBT} is constant, one obtains:

$$Q_{VBT} = \frac{2 \cdot \varepsilon \cdot V_j}{q \cdot w^2} \tag{3.8}$$

The relation between the carrier densities, and the valence-band tail charge (Eqn. 2.41) can also be simplified, by assuming p >> n in the space charge region, and $kT/E_{0V} \approx 0.5$:

$$Q_{VBT} = N_{VBT0} \cdot E_{0V} \cdot \left[\frac{p}{N_V}\right]^{0.5} \tag{3.9}$$

Further, by assuming an average electric field in the space-charge region ($E \approx V_j/w \approx$ const), the concentration of the holes in the space-charge region p is linked to the hole current j_p:

$$p = \frac{j_p}{q \cdot \mu_p \cdot E} = \frac{j_p \cdot w}{q \cdot \mu_p \cdot V_j} \tag{3.10}$$

At first glance, the approximations could appear too crude. But a closer look shows that the balance of electric field distribution and space-charge will automatically lead to an electric field distribution somewhere between a parabolic potential (with a constant space-charge), and a linear potential (with a constant current, but with the space charge only at the right end of the field zone).
For the threshold condition, the space-charge width w is equal to the i-layer thickness: w = L; and voltage drop over the space charge is the threshold voltage: $V_j = V_x$. From Eqns. 3.8 - 3.10, by elimination of p and Q_{VBT} , one obtains the following expression for the threshold voltage:

$$V_x^3 = \frac{q \cdot (N_{VBTO} \cdot E_{0V})^2}{4 \cdot \varepsilon^2 \cdot \mu_p \cdot N_V} \cdot L^5 \cdot j_p \tag{3.11}$$

predicting the following proportionalities of the threshold voltage

$$V_x \sim L^{\frac{5}{3}} \tag{3.12}$$

$$V_x \sim j_p^{\frac{1}{3}} \tag{3.13}$$

Figure 3.23 demonstrates that the measured threshold voltages in fact follow the i-layer thickness and intensity dependencies predicted by Eqn. 3.12 and 3.13 (note that with all light absorbed close to the n-i interface, the hole current j_p is proportional to the experimental light-intensity I).

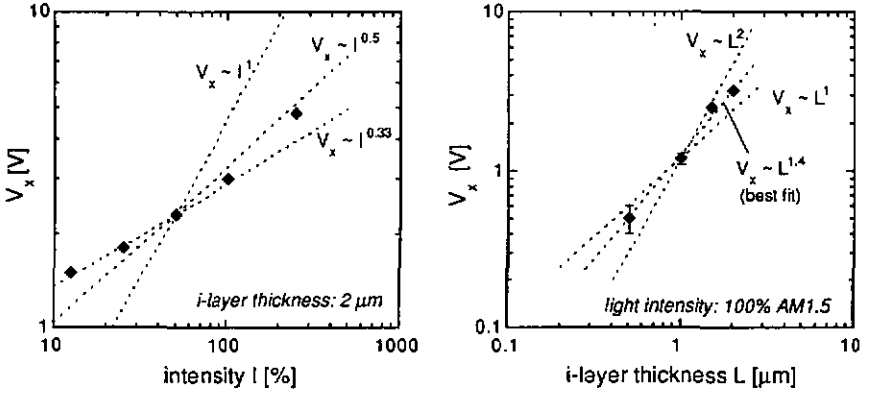

Figure 3.23: Measured intensity dependency (from Figure 3.20), and i-layer thickness dependency (from Figure 3.21) of the threshold voltage for n-side AM1.5 light collection. A built-in potential of 1 V was assumed while determining the internal threshold voltage V_i from the externally measured threshold voltage.

Estimation of the absolute valence-band tail space-charge density

It was intended to assess the possibility that the tail-states, especially the valence-band tail, could influence the collection in standard, thin p-i-n solar cells. An estimation can be done based on the comparison of the approximated densities of charged valence-band states (from Eqn. 3.8), and of the free holes (from Eqn. 3.10). As a result, for a hole density of ~ $4 \cdot 10^{13}$ cm^{-3}, space-charge densities of only 1 - $2 \cdot 10^{15}$ cm^{-3} are found (Table 3.I).

This hole density is at the highest end of what is observed in the modelling of thin p-i-n solar cells (see e.g. Figure 3.14), whereas the corresponding charge-density stays clearly below the level that is needed to significantly distort the electric field distribution in the thin p-i-n solar cells (to be compared with the typical dangling-bond densities). It is thus clearly justified to neglect the valence-band tail (and the conduction-band tail) while considering standard, 0.5 µm thick p-i-n cells under one sun illumination.

Table 3.1: Valence-band tail charge, and hole densities, estimated from n-side collection threshold

i-layer thickness L	threshold voltage V_x (1)	space-charge Q_{VBT} (2)	hole density p (3)
μm	V	cm^{-3}	cm^{-3}
0.5	(0.5 ?)	$(2.6 \cdot 10^{15})$	$(6.2 \cdot 10^{13})$
1.0	1.2	$1.6 \cdot 10^{15}$	$5.2 \cdot 10^{13}$
1.5	2.5	$1.5 \cdot 10^{15}$	$3.7 \cdot 10^{13}$
2.0	3.2	$1.1 \cdot 10^{15}$	$3.9 \cdot 10^{13}$

(1): measured value at 100 % AM1.5, with V_{bi} = 1 V
(2): according to Eqn. 3.8
(3): according to Eqn. 3.10, with μ_p = 1 Vs/cm², and j_p = 10 mA/cm² (~ 1 sun)

3.2.4 Other possible causes of asymmetry

To explain the asymmetric collection in the p-i-n cells after the degradation, other, extrinsic influences on the i-layer space-charge and recombination could be invoked, such as contaminants (oxygen) or dopant traces. But different observations and measurement results exclude this being the case:

First, the p/n collection asymmetry was observed not only in one type of solar cell, but in solar cells deposited in different laboratories, and under different deposition conditions. Also, to cause an asymmetry with a higher p-side over n-side collection through a change in the electric field, a possible i-layer dopant contamination would have to be by phosphorus. With the typical p-i-n deposition sequence, phosphorus contamination is easily controlled (chapter 2.3), and can not be regarded as a widespread and universal problem in p-i-n solar cells.

Also, electric field distortions due to an impurity should have a notable influence already on the annealed state electric field. But the direct measurements of the annealed state electric fields (Figure 3.10), and the annealed state collection of the very sensitive thick p-i-n cells at low intensities (Figure 3.20, at 6.25 % intensity), show no indication of asymmetry.

In one investigation, the degradation of the n-i interface properties was mentioned as a possible cause of the degraded state collection asymmetry [UCH83]. Such a degradation of the n-i interface properties can actually not be excluded. But modelling efforts consistently show [KOP93] that the degradation can definitely not be understood as a change of the i-layer interfaces alone. Also, many different solar cell measurements directly point to the presence of substantial dangling-bond concentrations in the bulk of the i-layer after the degradation (e.g. chapter 3.3). If in the modelling bulk defects are consequently employed, then the space-charges due to these defects always cause electric field peaks close to the interfaces (also at the n-i interface, see Figure 3.14), such that the collection of carriers is screened through these zones of an elevated electric field from the direct influence of the interfaces. As a consequence, the actual properties of the interfaces can be considered to play a minor role in the operation of degraded solar cells, and an increasing n-i interface recombination can not be regarded as causing the p/n-asymmetries seen after degradation.

3.3 Collection of strongly absorbed light in the absence of bias-light, and its link to the bulk i-layer defects

A characteristic suppression of the p-side dark spectral response of strongly absorbed (blue) light after light-soaking has been the object of different research efforts ('blue dip effect' [HOU92], 'ΔSWQE effect' [FOR88]). In some investigations, the effect was interpreted as the manifestation of degradation of the p-i interface [KUS91, KOP92, KOP93], whereas elsewhere it was related to the dangling-bond defects in the bulk of the i-layer [FOR88, HOU92]. It was further proposed to employ the observed reduction of the p-side blue response as a quantitative measure of the dangling-bond defects in the i-layer [FOR88, FOR93].
In this chapter, these different issues will be approached within the framework of the p-i-n solar cell model of section 2.1, and the characterisation concepts of section 2.2. This will allow to distinguish between the p-i interface collection under the particular conditions of illumination with only strongly absorbed light, and the p-i interface collection in the fully illuminated solar cell. Also, a simple quantitative link between the dark blue light collection and the number of i-layer defects will be established, offering a novel way to characterise the material quality of the solar cell i-layer through direct solar cell measurements.

3.3.1 Phenomenology and classification of the effect of the suppressed p-side dark spectral response after degradation

Figure 3.30 shows the p- and n-side spectral response of a degraded p-i-n solar cell, in the dark, and with bias-light. For p-side illumination the collection in the short wavelength range is strongly suppressed if no bias-light is present. In the long wavelength range, as well as over the whole range of the n-side measurement, no further significant deviations of the dark measurements from those with bias-light are found. This particular behaviour of the p-side short wavelength response also contrasts the fact that the degraded state collection is in general found to be independent of the bias-light intensity (see Figures 2.14 and 3.9).

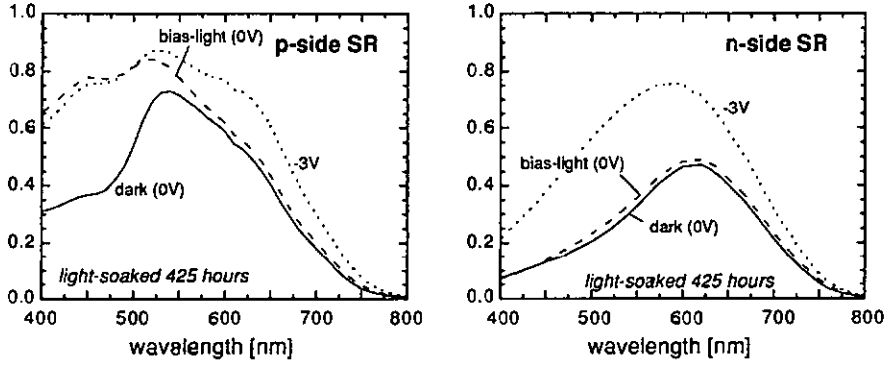

Figure 3.30: p- and n-side spectral response in the dark, and under red bias-light (λ > 610 nm), after 425 hours of light-soaking. The i-layer thickness is 0.5 μm (standard solar cell as in Figure 3.3).

Significance of the dark spectral response

In order to properly classify the behaviour of the p-side response, it is important to recall the link between spectral response and the solar cell current: In section 2.2 it was shown that only the spectral response under bias-light is in a general case related to the solar cell currents. The dark spectral response stands distinctly apart, and has no link to the solar cell currents under illumination. This is because in the absence of a bias-light, at each wavelength the probe-light itself is establishing its own special bias conditions. Furthermore, under these conditions, the spectral response measurement can be intensity-dependent, such that at each wavelength, the corresponding probe-light intensity has to be specified.

The presence of large discrepancies between the dark spectral response, and the spectral response under bias-light indicates that the internal conditions in the solar cell are significantly altered by the change of the illumination from the bias-light to the monochromatic probe-light alone. According to Figure 3.30, in a light-soaked p-i-n solar cell such a change greatly limits the collection in the p-i interface region if only p-side strongly absorbed light is present, as opposed to the situation under standard white or red bias-light, where the p-i interface collection approaches 100 % (Figure 3.6, 3.8, 3.30).

Obviously, these considerations do not exclude the possibility of the monochromatic probe-light collection without bias-light being quite similar to the spectral response with bias-light. This then indicates that the internal solar cell conditions are not strongly modified through the change from the bias-light to the corresponding monochromatic light. Such is the case in the degraded p-i-n solar cells for the whole n-side spectral response, or for the p-side spectral response at wavelengths above 550 nm (Figure 3.30).

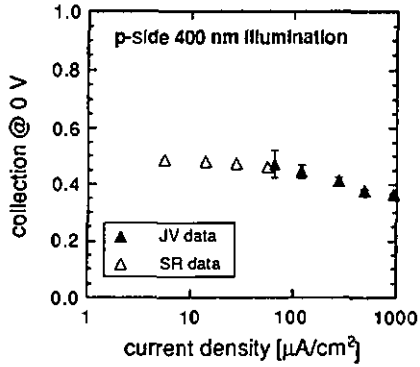

Figure 3.31: Collection at 0 V for p-side 400 nm monochromatic illumination in the dark, as a function of the saturated current density (~ light intensity), in a light-soaked standard p-i-n solar cell. The solar cell and degradation status are as in Figure 3.30.

Figure 3.31 shows the collection for p-side 400 nm light at 0 V, in the absence of bias-light, over a large range of intensities. For intensities in the range of typical spectral response probe-beams, the collection is about constant. For higher intensities, a small further decrease of the collection is noted. Overall, the collection is relatively intensity independent. This 'linear' behaviour indicates that the effect of the suppressed collection is caused by the dangling-bond defects, or at least it discards an involvement of the tail-states (see section 3.2.3).

Violation of the superposition principle

The effect of the suppressed p-side collection in the absence of bias-light explains also a class of seeming violations of the superposition principle in the JV-curve behaviour of light-soaked solar cells: Figure 3.32 shows the p- and n-side collection of a degraded p-i-n solar cell under the complete AM1.5 spectrum, and separately under only the long wavelength part, and under only the short-wavelength part of the same spectrum.

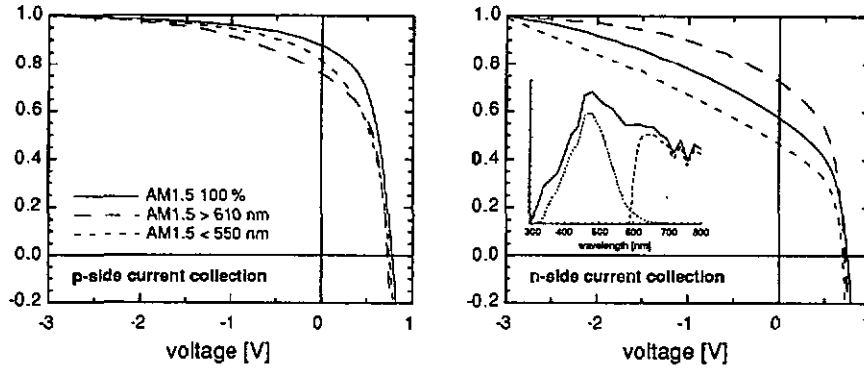

Figure 3.32: p- and n-side current collection of a light-soaked solar cell under the short wavelength part, the long wavelength part, and the total of the AM1.5 spectrum (same cell and degradation status as in Figure 3.30).

As a result, for p-side illumination, the collection of both the fractions of the spectrum alone is lower than the collection of the full solar spectrum, such that the collection of the total spectrum can not be explained as the sum of the collection of the two fractions. This seeming violation of the superposition principle is explained by the 'self-suppression' of the strongly absorbed part of the spectrum: if only the strongly absorbed, short wavelength part of the spectrum is present, the collection is reduced similarly to the p-side blue spectral response. If on the other hand both parts of the spectrum are present, the collection of the strongly absorbed short wavelength part of the spectrum becomes close to 100 %, as shown by the collection analysis under bias-light (Figures 3.30/3.7), explaining thus the overall higher collection of the total spectrum.
For illumination from the n-side there is no 'self-suppression' of blue light, and the 'expected' behaviour of the collection is observed, with the collection of the total spectrum lying between the collection of its short and long wavelength fractions.

3.3.2 Interface or bulk effect ?

The suppression of the p-side short wavelength response (without bias-light) after light-soaking has been interpreted as a strong indication that the degradation of the p-i-n cells comprises a major degradation of the p-i interface region [KUS91, KOP93]. In particularly it was argued, based on numerical simulations, that the suppression of the dark p-side spectral response could not be modelled without assuming a significant increase of the interface defects after degradation [KOP93]. The modelling of other measured effects of the degradation (e.g. the strong thickness dependence of the efficiency) however forces these authors to assume also an increase of the defects in the bulk of the i-layer. While it is difficult to actually disprove these simulation results, it

is important to note that the suppressed p-side response can be modelled by assuming an increase of the bulk i-layer defects alone [HOU92, SMO92]. In these investigations it was shown that the decrease of the p-side response without bias-light can be explained by a reduced electric field at the p-i interface induced by the i-layer defect charge, rather than by an increase of the local p-i interface defects (see Figure 3.33, and below). Also, these simulation results accurately reproduce the high response under bias-light, which appears unlikely in the above cited case where the suppressed dark response is modelled by an actual deterioration of the interface region itself [KOP93].

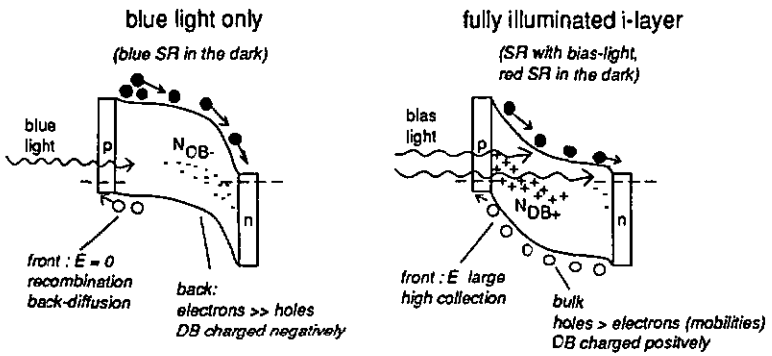

Figure 3.33: Schematic band-diagram in a degraded p-i-n solar cell. Left: under p-side blue light illumination, without bias-light (suppression of the p-side blue spectral response); Right: under bias-light illumination (high collection in the p-i interface region)

Figure 3.34 shows the numerically simulated i-layer carrier concentrations, dangling-bond charge, electric field, and potential distributions for different illuminations. A constant i-layer dangling-bond density of $2 \cdot 10^{16}$ cm^{-3} is used, and the applied external voltage is 0 V. The illuminations are p-side 400 nm light, representative of the p-side short wavelength collection in the dark, homogeneously absorbed light representative of the bias-light of the spectral response, and n-side 400 nm light, representative of the n-side dark short wavelength collection.

As a result, the i-layer space-charge, and the potential distribution in the i-layer, are found to be completely reversed by the change from homogeneously absorbed light to light absorbed only at the p-i interface. In contrast to the dominating positive space-charge under bias-light illumination (as discussed in section 3.2.3), under the illumination of only the p-i interface region, the potential distribution is dominated by the negative space-charge in the back of the i-layer. This negative space-charge arises from the sole presence of electrons in the back of the i-layer. In the front of the i-layer, a zone of shallow electric field is established, favouring the accumulation and subsequent recombination of the carriers generated there. This explains the strong decrease of the collection under this illumination condition.

For the case of n-i region illumination, the charge distribution is not much altered with respect to the homogenous illumination (bias-light) case. This is because the positive charge also dominates under the homogenous illumination. An additional reduction of the electron concentration in the bulk, due to an illumination with only n-side blue light, therefore causes only a small change in the overall potential distribution. This explains why no further suppression of the already low n-side blue response is observed when the bias-light is removed (Figure 3.30, right).

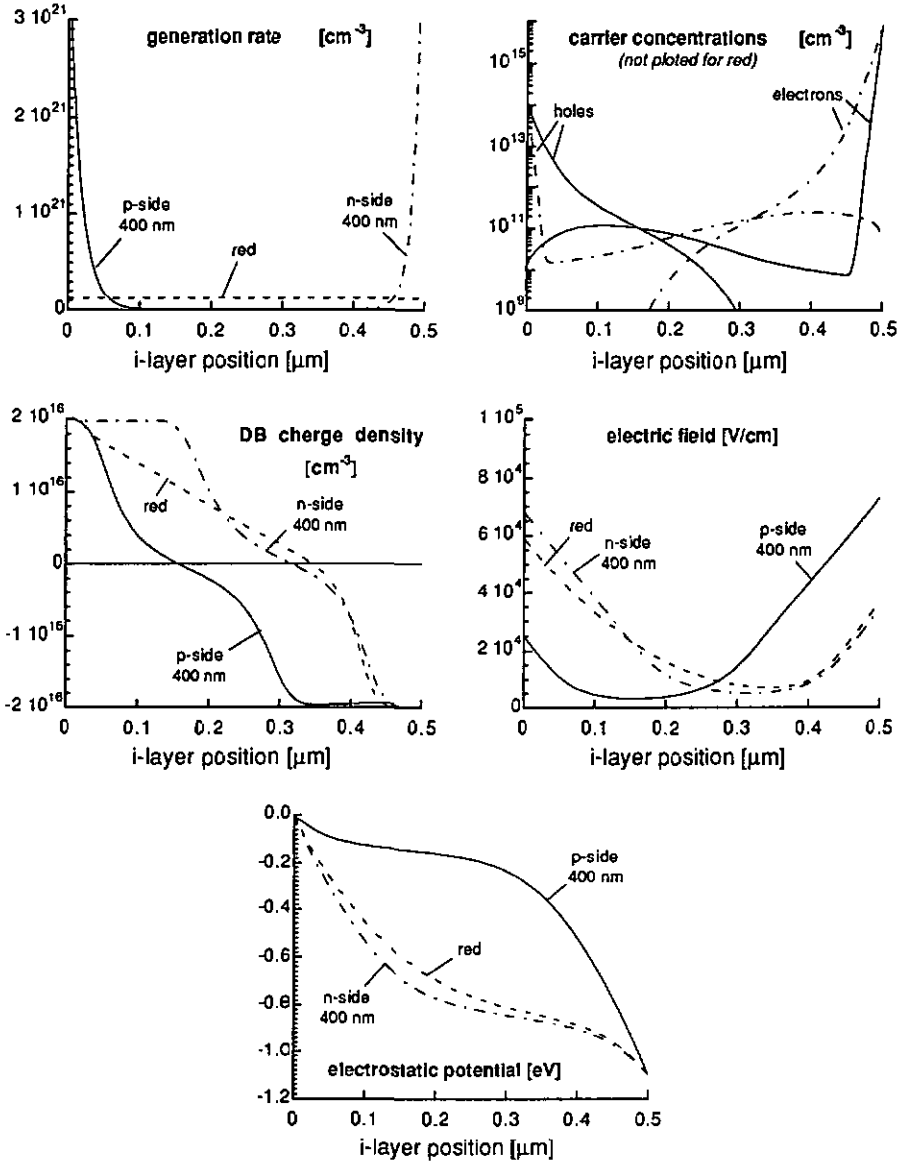

Figure 3.34: Numerically simulated generation rate, carrier densities, dangling-bond space-charge, electric field, and electrostatic potential as a function of the i-layer position, for p-side 400 nm, homogeneously absorbed (red), and n-side 400 nm illumination. The generation current is constant at 1 mA/cm^2 for all illuminations. The i-layer dangling-bond density is 2·10^{16}cm^{-3}, the other parameters are the standard parameters of Table 2.1.

In summary it can be stated that due to the asymmetry in the carrier mobilities, over wide ranges of monochromatic illumination the degraded state space-charge is dominated by the positive charge.

Only under illumination of the p-i interface region alone, the space-charge distribution is reversed and results in the suppression of the p-side collection by a dominating negative space-charge. In regard to the relative roles of interface and bulk defects, it is thus demonstrated that the bulk defects, even if they are located far from the p-i interface region, do strongly affect the collection in the p-i region by their influence on the overall potential distribution in the i-layer. The fact that the suppression of the collection from the p-i region is extremely sensitive to the presence of bias-light in the remote bulk of the i-layer does rule out an explanation based on interface degradation alone. Obviously, once the p-i interface electric field is reduced due to the negatively charged bulk defects, the actual amplitude of the (suppressed) blue light collection will become more sensitive to the p-i interface properties (electron back-diffusion to the interface). But this sensitivity is only given under the blue light illumination, whereas in the operating solar cell (i.e. under bias-light absorbed in the whole i-layer), the high p-i interface electric field will make the solar cell collection rather independent of the p-i interface properties.

3.3.3 The threshold voltage and its link to the i-layer defect density

The magnitude of the dark collection of p-side short wavelength light at 0 V was proposed as a sensitive monitor of the dangling-bond concentration present in the i-layer of a p-i-n solar cell [FOR93]. The steady decrease of this quantity with increasing degradation time [FOR88, FOR93], and its adjustable sensitivity due to its pronounced i-layer thickness dependency [FOR88, FOR93], were argued to make the p-side blue light collection a sensitive measure of the defect density. It was shown that indeed the degraded state performance of solar cells with differently prepared i-layers scaled with the amplitude of the dark collection of p-side blue light at 0 V [FOR93]. But the pure measurement of the suppressed collection amplitude at 0 V lacks a direct and uncomplicated link to the underlying number of defects.

The threshold voltage

A concise link between the actual defect density, and the measured collection can be established by considering the detailed voltage dependence of the collection. Figure 3.35 shows the voltage dependent collection of p-side 400 nm light in the dark. From the suppressed values of the

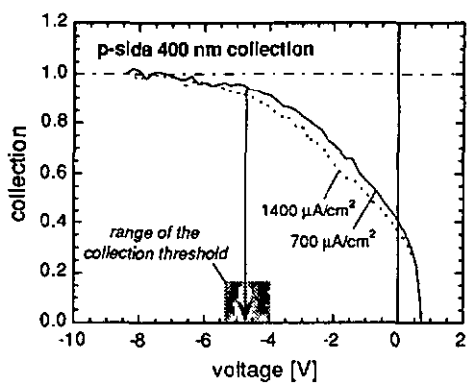

Figure 3.35: Voltage dependent collection for p-side 400 nm illumination in a degraded standard solar cell with a 0.5 μm thick i-layer (solar cell, and degradation status are the same as in Figure 3.30)

collection around 0 V, the collection is found to rise towards unity in a very specific shape. Contrasting an exponential voltage dependence ('Hecht'-curve), a threshold behaviour is discernible. For increasing voltage, this threshold marks the transition from a high, nearly saturated collection to a regime of rapidly increasing losses. The threshold bebaviour, analogous to the collection at 0 V (Figure 3.31), is not depending on the illumination intensity.
As seen in other sections of this work, threshold like features in the voltage dependent collection call for an explanation in terms of space-charge and electric field extension in the i-layer (sections 3.2.3 and 4.2). Figure 3.36, left, shows the schematic band-diagram and dangling-bond space-charge at a voltage below the threshold voltage.

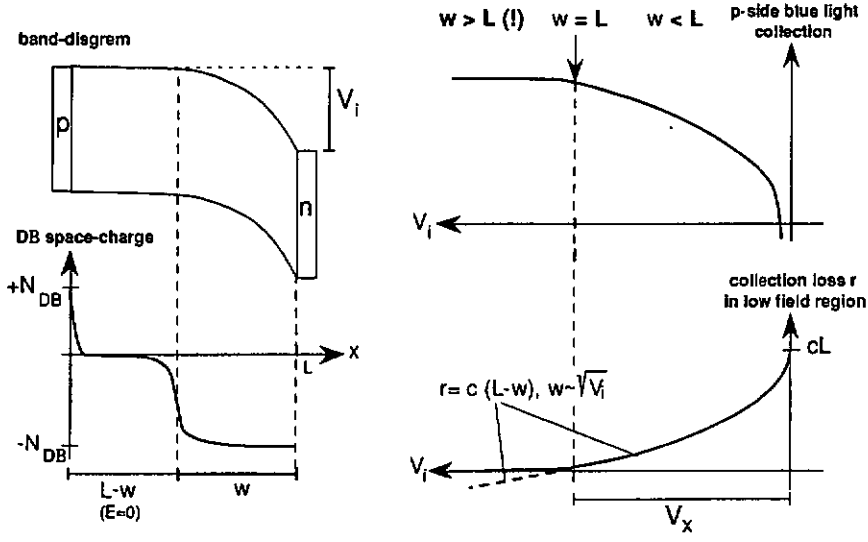

Figure 3.36: Schematic model of the threshold voltage observed in the collection of p-side strongly absorbed light in light-soaked p-i-n solar cells (see text).

The i-layer is divided in a section with a cancelled electric field and with no space-charge ($f^0 = 1$) at the p-side of the i-layer, and a section of negative defect charging ($f^- = 1$) over which the full applied voltage is dropped. The extension of the n-side zone of negative defect charging w is directly linked to the total voltage applied to the i-layer V_i as given by expression of the single-sided abrupt junction [SZE86]:

$$w = \sqrt{\frac{2 \cdot \varepsilon_r \cdot \varepsilon_o \cdot V_i}{q \cdot N_{DB}}} \qquad (3.10)$$

The applied voltage V_i is the sum of the external voltage and the built-in potential (V_{bi}). For increasing applied voltage V_i, the extension of the negative space-charge is progressing towards the p-side, and the zone without electric field is shrinking. Eventually the whole i-layer is depleted, i.e. w = L, at the threshold voltage V_x. Employing Eqn. 3.10, the threshold voltage V_x directly yields the defect density in the i-layer of the solar cell:

$$N_{DB} = \frac{2 \cdot \varepsilon_r \cdot \varepsilon_0 \cdot V_x}{q \cdot L^2} \tag{3.11}$$

Beyond the threshold voltage V_x, the electric field homogeneously increases in the whole i-layer as a function of the applied voltage.

Issues in modelling the voltage dependent collection

It might be asked as to whether the above idealised model of a well confined region of negative space-charge is realistic, or whether the transition between negative and neutral defect occupation is smeared out over a wide region of the i-layer. Obviously the slope of the transition depends on the ratio of cross sections of charged and neutral dangling-bonds, with small ratios leading to a faster transition. For a moderate cross section ratio (C=10), the numerical modelling shows still a well defined space-charge width w (Figures 3.34/3.37). In fact the existence of the threshold behaviour itself strongly indicates that the extension of the negative space-charge region is sharply defined, because otherwise the collection curve could only change in a gradual way.

One might further expect a step-like decrease of the collection at the threshold voltage, as it is seen for space-charges due to doping (section 4.2), rather than the experimental 'linear' slope seen in the experimental data. But in the present case, similar to the effects observed due to the valence-band tail charge (section 3.2.3), the collection can not drop step-like because there is a balance between electrons lost in the reduced field zone, and electrons escaping to the back and thus sustaining the space-charge. In the numerical simulation, the electric field in the p-i region is, through this balance, not totally zeroed below the threshold voltage, but a residual electric field is established, originating from the combined effects of recombination, hole back-diffusion, and a zone of only partial defect charging (Figure 3.37). This residual electric field is only slowly reduced beneath the threshold voltage, explaining the rather gradual than step-wise decrease of the p-side collection.

In a previous investigation [FOR88], the collection as a function of the applied voltage was quantitatively modelled by assuming the collection losses r proportional to the width of the low electric field region L-w (see Figure 3.36). Such a mechanism could e.g. represent the recombina-

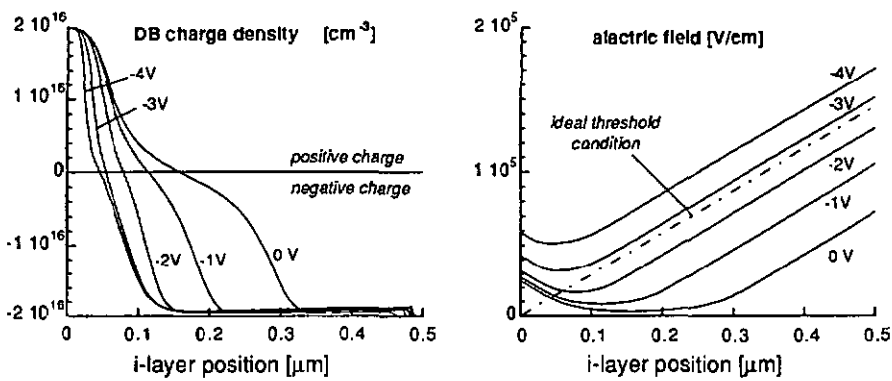

Figure 3.37: Numerically modelled space-charge and electric field as a function of the external voltage for p-side 400 nm illumination. The modelling parameters are as used in Figure 3.33. The voltages indicated are external voltages. For the given defect density of $2 \cdot 10^{16} cm^{-3}$, Eqn. 3.10 yields an internal threshold voltage of 3.8 V, corresponding to -2.8 V external voltage (dotted line: idealised electric field for the threshold condition).

tion probability of electrons diffusing through the low electric field region of neutrally charged defects towards the negative space-charge region.

$$r = c\cdot(L-w) = c\cdot(L-\sqrt{2\cdot\varepsilon_r\cdot\varepsilon_o/q\cdot N_{DB}}\cdot\sqrt{V_i}) \quad \text{(for } w < L\text{)} \qquad (3.12)$$

This model predicts a collection proportional to the square-root of the applied voltage (see Figure 3.36, right). This model was shown to agree with the experimental collection curve at low applied voltages [FOR88]. In principle, N_{DB} and the loss proportionality factor c could thus be extracted from the experimental curves by a fitting procedure.
It is however important to note that the square-root proportionality of the collection loss of Eqn. 3.12 is only valid for $w > L$, i.e. for $V_i < V_x$. For $V_i > V_x$ the collection loss must obviously be zero. The onset of the square-root loss mechanism at V_x in fact again defines the collection threshold, with a collection of near 100 % starting to decrease with a "linear slope" (see Figure 3.36, right), as seen in the experimental data. As compared to fitting the shape of the low-voltage range of the collection curve, the determination of the defect density N_{DB} from the threshold voltage (according to Eqn. 3.11) has the advantage of being more direct, and of not requiring any assumptions regarding the detailed loss mechanisms.

Wavelength dependency of the threshold voltage

The defect densities resulting from the evaluation of Eqn. 3.11 are very sensitive to the i-layer thickness L (square dependence). Or in other words, it is crucial that at the threshold voltage, all i-layer dangling-bonds are fully negatively charged up to the p-i interface. Otherwise, the actual dangling-bond density is underestimated.
An important parameter to fulfil this requirement is the penetration depth of the monochromatic probe light: Clearly, the probe light must be absorbed as close as possible to the p-i interface. Only then are electrons the majority carrier up to the p/i interface. This is illustrated in Figure 3.38, showing a very fast reduction of the threshold voltage (that would lead to an underestimation of the evaluated defect density) with increasing penetration depth of the monochromatic light.

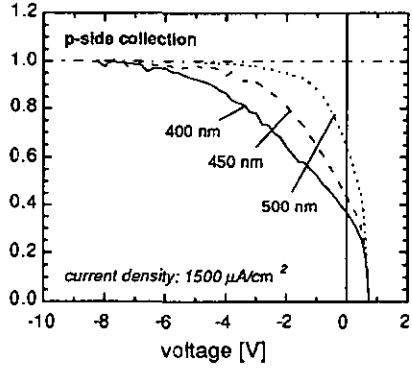

Figure 3.38: Collection of p-side monochromatic light as a function of the wavelength in a degraded p-i-n solar cell. The solar cell and degradation status are the same as in Figure 3.30.

Employing Eqn. 3.11, and assuming a built-in potential of 1 V, the collection threshold for p-side 400 nm light of the standard p-i-n solar cell (Figure 3.35) yields a density of dangling-bonds in the range of $2.5 - 3.5 \cdot 10^{16}$ cm^{-3}.

Defect densities in differently prepared i-layers

Figure 3.39 compares the degradation behaviour of two p-i-n solar cells with different types of i-layers. In one cell the standard deposition temperature is used, whereas for the other cell, the i-layer deposition temperature is lowered. Both cells have the same i-layer thickness of 0.7 µm.
In the annealed state, the performance and JV-curve of both cells are similar. But after a given time of light-soaking (120 hours), the cell with the low temperature i-layer clearly exhibits inferior performance compared to that of the standard cell (Figure 3.39, right).
In the degraded state, the two cells show a distinct difference in the p-side blue light collection (Figure 3.39, right). The threshold voltage is clearly higher for the cell with the low temperature i-layer. The stronger performance degradation of the low temperature cell seems to indeed be caused by a higher number of i-layer defects.
The evaluation with Eqn. 3.11 yields defect densities of $1.2 \cdot 10^{16}$ cm^{-3} for the standard i-layer, and of $2.4 \cdot 10^{16}$ cm^{-3} for the low temperature i-layer, again assuming a built-in potential of 1 V (the lower absolute values of the defect densities as compared to the solar cell of Figure 3.35 are due to a shorter light-soaking time (120 hours); also the defect densities are underestimated because 450 nm light was used instead of 400 nm light).

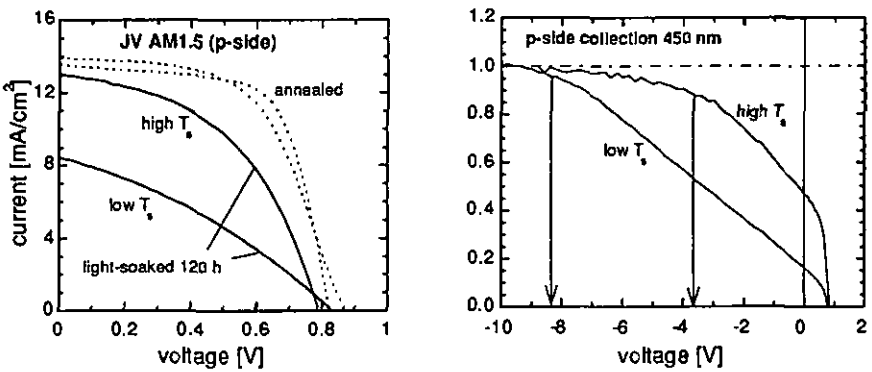

Figure 3.39: Comparison of solar cells with different i-layer deposition temperatures (high T_S: 220°C, low T_S: 150°C). The i-layer thickness is 0.7 µm. The other fabrication parameters correspond to the standard solar cell as described in Figure 3.30. The light-soaking was 120 hours at one sun, Na-spectrum. Left: JV p-side AM1.5/100 mW/cm^2; Right: collection of p-side 450 nm light in the dark after light-soaking, monochromatic intensity 1500 µA/cm^2.

The n-side collection threshold voltage, and its implications for the defect distribution

Up to here the focus was on the effect of the negatively charged defects on the collection of p-side strongly absorbed light. The n-side collection of strongly absorbed light is expected to be subject to the same mechanisms, but caused by positive defect charging. The only difference is that for the case of the n-side collection the positive space-charge is dominating already under bias-light

illumination, due to the lower hole mobility (as discussed above). Figure 3.40 shows that indeed also for n-side illumination with strongly absorbed light a collection threshold is found. Interestingly, the threshold voltage measured from the n-side is about twice as high as the one under p-side illumination.

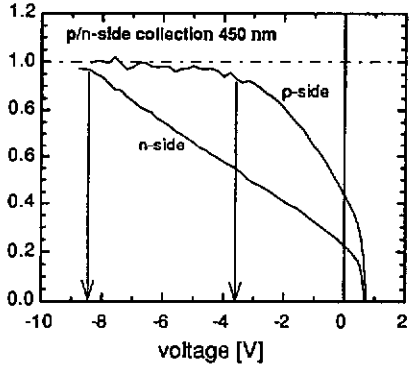

Figure 3.40: p-side, and n-side collection of 450 nm light in the dark, with a monochromatic intensity of 1500 μA/cm², after light-soaking. The solar cell, and degradation status are the same as in Figure 3.30.

Two models can explain a difference between the p- and n-side threshold voltage:

- The presence of constant densities of non-amphoteric defects in the solar cell i-layer, as e.g. used in [LEE91, KOP92], with the density of donor-like defects (positively charging) being higher than the density of acceptor-like defects (negatively charging).
- The presence of a non-constant defect density of (amphoteric) defects in the i-layer

In the following only the second model shall be further considered: For a non-constant defect density, Eqn. 3.11 is obviously no longer valid. But even with a non-homogenous defect density a threshold behaviour is still expected. With a non-homogenous charge profile, the charge contributions from the different locations in the i-layer have changing efficiencies in affecting the magnitude of the threshold voltage. It can easily be shown that charges close to the illuminated interface cause a much bigger increase of the threshold voltage than the same charges located at the remote interface. The higher n-side threshold shown in Figure 3.40 thus indicates that after light-soaking the density of defects increases from the p-side towards the n-side of the i-layer.

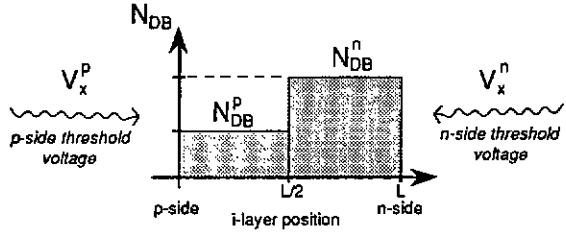

Figure 3.41: Schematic two-zone dangling-bond defect density model. The constant defect densities are assumed in the front and in the back half of the i-layer.

Obviously, many different shapes of the defect distribution can explain the set of two threshold voltages. With two measured threshold values, two defect distribution parameters can be evaluated. Figure 3.41 shows a two-zone dangling-bond distribution model, with two unknown defect densities in the front and the back half of the i-layer.
The defect densities in the two zones of the i-layer can be shown to result from the two threshold voltages as follows

$$N_{DB}^{p} = \frac{\varepsilon_r \cdot \varepsilon_0}{q \cdot L^2} \cdot (3\,V_x^p - V_x^n) \tag{3.13}$$

$$N_{DB}^{n} = \frac{\varepsilon_r \cdot \varepsilon_0}{q \cdot L^2} \cdot (3\,V_x^n - V_x^p) \tag{3.14}$$

Physical solutions are only found for a limited difference of the two threshold voltages

$$\frac{V_x^n}{V_x^p} = \tfrac{1}{3} \ldots 3 \tag{3.15}$$

Employing the threshold data of Figure 3.40, Eqns. 3.13 and 3.14 yield $N_{DB}{}^{p} \approx 1 \cdot 10^{16}$ cm^{-3}, and $N_{DB}{}^{n} \approx 5 \cdot 10^{16}$ cm^{-3} (the threshold voltages of Figure 3.40 are for 450 nm monochromatic light; the actual defect densities are thus expected to be somewhat underestimated (see Figure 3.38)).

General remark on the obsolute defect densities found in degroded films and solar cells

The method of the collection threshold implies the presence of defect densities in the range of $1 - 5 \cdot 10^{16}$ cm^{-3} in the i-layer of light-soaked p-i-n solar cells. On the other hand, in the literature commonly defect densities of 10^{17} cm^{-3} or higher are referred to for light-soaked a-Si:H films [ISO92, HAT92]. This discrepancy leads to two possibilities:

(1): The degraded state defect densities cited for films are most often measured after high intensity light-soaking, whereas in the present investigation the solar cells were degraded at one sun illumination levels. Further, the saturated defect density levels are generally accepted to be dependent on the light intensities [HAT92, FUJ93]. The above discrepancy could thus represent a true difference of the defect densities in the two measurements, caused by the different illumination intensities employed for the degradation.
The magnitude of the difference between the defect density obtained after high intensity light-soaking and the defect density obtained after one sun light-soaking is estimated in Figure 3.42. The estimation is based on measured solar cell efficiencies after low and high intensity light-soaking [FUJ93]. If these efficiencies are compared to a numerically modelled correspondence between solar cell efficiency and defect density, it is seen that at least a factor of 3 in the defect density must be assumed to explain the difference in the measured efficiencies (remark: the slope in the modelled correspondence between the efficiency and the logarithm of the defect density of Figure 3.42 compares well with slopes found elsewhere [FUJ93]).

(2): The collection threshold method measures only defects that are actually available for charging under the either strong electron or strong hole majority conditions which prevail in the solar cells under strongly absorbed illuminations. The film measurements on the other hand are all based on,

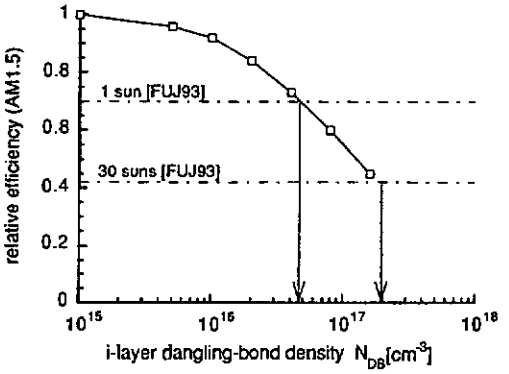

Figure 3.42: Numerically modelled solar cell efficiencies as a function of the i-layer dangling-bond density, normalised to $N_{DB} = 10^{15}$ cm^{-3} (symbols), compared to the measured relative degradation of solar cell efficiencies under 1 sun and under 30 sun illumination [FUJ93] (broken lines). The modelling parameters are of Table 2.1, for p-side AM1.5 illumination, with the tail-states not modelled.

or calibrated by, electron spin resonance (ESR), a measurement that explicitly measures only neutral defects. It could now be imagined that only a part of the defects as measured by ESR have the ability to change their charge state. E.g. it has been suggested that only 30 % of the defects as measured by ESR can change their charge state, and contribute to electric field distortions in p-i-n devices [QUR89]. The question however arises as to the nature of the remaining, permanently neutral defects, and to their relevance to the solar cell operation. Clearly, defects at mid-gap that are acting as recombination centres must also have the ability to change their charge state (at least temporarily during the recombination process). In this view, the permanently neutral defects, participating neither in the recombination nor in the space-charge, would thus not be relevant to the solar cells.

Obviously, these explanations are for the moment just speculations; further detailed comparisons between defect measurements in films and in solar cells will be needed to clarify this interesting issue.

3.4 Conclusions on the degradation of p-i-n cells without i-layer doping

The effects seen in the degradation of p-i-n solar cells of an i-layer thickness range of 0.5 µm are consistent with an increase of defects in the whole i-layer. Specific degradation of the doped layer interfaces can not be excluded, but clearly interface degradation does not determine the performance of the degraded solar cells.

The measurements show that after the degradation, the p-i-n solar cells exhibit a strongly asymmetric i-layer collection probability. This asymmetry, featuring a high collection at the p-i interface, and a decreasing collection towards the n-side of the i-layer, was found to be universally present in degraded solar cells, independent of the direction of the light-soaking illumination (p-/n-side), and independent of the bias conditions during the measurement (illumination/voltage).

The solar cell modelling demonstrates that this collection asymmetry is consistent with an overall increased defect density, combined with an electron mobility higher than the hole mobility. A difference in the mobility is shown to intrinsically cause a dominating positive defect space-charge, leading to a high electric field at the p-i interface, and lower electric fields towards the n-side of the i-layer. The prediction of an asymmetric electric field distribution of the solar cell model is supported by electric field measurements in degraded p-i-n cells. Also, the detailed measured collection behaviours are in agreement with such an asymmetric electric field distribution.

The suppression of the p-side spectral response in the dark in degraded p-i-n solar cells can be understood by the same bulk defect model, whereas interface degradation model fails. The voltage dependent analysis of the collection of strongly absorbed light leads to a novel method for the quantitative measurement of the i-layer defect concentration directly in the p-i-n solar cell. Defect densities in the range of a few times 10^{16} cm^{-3} are found in p-i-n solar cells degraded for several hundred hours. Also, there are indications that in the degraded solar cell, the concentration of defects in the i-layer is not constant, but is higher at the n-side than at the p-side.

The analysis of the influence of the band-tail states on the p-i-n cells shows evidence of the valence-band tail only. Based on voltage dependent solar cell collection measurements, the charge densities trapped in the valance-band tail were estimated by a simple model. It is clearly shown that the detected charge densities are too small to significantly influence the collection in 0.5 µm thick p-i-n solar cells. Yet, it is demonstrated that the analysis of thick p-i-n cells, and at high light intensities, is a useful means to characterise the properties of the valence-band tail.

4 Graded low-level i-layer doping in amorphous silicon p-i-n solar cells

"A solution ?"

4.1 Introduction

Compensation of the dangling-bond space-charge by graded low-level i-layer doping

In this chapter low-level doping of the i-layer is investigated as a means to improve the degraded state performance of a-Si:H p-i-n solar cells. The following concepts motivate this investigation:

(1): After the degradation, dangling-bond defects are present in the i-layer of the p-i-n cells. These defects charge as a function of the local majority carrier polarity, and distort the electric field distribution in the i-layer. This distortion increases the overall collection losses, because carriers accumulate in the low-field regions where they are subject to an enhanced recombination probability (as discussed in chapter 3).

(2): For any given density and distribution of the dangling-bonds, an i-layer doping scheme can be found to compensate the dangling-bond space-charge, and to impose any desired distribution of the electric field within the i-layer of the p-i-n cell. It is important to note that only the use of graded, non-constant doping of both polarities enables this generalised freedom of design (this concept arises from the fact that amorphous silicon can be doped systematically over the whole range from strongly p-type to strongly n-type, and with dopant concentrations spatially controllable to the angstrom level).

Based on these concepts, an i-layer doping profile can be developed to tailor the electric field in the solar cell for optimised collection in the degraded state. Figure 4.1 illustrates the general idea of the intended compensation of the dangling-bond charge: Without graded doping (Figure 4.1, left), the i-layer electric field is uniform in the initial state, and distorted by the dangling-bond space-charge after degradation. In the p-i-n solar cell with the optimised graded doping (Figure 4.1, right), the electric field is distorted initially, and reaches its optimal distribution only after the creation of the light-induced dangling-bonds.

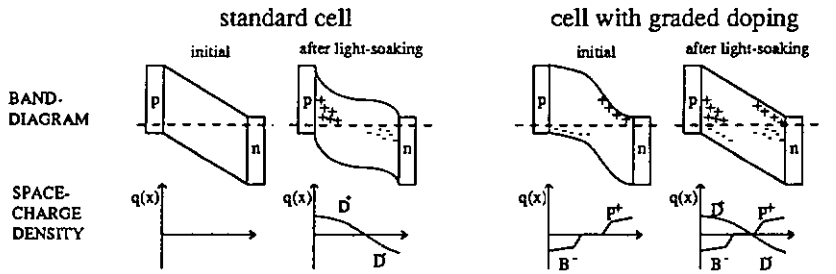

Figure 4.1: Generalised idea of the i-layer electric field profiling in a-Si:H p-i-n solar cells for optimised degraded state performance.

Previous investigations of low-level i-layer doping

Throughout the history of amorphous silicon solar cells, intentional doping of the i-layer of p-i-n solar cells has been applied and discussed repeatedly. The invention of the amorphous silicon solar cell was due to the p-i-n structure, i.e. the use of an undoped light-absorbing i-layer, with the junction induced by only narrow doped layers [CAR76]. Simultaneous trials with both p- and n-doped absorbing layers proved less successful. This was explained with a reduced diffusion length of the then used (highly) doped a-Si:H materials [CAR76]. Later, depending on the solar cell structure (n-i-p or p-i-n) or deposition technique, i-layer doping with boron or phosphorus at concentrations in the ppm range enabled (initial) efficiency gains over cells employing no i-layer doping [KON82, HAR83, SIC83, CAT86, KAU88]. In most cases, the improvement was explained with the compensation of electric field distortions due to unintended, fabrication related contaminations of the i-layer [KON82, CAT86, KAU88]. Elsewhere, the effect of the low-level doping was explained in terms of a detailed improvement in the i-layer transport properties (e.g. a more 'intrinsic' material [SIC83], improved $\mu\tau$ products [HAR83], etc.). But as deposition technology improved, the contamination problems became better controlled, and the best initial efficiencies were once more achieved without i-layer doping.

Some years ago, low-level i-layer doping has been studied in conjunction with the solar cell degradation in several investigations [MOE85, KUS85, CAT85, GOR86, KUW87, GOR88]. None of these investigations were however able to demonstrate an actual improvement of the solar cell efficiency after degradation. In some cases, both boron and phosphorus doping were shown to lead to a reduced relative degradation of the solar cells [CAT85, MOE85, KUS85]. But never the resulting efficiencies after degradation were actually improved over those of cells without low-level doping. For boron doping different studies even showed increasing efficiencies during degradation [KUS85, GOR86, KUW87], a finding which in the view of the present work points directly towards the compensation between dopant and dangling-bond charge.

The overall lack of success of the cited studies in producing improved solar cell performances might be explained by the fact that those studies were not actually focused on the dangling-bond charge and on an actual optimisation of the electric field distribution. Rather, many different doping schemes (often constant doping of the whole i-layer) were applied randomly to check for a reduced degradation. Only in one patent the idea of compensating the dangling-bond space-charge by i-layer doping has been formulated [SCH88], but was apparently never implemented experimentally. It is also important to note that the implications of stacked cells, and the possibility to individually optimise their component cells, were not considered at that time, an idea that will be fundamental in the present work (see section 4.3).

Will doping induced defects compromise the gains due to the space-charge compensation ?

Besides modifying the electric field distribution within the solar cell i-layer, the addition of dopants also alters the local material properties in these doped zones. Firstly, the presence of dopant atoms creates additional dopant-states in the amorphous silicon material. Also, with rising dopant concentration, the defect density at mid-gap and thus the recombination are typically found to increase [STR83, STR91]. The difficulty of employing i-layer doping to improve the performance of a-Si:H solar cells is that the desired and the detrimental effects of the doping can not be separated. Obviously a doping related increase of the recombination prohibits the use of the i-layer

doping as soon as the additional recombination losses are larger than the gains due to the improved electric field.

The experimental evidence of strongly increased defect densities in doped materials occurs however only in the range of high dopant concentrations. In the range of the very low-level doping concentrations needed to manipulate the electric field within the i-layer of a p-i-n cell (around 1 ppm, see section 4.2), the measured defect densities seem in turn to be well within the range of undoped materials (before degradation) [SAU93].

It must also be considered that the defect densities determined by film measurements are subject to various interpretation problems [e.g. SAU93]. One thus hesitates to employ those film measurement results for a detailed evaluation of the feasibility of the above low-level doping concept.

In the present work, the issue will be indirectly addressed by the investigation of the low-level doped solar cells themselves. These experiments will show that strong recombination losses do not occur as long as the cited low doping levels are used. This observation is ultimately corroborated by the demonstration of an actually improved solar cell performance (see section 4.3).

4.2 Graded low-level i-layer doping in p-i-n cells

In this section, the basic effects of low-level i-layer doping on the p-i-n solar cell behaviour are demonstrated and discussed. The doping concentrations refer to the ratio of either diborane (B_2H_6, p-type doping) or phosphine (PH_3, n-type doping) over silane (SiH_4) in the i-layer deposition feed gas. Details on the deposition technology of low-level doped materials are given in section 2.3.4.

4.2.1 Boron doping

Boron doping in a-Si:H creates acceptor states, i.e. states that are negatively charged when ionised. If applied in the i-layer of a p-i-n cell, the negative space-charge leads to a reduced electric field between the p-layer and the doped zone, and to an increased electric field between the doped zone and the n-layer (Figure 4.2). The electric field is thus displaced within the i-layer, while total potential drop between the p-layer and the n-layer remains constant. Depending on the extension and magnitudes of the doping in the i-layer, the resulting quantitative shifts of the electrostatic potential are different, but the general trend of a displacement of the electric field towards the n-side of the i-layer will always accompany boron doping in the i-layer.

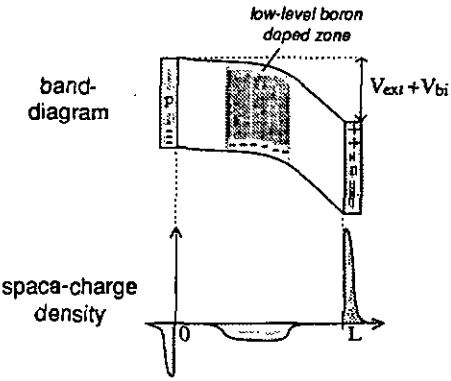

Figure 4.2: Schematic influence of graded i-layer doping with boron (acceptors) on the band-diagram and space-charge density in a p-i-n solar cell.

The described effect of the boron doping on the electric field in the p-i-n cells causes a general decrease of the collection on the p-side of the i-layer. Because for any general distribution of the boron in the i-layer it is always the electric field close to the p-i interface that is reduced most, boron doping is typically associated with a reduction of the p-side short wavelength spectral response (section 2.3, [KUS85, ONI91]). But depending on the location of the doped zones, the

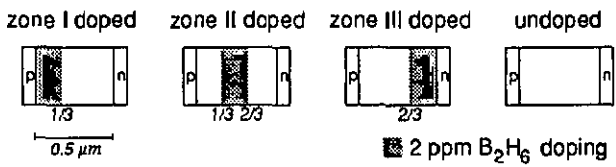

Figure 4.3: Schematic boron doping profiles of the p-i-n solar cells analysed in section 4.2.1. With exception of the doping in the i-layer, the solar cells correspond to the standard solar cell of Figure 3.3.

collection is reduced not only at the p-side, but also in the depth of the i-layer. The link between doping location, electric field and carrier collection will in the following be demonstrated based on the set of graded boron doped solar cells shown in Figure 4.3.

Basic measurements

Figure 4.4 shows the electric fields at zero applied external voltage, as measured by µs current transients (section 2.2.4) from both the p- and the n-side. As electric fields which increase in the direction away from the measurement side can not be measured by this method, the p-side measurements only indicate that the boron doped cells have a reduced field at the p-side as compared to the undoped cell. The n-side measurements on the other hand yield detailed information on the electric field distribution.

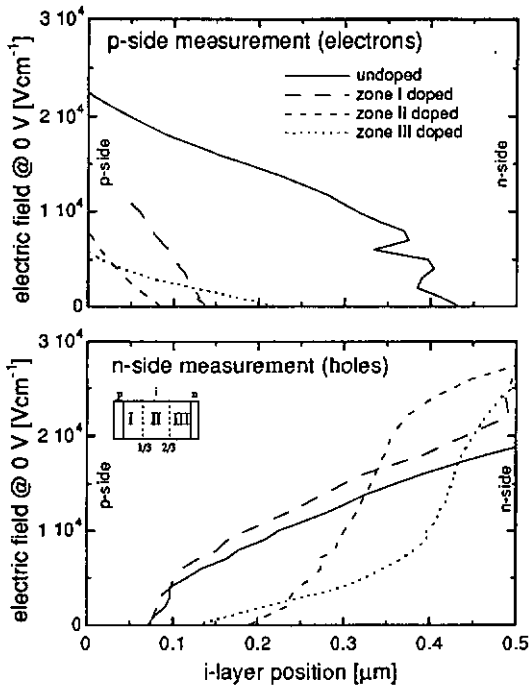

Figure 4.4: p- and n-side electric field profiles in graded boron doped p-i-n solar cells as measured by µs charge transients (chapter 2.2.4). Doping profiles according to Figure 4.3.

First, all boron doped cells have higher electric fields than the undoped cell at the n-side of the i-layer. Secondly, sharp decreases of the electric fields mark the onset of the doped zones. For the zone III doped cell, the high field region is limited to the n-i interface region, for the zone II doped cell the onset of the doping can be seen in the centre of the i-layer. For the zone I doped cell a relatively small uniform field increase is observed. These distribution profiles of the electric field can be directly understood by applying Poisson's equation (Eqn. 2.23), which predicts that the electric field at the n-i interface should increase with decreasing distance of the doped zone from

the n-i interface. It can thus be concluded that at 0 V applied voltage, the low-level boron doping schemes used here do indeed displace the electric field in the p-i-n cells in the way as is expected from acceptor doping.

Figure 4.5 shows the annealed-state JV-curves of the graded boron-doped solar cells for different illumination conditions. For all illumination conditions, the current collection at forward voltages is reduced as compared to the collection in an undoped solar cell. These reductions can be directly understood as the carrier collection in the zones of low electric fields being suppressed. E.g. the reduction of the collection is much stronger for p-side AM1.5 illumination than for n-side AM1.5 illumination, as expected from the general reduction of the p-side electric fields due to boron

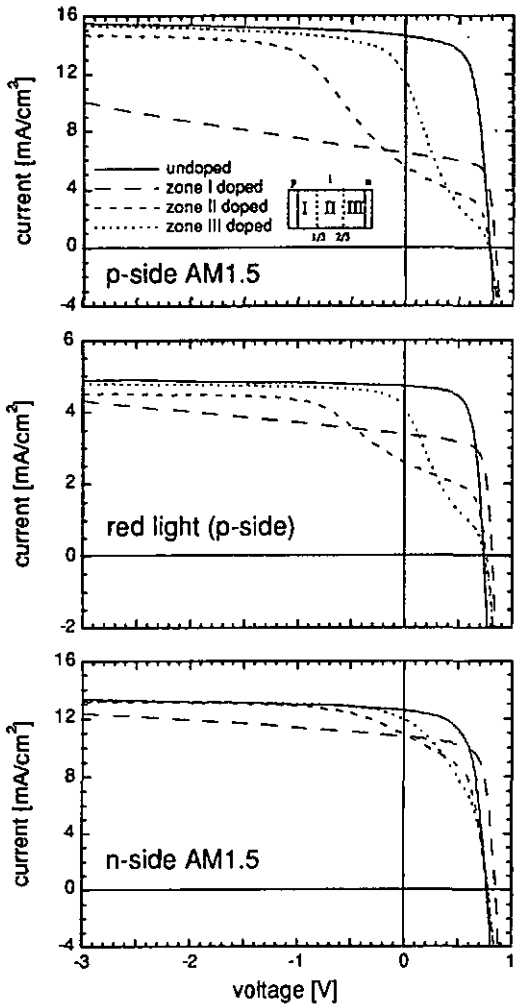

Figure 4.5: Annealed state JV-curves of p-i-n solar cells with different low-level graded i-layer boron doping according to Figure 4.3, under p-side AM1.5, red light (AM1.5, λ > 610 nm), and n-side AM1.5 illumination.

doping. For reverse voltages, the current collection tends to attain the (complete) collection of the undoped cell. The fact that already at moderate reverse bias voltages all photo-generated carriers can be collected shows that the low-level doped zones have reasonably large photo-carrier lifetimes and are by no means photovoltaically dead layers such as e.g. the highly doped p- and n-layers of a p-i-n solar cell.

The DICE collection probability profiles of the doped cells (Figure 4.6, left) confirm that the collection is directly governed by the local electric fields (as shown in Figure 4.4) rather than by an enhanced recombination in the doped zones themselves: whereas for zone I doping the collection at + 0.6 V is high for the whole i-layer except for the region close to the p-i interface, for zone III doping the collection is suppressed over most of the i-layer, except for the (doped) region close to the n-i interface. As the red light current collection is proportional to the average collection from the entire i-layer, the areas under the + 0.6 V DICE profiles scale directly with the red light currents at + 0.6 V of Figure 4.5.

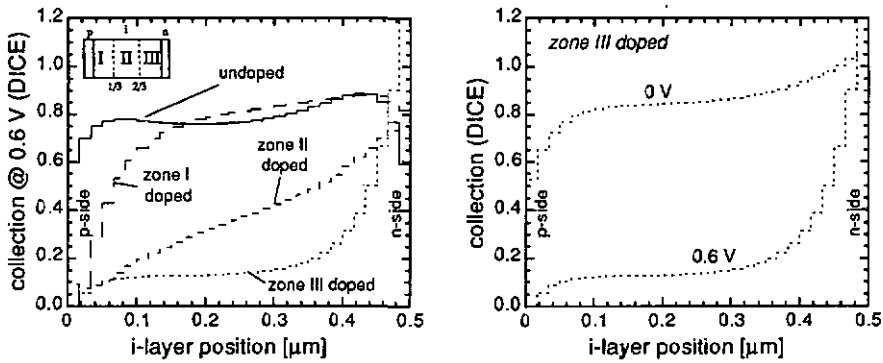

Figure 4.6: Bifacial DICE collection probability profiles in graded boron doped p-i-n solar cells. Left: collection at 0.6 V of differently doped p-i-n cells; Right: collection of zone III doped cell as a function of voltage bias (doping profiles according to Figure 4.3).

The pronounced differences found in the voltage dependence of the collection can be understood by considering the details of the electric field propagation in the i-layer of the solar cell: For low applied voltage (forward), the electric field will only extend over the region between the n-layer and the low-level doped zone (which acts as a weakly doped p-layer). With increasing applied voltage (reverse) the acceptors in the low-level doped zone become more and more ionised until the electric field extends also into the zone between the p-layer and the low-level doped zone. This is confirmed by Figure 4.6 (right), showing the collection profile for the zone III doped cell, at 0 V and at +0.6 V applied external voltage. In line with the JV-curve behaviour of this cell, the collection from the bulk region is largely recovered by a change in the applied voltage from 0.6 V to 0 V. This can be understood as the electric field being limited to the n-i interface region at 0.6 V, and extending throughout the whole i-layer at 0 V. The sharp features seen in the JV-curves of both the zone II and III doped cells indicate that the extension of the electric field to the p-side of the doped zone does not occur gradually, but within a narrow, well defined voltage range.

Evaluation of the dopant charge density by the blue light collection threshold

The onset of the collection on the p-side of the i-layer can be directly probed by strongly absorbed light incident on the p-side (Figure 4.7). Unlike the cases where the generation is distributed over the whole i-layer (white or red light, Figure 4.5), the collection of photo carriers generated in the p-i interface region alone is completely cancelled at forward voltages. As the completely cancelled p-side collection has to be associated with a suppressed electric field in this region, this demonstrates that a doping concentration of 2 ppm B_2H_6, with a sufficient volume of the doped zone, produces an electrostatic potential similar to that of a highly doped p-layer. As the doped zones II and III are remote from the region probed by the light, doping induced life-time effects can clearly not be the cause of the observed collection decrease.

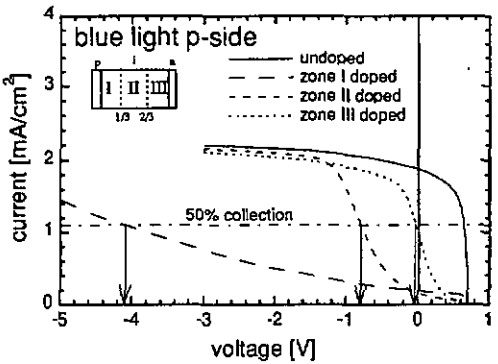

Figure 4.7: p-side blue light (AM1.5 filtered λ < 460 nm) JV-curves of graded boron doped p-i-n solar cells (doping profiles according to Figure 4.3).

For an increasing applied (reverse) voltage, the collection is found to rapidly grow to 100 %, defining a critical threshold voltage for each doping position (with exception of the zone I doped cell: this cell shows a gradual increase of the collection). The critical voltage systematically increases as the doped zone moves towards the p-side. The sharpness of the collection increase at the critical voltage calls for a further quantitative analysis.

A simple model linking the doping position to the threshold voltage is illustrated in Figure 4.8: For an acceptor density N_A, the total integrated negative charge of the doped fraction of the i-layer is $N_A \cdot L/3$ per unit area (one third of the i-layer is doped). This total charge is taken to be concentrated in a single sheet of charge of negligible width at the i-layer position x. Poisson's equation is then used to relate the electric field on the p-side (E_1) and the n-side (E_2) of the doping charge sheet (q is the elementary charge, ε is the dielectric permittivity):

$$E_2 - E_1 = \frac{q}{\varepsilon} \cdot N_A \cdot \frac{L}{3} \qquad (4.1)$$

The integration of the electric field over the whole i-layer must equal the applied potential:

$$E_1 \cdot x \cdot L + E_2 \cdot (1-x) \cdot L = |V_{ext} - V_{bi}| \qquad (4.2)$$

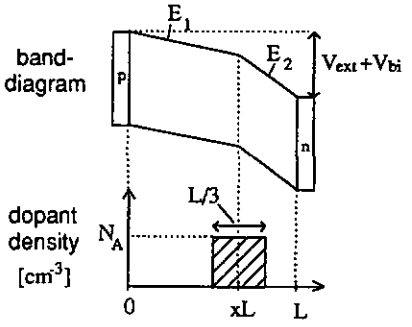

Figure 4.8: Schematic model of electric fields and doping profile as used for the acceptor space-charge density evaluation of the graded boron doped p-i-n solar cells (doping profiles according to Figure 4.3)

At the critical voltage $V_{ext} = V_{critical}$, defined by the onset of the p-side collection, it is assumed that the electric field at the p-side of the doped zone E_1 is exactly cancelled:

$$E_1 = 0 \tag{4.3}$$

It could be argued that for the collection to set on, a certain minimal electric field E_1 is required. Such a minimal electric field could be estimated from the difference between the built-in potential and V_{OC} in standard, undoped p-i-n cells. This difference of 0.2 - 0.3 V can be regarded to give a rough estimate of the error on the voltage scale caused by the simplified assumption $E_1 = 0$. Clearly this error remains small as compared to the magnitude of the measured threshold voltages ($\geq$ 1 V). By combining Eqns. 4.1, 4.2, and 4.3, the dopant charge density as a function of x and $V_{critical}$ is

$$N_A = \frac{3}{L^2} \cdot \frac{\varepsilon}{q} \cdot \frac{|V_{critical} - V_{bi}|}{(1-x)} \tag{4.4}$$

Table 4.I shows the evaluation of the acceptor density N_A for the three doping positions. The built-in potential V_{bi} was assumed to be 1 V in all cases. Given the simplicity of the model, the result yields fairly consistent densities N_A of $3 - 4 \cdot 10^{16}$ cm^{-3}. According to SIMS measurements of materials identical to the low-level boron doped i-layers used here, the total boron concentration in 2 ppm B_2H_6 doped films is $3 \cdot 10^{17}$cm^{-3} (Fig. 2.36). The fraction of active, 4-fold co-ordinated boron dopants can thus be estimated to amount to 10 - 15 % of the boron atoms incorporated in the material. This is similar to values found in the literature [BEY84].

Table 4.I: Evaluation of the acceptor density N_A in graded 2 ppm B_2H_6 doped p-i-n solar cells by the p-side blue light collection threshold (doping profiles according to Figure 4.3)

doped zone	x	$V_{critical}$	$\lvert V_{critical} - V_{bi} \rvert$	N_A
		V	V	cm^{-3}
I	0.17	- 4.2	5.2	$4.7 \cdot 10^{16}$
II	0.5	- 0.8	1.8	$2.8 \cdot 10^{16}$
III	0.83	- 0.1	1.1	$4.5 \cdot 10^{16}$

Remark on the numericol modelling of the low-level i-layer doping

As mentioned in section 2.1, the modelling of dopants requires to define a mechanism that neutralises the dopant space-charge when the local Fermi-level is approaching the band-edges. If this mechanism is not implemented, at forward voltages the electrostatic potential within the i-layer of the modelled solar cells with i-layer doping can reach values beyond the range defined by the respective potentials of the two doped layers. In this work, the neutralisation of the dopant charge is realised in an indirect way by the tail-state occupation (see section 2.1.5). As a consequence, the modelling of solar cells with low-level i-layer doping requires to model the i-layer tail-states, even if this was not necessary for the modelling of solar cells with non-doped i-layers (see section 3.2.3).

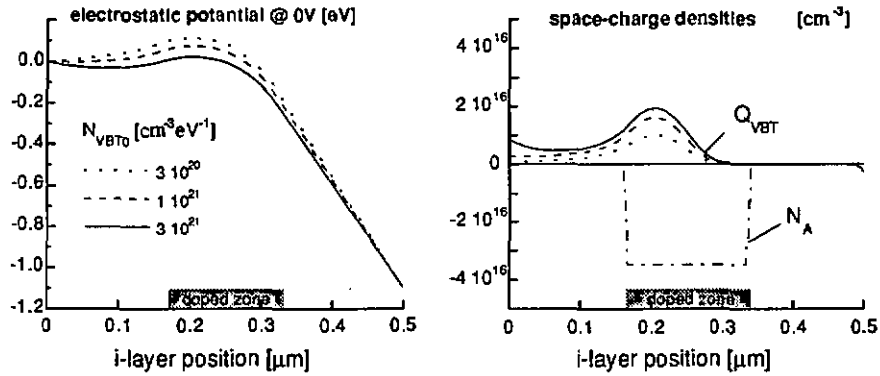

Figure 4.9: Numerically simulated electrostatic potential and space-charges in a graded boron doped p-i-n cell as a function of the valence-band edge density of states N_{VBT0}. The ionised acceptor density N_A is $3.5 \cdot 10^{16} cm^{-3}$ in zone II (see Table 4.1). Otherwise the modelling parameters correspond to the standard parameters of Table 2.1.

The limiting influence of the tail-states on the modelled electrostatic potential can be demonstrated by a low-level boron-doped cell. The example corresponds to the zone II, 2 ppm boron doped cell of the previous sections. The assumed acceptor density in the doped zone corresponds to the one experimentally determined for 2 ppm doped materials (see above). Figure 4.9 shows the modelled electrostatic potential, and the i-layer space-charges at 0 V external voltage. This voltage is below the measured threshold voltage of the p-side collection, thus the dopant charge in the centre of the i-layer is considered to be only partially ionised, and the potential towards the p-side of the cell is assumed to be constant (E = 0). Figure 4.9, left, shows the limiting effect of the total number of available valence-band tail states on the maximal electrostatic potential reached in the middle of the i-layer. The limitation is by a partial compensation of the negative acceptor charge by the positive valence-band tail charge (Figure 4.9, right); the balance of these two space-charge contributions leads to the expected, approximately constant electrostatic potential on the p-side of the doped zone if a sufficiently high number of valence-band tail states is assumed.

Figure 4.10, left, shows the simulated blue light, and red light voltage dependent collection of the modelled zone II doped p-i-n solar cell (to be compared with the measured collections in Figs. 4.5 and 4.7). Clearly, the typical features of the measured curves, especially the threshold around -1 V, are realistically reproduced. Figure 4.10, right, shows the corresponding electrostatic potentials, and electric fields in the doped cell that explain the modelled collection behaviours.

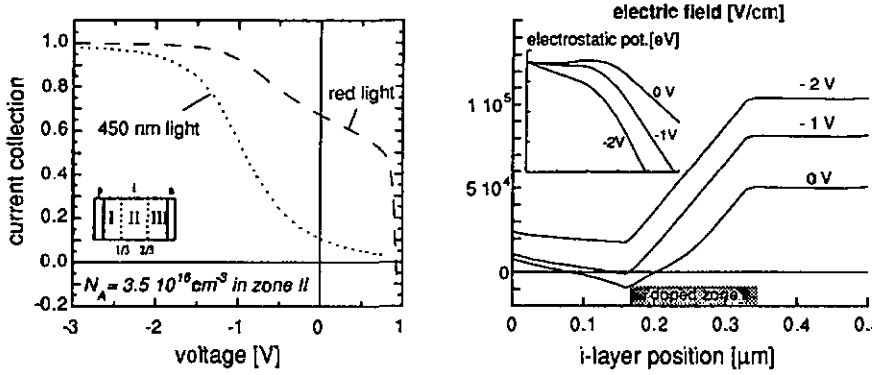

Figure 4.10: Numerically simulated p-side blue and red light JV, and the voltage dependent space-charge and electrostatic potential, of a graded boron doped p-i-n cell. The ionised acceptor density N_A is $3.5 \cdot 10^{16} cm^{-3}$ in zone II (see Table 4.1). Otherwise the modelling parameters correspond to the standard parameters of Table 2.1.

Conclusions on the low-level i-layer doping with boron

In summary, the results of the low-level graded boron doping in the i-layer show that the doping induces changes of the electric field as expected from the presence of shallow acceptor-like states in the doped zones of the i-layer. The experimental results can be entirely understood in terms of modified electric field distributions in the i-layer. This description is precise enough to even allow for a consistent quantification of the acceptor densities involved. At a doping concentration as low as 2 ppm B_2H_6, the boron doping is shown to have the capability to displace the electrostatic potential in the i-layer very near to the potential of the (highly doped) solar cell p-layer itself. Also, there are no indications that the material significantly deteriorates due to low-level doping.

It is worthwhile to compare the above results with some recent solar cell modelling studies that employ the 'defect-pool' model [ASE92, BRU92]. The 'defect-pool' idea in general predicts an exponential growth of defects as the Fermi-level is displaced from mid-gap. In the cited studies, the 'defect-pool' has been implemented in p-i-n solar cell models in a way that leads to very high defect densities at the i-layer interfaces (10^{17}-10^{18} cm^{-3}). This causes a concentration of the built-in field at the interfaces, with the electric field in the bulk of the i-layer virtually cancelled (in the initial state)[ASE92]. Obviously, the degree of suppression of the i-layer electric field depends strongly on the parameters of the defect pool, in particular on the onset of the defect growth as a function of the Fermi-level.

However, the above measurements of the low-level boron doped p-i-n solar cells can clearly not be understood on the basis of an i-layer electrostatic potential pinned to the middle of the gap by a Fermi-level dependent defect growth. Rather, the explanation of the collection and of the electric field measurements demands for a model, including a 'defect-pool' mechanism or not, that allows for a shift of the i-layer potential over an important fraction of the gap without the massive creation of defects. (see figure 4.11) Also, the model must be compatible with the fact that those shifts can be effected by relative low densities of dopants (e.g. by $3 - 4 \cdot 10^{16}$ acceptors per cm^{-3}). The observations do however not exclude that, beyond a 'relatively free' section of the gap of the order

of 0.7 - 1 eV, defect-pool like mechanisms, in parallel with the tail-states, limit the displacement of the Fermi-level.

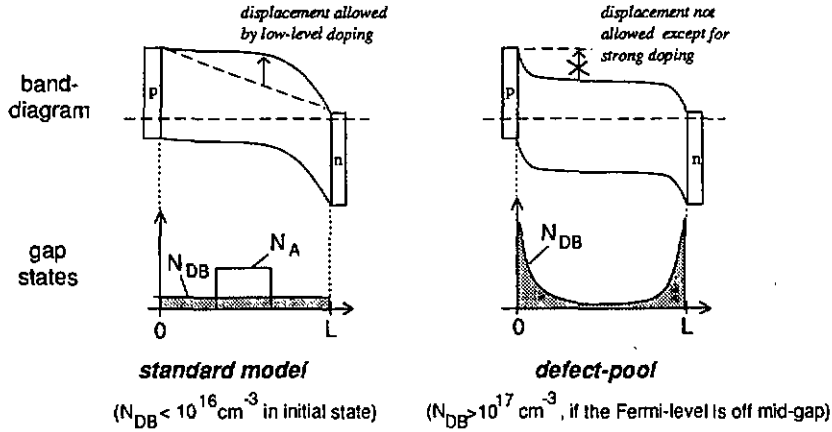

Figure 4.11: Schematic band-diagram and gap-states in the i-layer of p-i-n solar cells employing a standard or a 'defect-pool' defect model. In the 'defect-pool' case, the shift of the i-layer potential by low-level doping (in the 10^{16}cm^{-3} range) can not be explained.

4.2.2 Phosphorus doping

Phosphorus doping in a-Si:H creates donor states, i.e. states that are positively charged when ionised. If applied in the i-layer of a p-i-n cell, contrary to boron doping, the positive space-charge leads to a reduced electric field between the n-layer and the doped zone, and to an increased electric field between the doped zone and the p-layer (Figure 4.12). As discussed above, the electric field is only displaced within the i-layer, while the total potential drop between the p-layer and the n-layer stays constant.

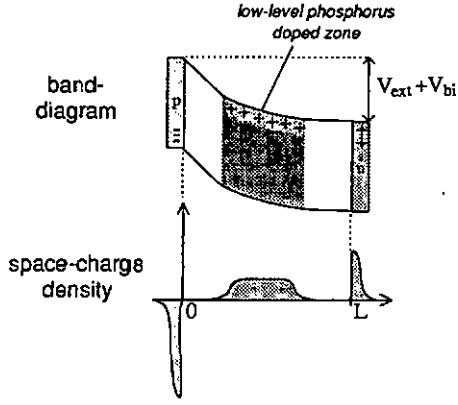

Figure 4.12: Schematic influence of graded i-layer doping with phasphorus (donors), on the band-diagram and space-charge density in a p-i-n solar cell.

The detailed influence of graded phosphorus doping on the electric field and the collection of p-i-n solar cells is analysed in solar cells doped partially with 1 ppm PH_3. In general, behaviours were found to be analogous to the ones observed for boron doping. Figure 4.14 shows the JV-curves for different illuminations of zone I and III phosphorus doped cells. The JV patterns are readily explained with high electric fields towards the p-side of the doped zones, and a voltage dependent

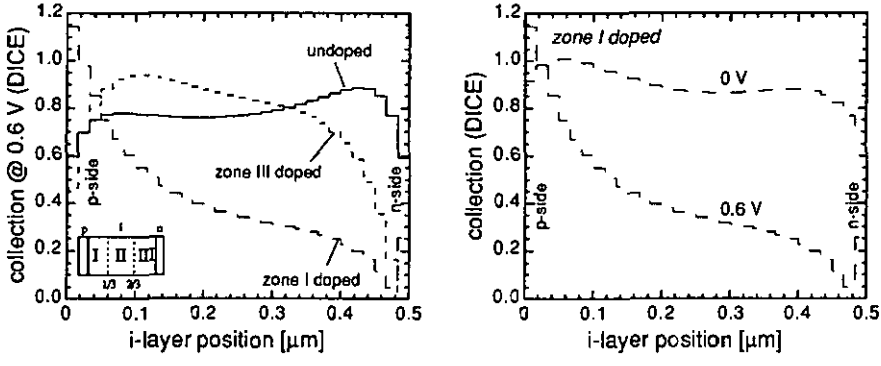

Figure 4.13: Bifacial DICE collection probability profiles in graded phosphorus doped p-i-n solar cells. Left: collection at 0.6 V of differently doped p-i-n cells; Right: collection of a zone I doped cell as a function of voltage bias (1 ppm PH_3 in the doped zone).

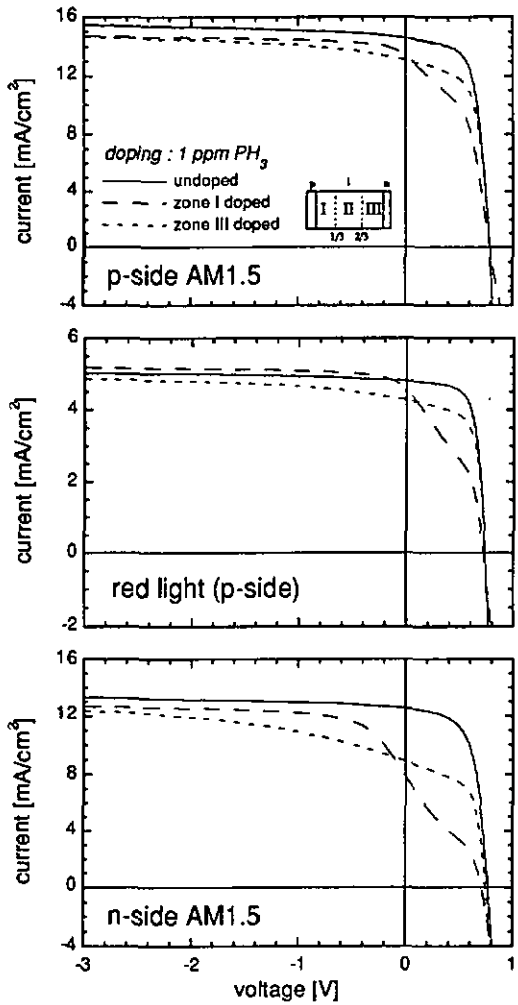

Figure 4.14: Annealed state JV-curves of p-i-n solar cells with different low-level graded i-layer phosphorus doping (1 ppm PH_3 in the doped zone), under p-side AM1.5, red light (AM1.5, $\lambda > 610$ nm), and n-side AM1.5 illumination.

extension of the electric fields towards the n-side of the i-layer, analogous to the boron doping (Figure 4.5). Obviously the same applies to the underlying i-layer collection profiles, shown in Figure 4.13 (to be compared with Figure 4.6).

The donor concentration in the doped zones was evaluated from the collection threshold of strongly absorbed light incident from the n-side (analogous to the analysis of the acceptor charge in boron doped cells of section 4.2.1). Figure 4.15 shows the corresponding measurements for zone I and III 1 ppm phosphorus doped cells. Differently from the partially boron doped solar cells (Figure 4.7), the collection is not completely suppressed at forward voltages, but rather a collection of about

30 % persists up to high forward voltages. This effect points towards a limitation of the low-level phosphorus doped i-layer sections to attain the full electrostatic potential of the highly doped n-layer. In this view, a certain n-i interface barrier remains at the n-i interface, even if the bulk electric field is cancelled by the i-layer doping (see Figure 4.15, right). This explanation is for the moment just a speculation; a study employing higher phosphorus concentrations would be needed to better understand the detailed mechanisms at the n-i interface.

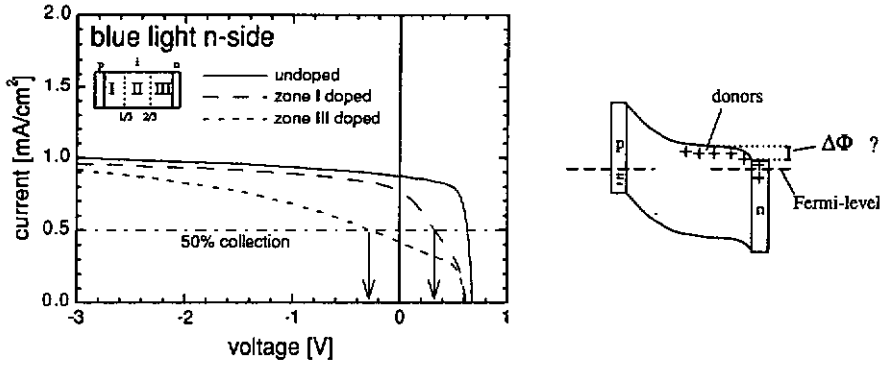

Figure 4.15: n-side blue light (AM1.5 filtered $\lambda < 460$ nm) collection of graded phosphorus doped p-i-n solar cells (1 ppm PH_3 in the doped zone).

With the only partial suppression of the collection at the n-i interface, also the threshold voltage for the zone I phosphorus doped cell is not as well defined as for the analogous case of zone III boron doping (Figure 4.7, zone III doped). But still, the approximate threshold voltage (set at 50 % collection) is again decreasing with increasing distance of the doped zone from the probed interface, as predicted by Poisson's equation. The quantitative analysis yields donor concentrations of $1 - 3 \cdot 10^{16}$ cm^{-3} in the 1 ppm PH_3 doped zones (Table 4.II). With a total phosphorus concentration of $1 \cdot 10^{17}$ cm^{-3} (determined by SIMS, see Figure 2.36), the fraction of active, 4-fold co-ordinated phosphorus is thus 10 - 30 %. This is in the range reported in the literature [BEY84].

Table 4.II: Evaluation of the donor density N_D in graded 1 ppm PH_3 doped p-i-n solar cells by the n-side blue light collection (Eqn. 4.4)

doped zone	x (from n-side)	$V_{critical}$ V	$\lvert V_{critical} - V_{bi} \rvert$ V	N_D cm^{-3}
I	0.83	+ 0.3	0.7	$3.1 \cdot 10^{16}$
III	0.17	- 0.3	1.3	$1.2 \cdot 10^{16}$

4.2.3 Basic effects of light-soaking in p-i-n solar cells with low-level doped i-layers

For the low-level doped solar cells presented above (sections 4.2.1 and 4.2.2), the dopant concentrations are such that in the annealed state, the dopant charge is clearly dominating the i-layer space-charge (dopant densities of $1 - 4 \cdot 10^{16}$ cm^{-3}). But after light-soaking, the number of dangling-bonds is raised to concentrations ($N_{DB} \approx 1 - 5 \cdot 10^{16}$ cm^{-3}, see chapter 3) similar to the ones of the dopants. The electric field in the degraded low-level doped solar cells becomes thus determined by a balance of both the dopant and the dangling-bond space-charge, and during the degradation, major shifts of the electric field distribution are expected to occur while the growing dangling-bond space-charge competes with the fixed dopant charge.

Recovery of the collection of boron doped p-i-n cells during light-soaking

Figure 4.16 shows the measured influence of the light-soaking on the collection of graded boron (left) or phosphorus (right) doped cells. In the cells with graded boron doping, the i-layer sections, in which the annealed state collection is suppressed by low local electric fields, show a recovery of the collection after the light-soaking. A similar increase of the p-side collection was found in an independent investigation for a p-i-n solar cell with constant i-layer boron doping [ONI91]. Within the framework of competing dopant and defect charges, these recovery effects in boron doped cells are explained by the compensation of acceptor charges by positively charged dangling-bonds, effecting an increase of the initially suppressed electric field on the p-side of the i-layer.

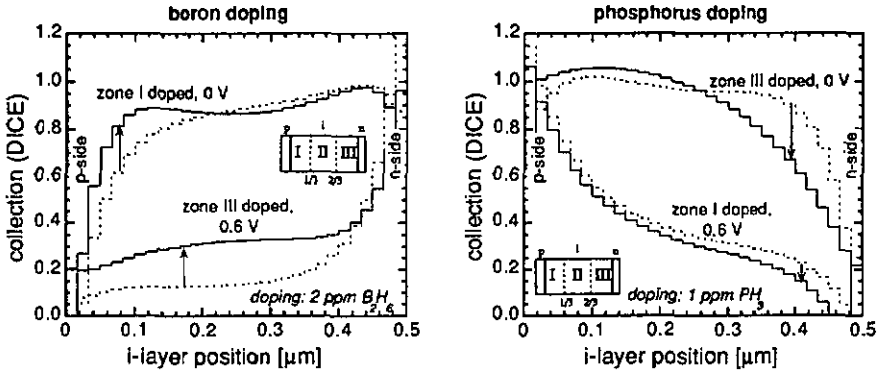

Figure 4.16: Collection profiles in graded doped p-i-n solar cells in the annealed state (doshed lines, and after light-soaking. Left: collection in graded boron doped p-i-n cells (2 ppm B_2H_6 in the doped zone); Right: collection in graded phosphorus doped p-i-n cells (1 ppm PH_3 in the doped zone). Light-soaking was at 1 sun (see Figure 3.3), for approx. 20 hours.

For the phosphorus doped cells, no recovery effects due to the light-soaking are observed. On the n-side of the i-layer, where the annealed state electric field is suppressed by the donor charge, the collection is further decreased by the degradation. Those regions at the n-side show actually the strongest decrease of the collection of the whole i-layer, similar to what is observed in cells without i-layer doping (Figure 3.7). This behaviour of the phosphorus doped cells confirms in fact the conclusion from the observations and modelling of undoped cells (section 3.2), i.e. that no significant negative dangling-bond space-charge is present in the i-layer of degraded solar cells.

The important recovery effects seen in the boron doped cells on the other hand confirm the presence of an important positive space-charge after the light-soaking.
Figure 4.17 shows the evolution of the i-layer collection (left), and of the red light JV-curve (right), of a zone II boron doped solar cell. It is shown that the increase of the p-side collection due to the favourable electric field re-arrangements occur already after a relatively short time of light-soaking. With progressing light-soaking time, some of the initial gains of the collection are lost again, but even after a few hundred hours the collection stays clearly higher than in the initial, annealed state. The corresponding short-circuit current (see Figure 4.17, right) scales directly with the time dependent changes seen in the i-layer collection. Not only the collection at 0 V, but also the power output of the solar cell shows a clear recovery in the initial phase of the light-soaking (Figure 4.17, right, inset). Similar observations, yet without the corresponding interpretation in terms of space-charge compensation, were also made in independent investigations [KUS85, GOR86, KUW87].

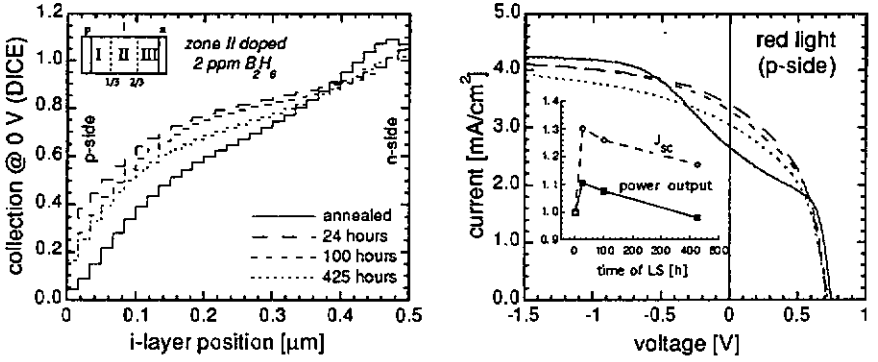

Figure 4.17: Light-soaking of a graded boron doped p-i-n solar cell (doping: 2 ppm B_2H_6 in zone II). Left: evolution of the i-layer collection at 0 V; Right: JV-curve for homogeneously absorbed light (AM1.5 at 100 mWlcm², λ > 610 nm), inset: J_{SC} and power output as a function of light-soaking time. Light-soaking was at 1 sun (see Figure 3.3).

Influence of the defect position on the recovery effect in boron doped solar cells

Graded boron doped cells were light-soaked with strongly absorbed light to create dangling-bonds only locally in the vicinity of the illuminated interface, and not in the whole i-layer. To enhance the confinement of the light-generated carriers, the degradation was carried out under short-circuit condition. Figure 4.18, left, shows the evolution of the p-side collection (represented by the spectral response of 500 nm light), for p-side or n-side light-soaking with strongly absorbed light.
As a result, it is clearly the light-soaking from the p-side that leads to a strong recovery of the p-side collection. Light-soaking from the n-side in turn proves ineffective in recovering the p-side collection. If one admits that the defect creation is in fact confined to the illuminated zones, this result corroborates the model of p-side dangling-bonds, positively charged due to their vicinity to the p-i interface, being at the origin of the observed recovery effects.
The collection in the n-side region of the i-layer (Figure 4.18, right) it is found to be decreased fast by the n-side light-soaking, and much slower by p-side light-soaking. This is equivalent as to what was found for solar cells without low-level doping (Figure 3.11). Again, also after the supposed dangling-bond creation in the n-i interface region alone, there is no evidence of a significant

negative dangling-bond space-charge, and of a corresponding electric field increase at the n-i interface.

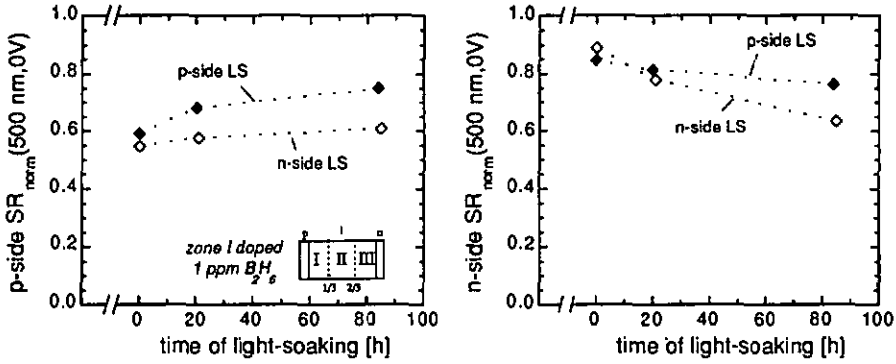

Figure 4.18: p-side (left) and n-side (right) normalised spectral response at 500 nm (penetration depth ~ 0.05 μm) of a graded boron doped p-i-n solar cell (doping: 1 ppm B_2H_6 in zone I) during light-soaking with strongly absorbed light. Light-soaking is from the p-side (closed symbols) or the n-side (open symbols), with 450 nm light, with the light generated current adjusted to 13 mA/cm^2. During light-soaking, the solar cells are at short-circuit condition.

4.3 Electric field profiling for an optimal degraded state performance

In the previous section, the fundamental effects of low-level graded i-layer doping on the p-i-n solar cells were demonstrated. The implementation of various doping profiles showed that the i-layer electric field can be manipulated in a controlled way, that the dopant concentrations to achieve these manipulations do not seem to significantly degrade the i-layer material, and that after light-soaking a balance of dopant and defect charge defines the degraded state electric field in those graded doped p-i-n cells. These experimental findings suggest indeed a practical potential of the graded doping to improve the degraded state performance of p-i-n cells as proposed at the beginning of this chapter. In this final section, based on the different modelling and experimental results from above, the graded low-level doping will be specifically applied to realise solar cell performance gains.

4.3.1 Modelling predictions

Intuitively, electric field distortions, which are caused by a given i-layer space-charge profile, are compensated by a doping profile that follows the inverted space-charge profile. Thus to compensate the dangling-bond space-charges that cause the distortion of the electric field in the degraded solar cells, boron doping (acceptors) has to be applied in the p-side regions of the positively charged dangling-bonds, and phosphorus doping (acceptors) has to be applied in the n-side regions of the negatively charged dangling-bonds.

The 'ideal' doping profile

The detailed shape of the dangling-bond space-charge was numerically modelled and discussed in section 3.2. If the typical simulated space-charge distributions (see e.g. Figure 3.14) are directly inverted, and the corresponding doping profile is implemented in the model, one does not achieve an ideally compensated, constant electric field. This is due to the coupling of the different mechanisms governing the operating solar cell (Eqn. 2.3 - 2.7), causing the dangling-bond space-charge in the compensated solar cell to be different from the one determined under the conditions of the distorted electric field.
To determine the 'ideal' doping profile, one can artificially break the coupling between the electric field distribution and the space-charge (i.e. Poisson's equation, Eqn. 2.3) in the numerical solar cell model. In this scheme, the electric field is arbitrary set to be constant (to its desired shape), that is Eqn. 2.3 is replaced by

$$\frac{dE(x)}{dx} = 0 \neq f(Q_{DB}) \tag{4.5}$$

With this modification, the solar cell operation is modelled as if the electric field would already be compensated. The total dangling-bond space-charge determined under these conditions yields directly the 'ideal' doping profile, taking into account the detailed carrier transport and recombination under the constant electric field. Figure 4.19 shows the dangling-bond charge with or without compensated electric fields, and the correspondence to the 'ideal' dopant profile for the case of red light illumination. For the presented example, the dangling-bond occupations do not change strongly after the compensation, the effect of the coupling is thus small and the occupations of the non-compensated case yield a profile already close to the 'ideal' doping profile.

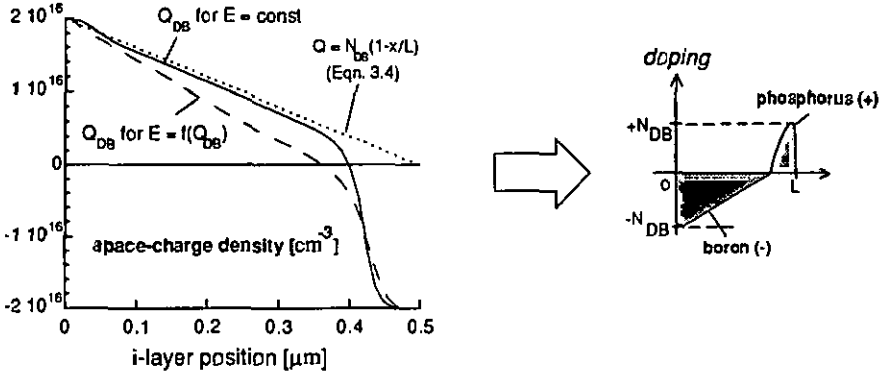

Figure 4.19: Left: Numerically simulated space-charges, and an analytically determined doping profile, in a 0.5 µm thick p-i-n cell, at 0 V, and for $N_{DB} = 2 \cdot 10^{16}$ cm^{-3}. Broken line: Q_{DB} for a standard simulated electric field (according Eqn. 2.3: $dE/dx = f(Q_{DB})$); full line: Q_{DB} for a constant electric field ($dE/dx = 0$ in Eqn. 2.3). Illumination: homogeneously absorbed, 16 mA/cm^2. The other parameters are the standard parameters of Table 2.1, with the tail-states not modelled. Right: schematic i-layer doping profile corresponding to a constant electric field.

The role of the generation profile

To estimate the improvement potential of the electric field compensation, Figure 4.20 shows the simulated degraded state JV-curves of a solar cell with the electric field set constant (Eqn. 4.5), and of a standard solar cell with the distorted (Eqn. 2.3) electric field (Remark: Obviously, in real graded doped cells with a fixed doping profile, the electric field can only be set constant at one single voltage; this voltage will be in the region of interest around the maximum power point). The simulations are given for AM1.5 illumination, and for red light illumination.
Interestingly, for AM1.5 illumination, the simulation indicates no gains due to the electric field compensation. It thus appears that for AM1.5 illumination, a compensated, constant electric field has no advantage over the intrinsic electric field prevailing in these cells. Two factors explain this behaviour:

- the overall electric field distortion is smaller under the inhomogeneous carrier generation of the AM1.5 illumination (Figure 3.15) than under homogeneously absorbed light. Therefore, the potential for a gain is also more limited.
- the increase of the electric field in the back part of the i-layer that is achieved by the compensation enhances the current collection of only a minor part of the total current. In the region of the major current generation at the front, the electric field is reduced, increasing the losses in that region.

Experimentally, for standard single junction p-i-n cells, the optimal degraded state i-layer thickness is 0.2 - 0.3 µm [BEN86, LEC91, BER93]. At these thicknesses, the total variation of the generation rate is smaller than in the 0.5 µm thick solar cells considered above, and an efficiency gain through electric field compensation could be possible. On the other hand, the magnitude of the electric field distortion is reduced at those small i-layer thicknesses, limiting the improvement potential.

For the conversion of a homogeneously absorbed, red light illumination on the other hand, substantial gains seem to be possible by the electric field compensation (Figure 4.20, right). This is explained by a larger potential due to a more pronounced electric field distortion under this illumination (Figure 3.15). Also, the fact that under red light illumination the different sections of the i-layer contribute equally to the total current makes the constant electric field clearly more favourable than the distorted field of the standard cells.

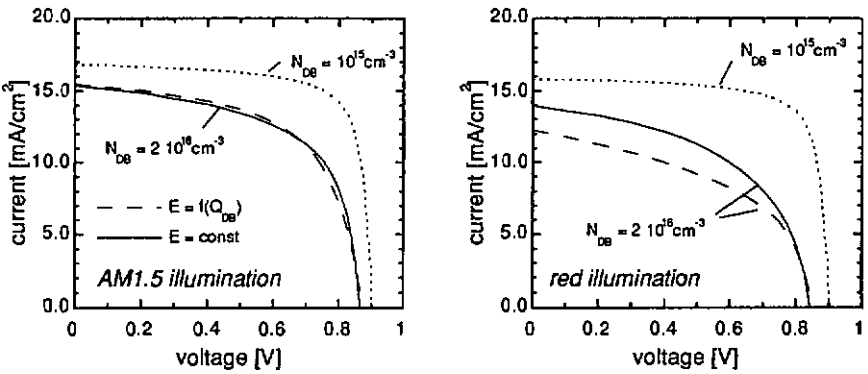

Figure 4.20: Numerically simulated JV-curves for differently simulated electric fields, under AM1.5 illumination and under homogeneously absorbed red light illumination. Dashed lines: standard simulated electric field (according Eqn. 2.3: $dE/dx = f(Q_{DB})$), $N_{DB} = 2 \cdot 10^{16}$ cm^{-3}; full lines: constant, compensated electric field ($dE/dx = 0$ in Eqn. 2.3), $N_{DB} = 2 \cdot 10^{16}$ cm^{-3}; dotted lines: initial state, $N_{DB} = 1 \cdot 10^{15}$ cm^{-3} (no differences as a function of the electric field are observed). The other parameters are the standard parameters of Table 2.1, with the tail-states not modelled.

Strategy for realistic doping attempts

As discussed in chapter 3.1, the achievable performance of amorphous silicon cells is presently limited by the relative poor stability of the second cells in 2-fold multijunction cells. These second cells have to convert a rather homogeneously absorbed light-spectrum, because the high generation peak of the AM1.5 spectrum (Figure 2.2) is absorbed in the first cell. Also, the range of thickness found to be optimal for the second cells is presently around 0.4 µm [CAT91, ICH93]. In this thickness range, and for a homogeneously absorbed illumination, the effects due to the electric field distortion are important enough to expect substantial performance gains from a suitable electric field compensation. In the following, the focus shall thus be on the conversion of homogeneously absorbed light, with the goal to develop a graded doping scheme to be applied in the second cells of 2-fold multijunction cells.

Figure 4.19 schematically showed the 'ideal' doping profile, i.e. the one needed to achieve a constant field at 0 V external voltage, and for homogeneously absorbed light. This profile is characterised by a gradually decreasing boron concentration tailing wide into the bulk of the i-layer, and a much less important region of phosphorus in the vicinity of the n-i interface. As seen in chapter 3.2, the detailed shape of this profile depends strongly on the various modelling parameters (mobilities, cross sections, etc.). Considering the relative uncertainty of these parameters, as well as of the employed models in general, the modelling results shall thus be summarised by only two general implications:

- i-layer doping with boron addresses the major part of the suspected electric field distortions
- the boron doping should be applied in a continuos profile that starts at the p-i interface, and that gradually decreases in the bulk of the i-layer

The first implication also arises from the general experimental observation that in the degraded solar cells, the collection is decreased mostly towards the n-side of the i-layer (Figure 3.7). Independent of the actual mechanism causing this asymmetry, the measured behaviour alone implies the use of boron doping, because it is only by boron doping that electric field can be moved towards the n-side of the i-layer to increase the local collection of that region. The application of phosphorus doping cannot be expected to be beneficial: the measured degraded state collection reaches its lowest value directly at the n-i interface, and also the experimental findings give no indication of any substantial negative dangling-bond space-charge at the n-side of the i-layer (section 4.2.3).

The second implication of using a continuos, decreasing boron profile is rooted in the assumption of the presence of dangling-bonds in the whole bulk of the i-layer. If this model is true, it forces the use of a continuos doping profile to reduce the electric field distortion. Alternative boron doping schemes can not suitably address the electric field distortion: If the boroo is limited to the region near the p-i interface, it can in principle not affect the electric fields in the back of a p-i-o cell. Also, the application of boron only in the n-side region, without a continuos grading starting at the p-i interface, can fundamentally not result in a homogenous electric field distributioo. This is illustrated in Figure 4.21: With a non-continuos boron doping in the centre of the i-layer, the electric field can be efficiently restored in the back of the i-layer, but with the consequence that the electric field collapses in the front. This is a direct consequence of the fact that the positive dangling-bond space-charge will always start directly at the p-i interface, intrinsically requiring a local compensation by a continuos doping profile originating at the p-i interface, too. Finally, the requirement of a decreasing profile arises from the fact that the positive space-charge to be compensated will also decrease towards the interior of the solar cell, following the change of the local carrier concentration ratios.

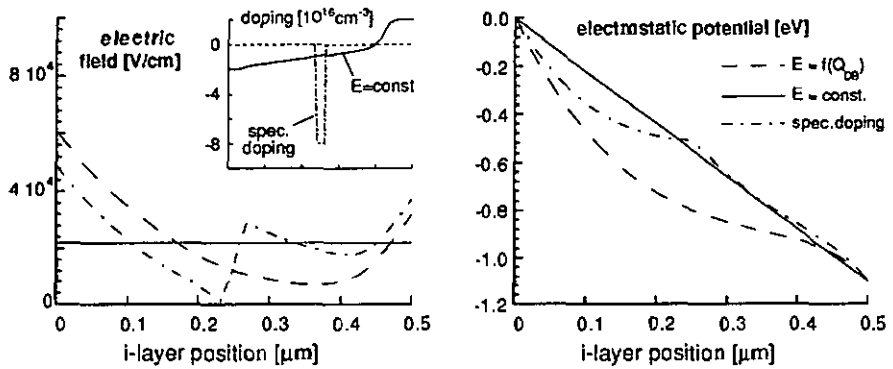

Figure 4.21: Numerically simulated electric field and electrostatic potential at 0 V external voltage, for homogeneously absorbed red light illumination, and $N_{DB}=2\cdot10^{16}$ cm^{-3}. Dashed lines: undoped case; full lines: constant electric field case (equivalent doping see inset); dashed-dotted lines: doping with $N_A=8\cdot10^{16}$ cm^{-3} in a 0.05 µm wide slab in the centre of the i-layer (see inset). The other parameters are the standard parameters of Table 2.1, with the tail-states not modelled.

4.3.2 Experimental implementation of boron profiles for optimised red light conversion

Based on the above considerations, the i-layers of p-i-n solar cells were doped with boron employing linearly decreasing doping profiles. The doping was designed to start at the p-i interface, and to reach zero at two thirds of the total i-layer thickness.

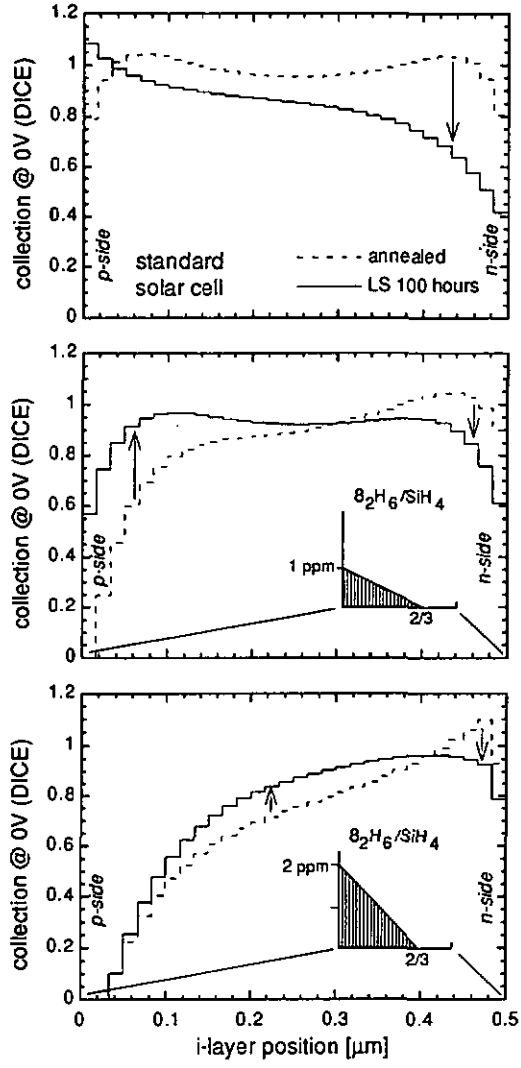

Figure 4.22: Bifacial DICE collection probability profiles in graded boron doped p-i-n solar cells, at 0 V, in the annealed state, and after 100 hours of light-soaking. The graded doping profiles are linearly decreasing form the p-i interface over 2/3 of the i-layer, with different initial doping concentrations (undoped (top), 1 ppm (middle), 2 ppm (bottom)). With exception of the i-layer doping, the solar cells correspond to the standard solar cell of Figure 3.3.

Collection in the i-layer

Figure 4.22 shows the collection behaviour before and after light-soaking. In the annealed state, the graded doped cells show the typical suppression of the p-side collection (as seen in Figure 4.6). The degree of suppression is increasing with growing doping concentration. At the n-side, as expected, the collection remains near *100 %*.

After the light-soaking, the boron doped cells show recovery of the p-side collection. The location and degree depends strongly on the doping concentration. For the '1 ppm' doped cell, the recovery is almost complete, i.e. even very near the p-i interface collection values close to unity are reached. Differently from this, the '2 ppm' doped cell shows practically no recovery at the p-i interface itself, but only in the central regions of the i-layer. At the n-side on the other hand, some decrease of the collection is observed, but as intended by the doping, the decrease is much smaller than in the undoped cell. The comparison of the collection of all three solar cells shows that a suitable graded boron doping profile can in fact, through the displacement of the electric field in the i-layer, gradually shift the collection from a high p-side collection to a high n-side collection. More important, during this gradual shift, at an optimal doping strength ('1 ppm'), the degraded state collection is increased at the p-side but not yet strongly reduced at the n-side, such that the average collection is actually increased over the undoped case. The fact that this is achieved strongly indicates that undoped cells suffer indeed from an inhomogeneous electric field distribution in the degraded state. Also, the increased average collection demonstrates that there is a range where low-level boron doping can be beneficially applied, with the gains due to the electric field modifications being at least higher than the losses due to a suspected doping induced deterioration of the i-layer material properties.

Solar cell performance under different illuminations

Figure 4.23 compares the solar cell performances (efficiencies) of the different cells, before and after degradation. In the annealed state, in agreement with the collection measurements, for the illuminations mostly absorbed at the p-side or in the bulk of the i-layer (p-side AM1.5 and red

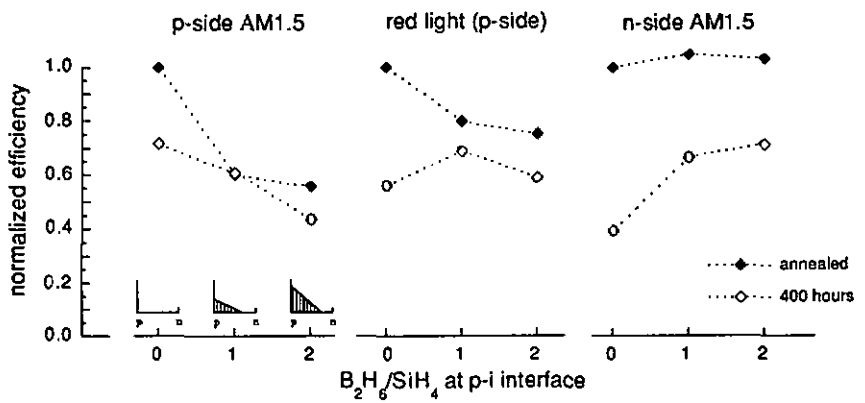

Figure 4.23: Solar cell efficiency of graded boron doped p-i-n solar cells (same as in Figure 4.22) for different illuminations, in the annealed state, and after 400 hours of light-soaking. The solar cell efficiencies are for each illumination normalised with respect to the annealed state efficiency of the undoped cell. The respective efficiencies of the undoped cell are 7.5 % for p-side AM1.5, 2.6 % for red light, and 6.0 % for n-side AM1.5.

light), the boron doped cells show low efficiencies as compared to the undoped cell. The n-side AM1.5 efficiencies are not affected by the doping. These trends correspond to those observed for the boron doped cell in general (section 3.2.1).
After the light-soaking, the undoped cell still performs best under p-side AM1.5 illumination, but the difference to the '1 ppm' doped cell is smaller. For n-side AM1.5 illumination, the increased n-side electric field of the boron doping leads to a clearly higher degraded state efficiency of the boron doped cells. For the conversion of homogeneously absorbed (red) light, the degraded state efficiency of the '1 ppm' doped cell performs better than the undoped cell, and also better than the more strongly doped cell. The more homogenous, and on the average higher collection of the '1 ppm' doping concentration measured at short-circuit condition (Figure 4.22) is thus found to translate into an optimal conversion efficiency for homogeneously absorbed light.

Current voltoge curves

Figure 4.24 compares the JV-curves of the undoped, and the 'optimally' ('1 ppm') boron doped solar cell. The undoped cell degrades as discussed in section 3.2, with the degradation of the currents clearly larger for red light than for AM1.5 light conversion.

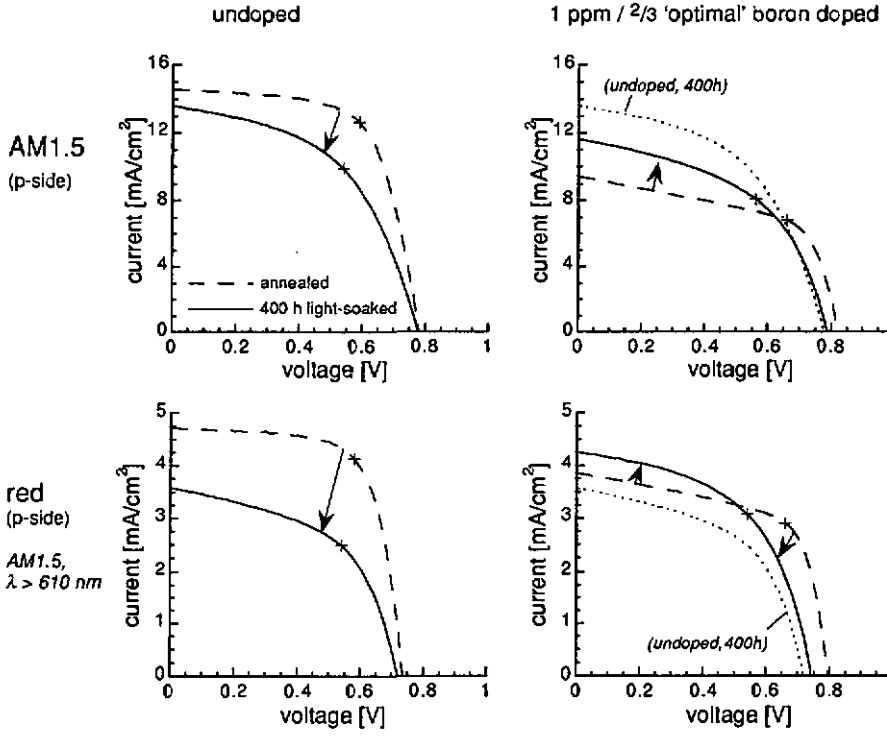

Figure 4.24: JV-curves of the undoped, and the 1 ppm / 2/3 'optimal' graded boron doped p-i-n solar cell (same cells as in Figure 4.22), in the annealed state, and after 400 hours of light-soaking, for p-side AM1.5 (top), and red light (bottom). The + symbols mark the maximal power points.

In the JV-curves of the 'optimally' boron doped cell, the light-soaking causes considerable recovery effects, especially in the low forward voltage range. Towards V_{oc}, the currents decrease as in the standard cells. This leads to an unusual translation of the maximal power point toward higher currents, and to relatively stable efficiencies (for AM1.5 illumination, the efficiency actually stays constant, see Figure 4.23). For the conversion of the red light illumination, this relative stability, together with the fact that the currents in the undoped cell degrade very strongly under this illumination, leads to the better degraded state performance of the boron doped cell.
The red light degraded-state JV-curves of the doped and undoped cell in fact show considerable resemblance to the modelled red light JV-curves (Figure 4.20, right) with a constant and with a distorted electric field, respectively. This indicates that the solar cell model employed above might not be too far from the actual physical reality, at least as far as the major effects of the light-induced defects on electric field and recombination in p-i-n solar cells are concerned.

4.3.3 Optimal doping and estimation of the defect concentration

p-side collection recovery, and its link to the defect density

The above series of solar cells has clearly shown that there exists a well defined optimal doping concentration for red light conversion. Beyond this concentration, the performance of the doped cells again decreases because the p-side collection remains suppressed after light-soaking. The capability to recover the p-side collection up to the range of the average i-layer collection is in fact indispensable for a successful doping scheme. If this recovery is not achieved, the region at the p-side is lost to the collection, and the compensation is thus too strong.
Figure 4.25, left, shows the collection close to the p-i interface (represented by the p-side spectral response at 400 nm) for the graded boron doped cells discussed above. A high degree of recovery is observed in the '1 ppm' doped cell, whereas for the '2 ppm' cell the p-i interface collection remains suppressed also after the light-soaking. In fact, as seen in Figure 4.22, bottom, the '2 ppm' doped cell shows substantial recovery only in the central part of the i-layer, where again the boron doping

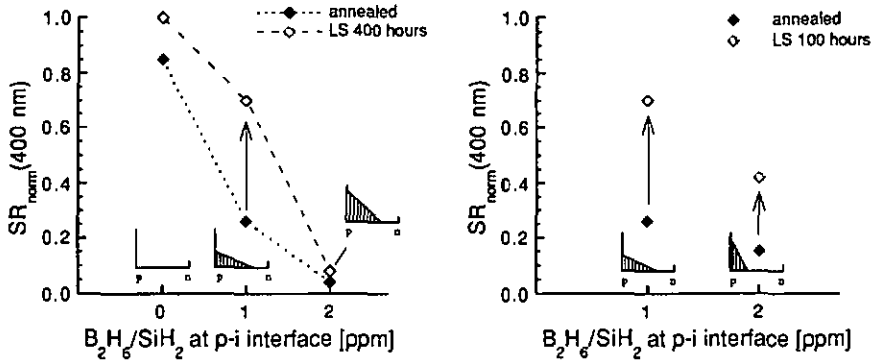

Figure 4.25: Normalised p-side spectral response at 400 nm (at 0 V, with red bias-light) for different graded boron doped p-i-n solar cells, in the annealed state, and after 100 hours of light-soaking. Left: solar cells of Figure 4.22; right: comparison of 1 ppm / 2/3 and 2 ppm / 1/3 linearly graded boron doped cells.

concentration is in the range of 1 ppm. It thus appears that through the degradation, space-charge effects of 1 ppm boron doping can be offset by the positive dangling-bond charge, but not the effect of 2 ppm boron doping. This threshold of the recovery capability as a function of the boron doping concentration allows to directly estimate the degraded state dangling-bond density, by assuming that at the recovery threshold the dangling-bond density N_{DB} equals the acceptor concentration N_A at the p-i interface.

With the concentrations of acceptors N_A determined to be of about $3.5 \cdot 10^{16} cm^{-3}$ in 2 ppm boron doped material (section 4.2.1), and with the threshold of recovery between 1 and 2 ppm (Figure 4.24, left), the density of dangling-bonds N_{DB} is thus estimated to be $2 - 4 \cdot 10^{16} cm^{-3}$. This estimation compares well with the findings of section 3.3, where the dangling-bond density was estimated to about $3 \cdot 10^{16} cm^{-3}$ from the blue light collection threshold.

Is the defect density estimation compromised by an only partial charging of the defects ?

It could be argued that the defect densities at the p-i interface are systematically underestimated due to an only partial positive charging. In this view, the only partial charging would prevent a recovery of the p-side collection even if the total defect density was higher than the acceptor concentration (Figure 4.26: forbidden case). This argument however does not hold: If one admits that the initial state suppression of the p-side collection is due to a cancelled electric field at the p-i interface, then one must also admit that in this low electric field region virtually all dangling-bonds are positively charged (Figure 4.26: allowed case). This is because in the field free zone holes are majority carriers (back diffusion of holes from the p-layer). Only if the potential would start dropping directly from the interface could the dangling-bonds take a reduced degree of charging. But then again a recovery would be observed. In summary it is not imaginable that the total dangling-bond density is significantly larger than the acceptor density, and yet the collection at the interface stays suppressed.

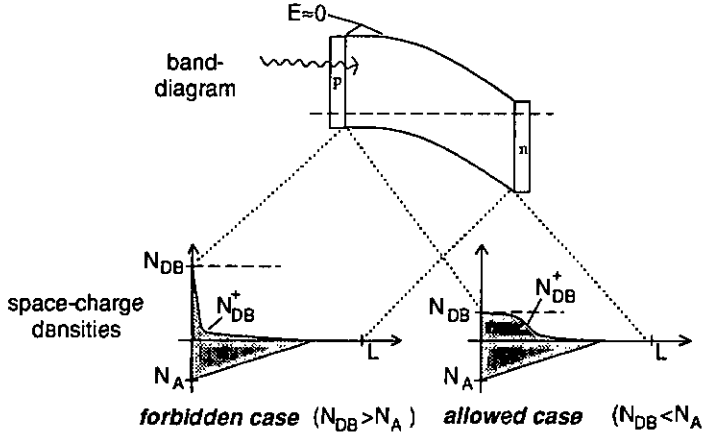

Figure 4.26: Schematic band-diagram, and different imagined space-charge distributions, in a low-level boron doped p-i-n cell, for the case of the p-i interface collection remaining suppressed after degradation (for discussion see text).

Influence of the boron doping profile depth on the defect density estimation

It might further be argued that the estimation of the dangling-bond density could depend not only on the matching of acceptor and dangling-bond density at the p-i interface, but also on the detailed shape of the whole doping profile. But the shape of the doping profiles matters only in the sense that very shallow acceptor doping profiles can not be employed to estimate the defect density. This is because shallow doping profiles loose their capability to suppress the p-i interface collection, independent of their p-i interface concentration, as soon as the total integrated acceptor charge is too small to build-up the full i-layer electric field, and the electric field penetrates up to the p-i interface. To be able to correctly estimate the defect density, the doping profiles must thus reach deep enough to suppress the p-i interface collection in the annealed state. Only then a sufficient sharpness of the discrimination is achieved.

Figure 4.25, right, compares two graded boron doped cells that have the same integrated dopant charge, but different p-i interface doping concentrations. Clearly, it is the cell with the lower p-i interface doping that shows the larger collection recovery. This corroborates the model that it is indeed the doping concentration at the p-i interface that determines the recovery capability, and not the whole integrated dopant charge of the i-layer. If a degraded state collection higher than 50 % is taken to be the criterion of recovery, the threshold is again situated between 1 and 2 ppm.

If one compares cells with the same p-i interface doping concentration, but different doping depth ('2 ppm / 2/3' doped cell of Figure 4.25, left, versus '2 ppm / 1/3' doped cell of Figure 4.25, right), the shallower doped cell shows a higher annealed state collection. As discussed above, this difference is explained with the doping being about to become too shallow to suppress the p-i interface collection in the cell with the lower doping depth.

Effect of the boron doping depth on the overall degraded state collection

Figure 4.27 compares the degraded state i-layer collection of the two cells that have the same total integrated boron doping, but a different shape of the doping profile (the ones that were compared in their p-side recovery in Figure 4.25, right). Clearly, the lower, but deeper reaching profile is more successful in homogenising the collection profile. Firstly, the recovery at the p-side is much more

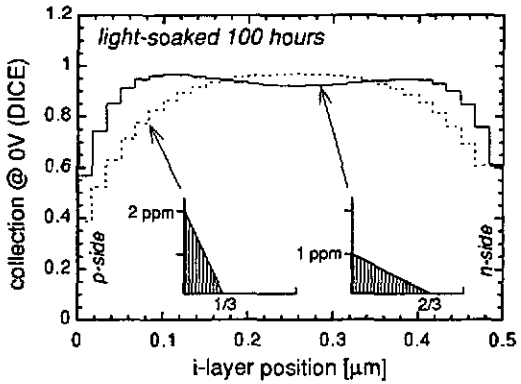

Figure 4.27: Comparison of the bifacial DICE collection probability profiles in '1 ppm / 2/3' and '2 ppm / 1/3' linearly graded boron doped cells after 100 hours of light-soaking.

complete, and secondly, in agreement with the modelling predictions, the deeper reaching doping causes the electric field to shift further towards the back of the i-layer, as shown by a higher collection in the n-side region. With too much electric field removed at the p-side, and not much electric field enhancement at the n-side, the narrower doped cell is expected to have its electric field concentrated in the central region of the i-layer, and indeed this is confirmed by the superior collection seen in those regions.

4.3.4 Considerations for the stacked cell application

Above, low-level i-layer doping was applied to single-junction p-i-n solar cells. The focus was on an improvement of red light conversion efficiency, with the goal to apply graded doped p-i-n cells as component cells in stacked cells. In view of a further optimisation of these low-level doped cells, it is important to note that for an application in a multijunction cell the single component cells can in principle not be optimised separately by optimising their respective power output alone. This is because in the multijunction cell, the component cells do not necessarily operate at their respective maximal power points of the single cell operation, but at an operation point that is influenced by all the series connected cells. As a consequence, power gains or losses measured for single junction operation do not directly translate into equivalent changes of the multijunction cell power output.
In an standard amorphous silicon 2-fold multijunction cell, the very thin first cell does practically not degrade and maintains a rather 'square' JV-curve. In contrast, the second cell JV-curve is typically 'flattened' after the light-soaking (see e.g. Figure 3.3). If the second cell JV-curve is improved, two basic categories of improvement can be distinguished: improvements increasing the current of the maximal power point (type I), or improvements increasing the voltage of the maximal power point (type II).
In Figure 4.28, left, the two types I and II are schematically depicted. The particularity of the stacked cell operation is that for equal power increases in the single-junction operation, the increase of the multijunction power is doubled for the improvement towards a higher current (type I). The added gain is due to an increase of the power produced in the first cell, which raises its operation current in parallel with the second cell.

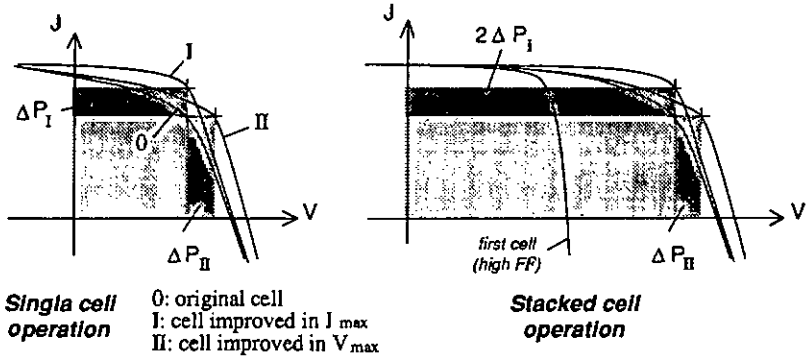

Figure 4.28: Schematic influence of different improvements of the 2nd cell JV-curve on the single-junction and on the stacked cell power output increase. The + symbols mark the maximal power points.

The above considerations made with respect to the JV-curve shape are related to the question of how the respective thicknesses of the two component cells should be matched to yield an optimal performance. In Figure 4.28, a matching of the currents at saturation was assumed.
It can be shown that the disadvantage of the type II cell can be reduced by a mismatching of the currents in the direction of a higher second cell current. This is confirmed by experimental results showing that it is advantageous to increase the second cell current over the first cell current [XU93]. However, Figure 4.29 shows that despite a correction by the mismatching, still the type I cells remain fundamentally more favourable for the stacked cell application than type II cells.

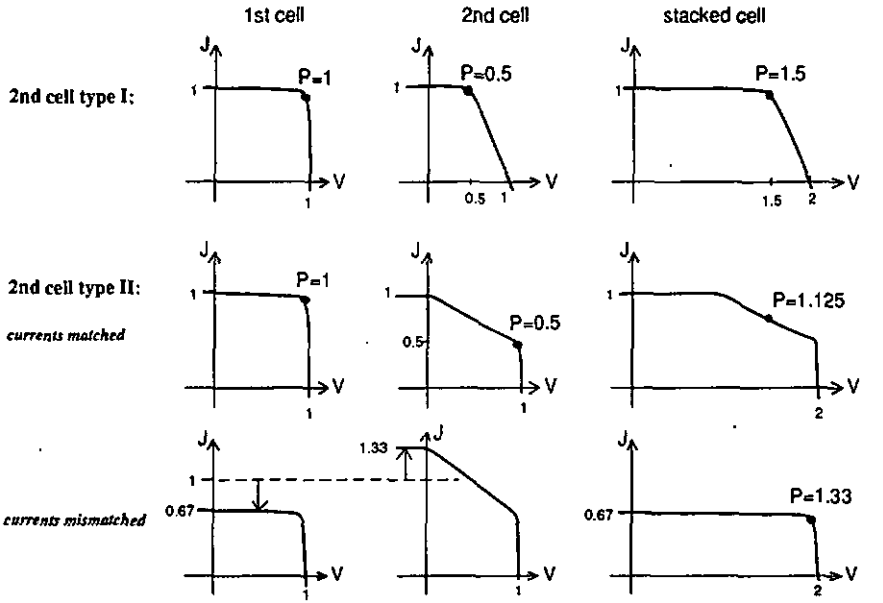

Figure 4.29: Schematic influence of different 2nd cell JV-curve shapes (type I and II, both having the same single-junction power output), and of the current mismatching on the stacked cell power output. The numbers are arbitrary units, P is the stacked cell output power.

Figure 4.30 shows the measured red light JV-curves of the 'optimally' low-level doped, and the corresponding undoped p-i-n solar cell (same as in Figure 4.24). Clearly, the type of improvement by the doping is towards a higher current (type I in Figure 4.27). In an idealised multijunction operation (assuming a first cell fillfactor of 100 %), the power increase is about doubled with respect to the increase seen in the single-junction operation. This shows that the graded boron doped cells, with their fast saturation of the current, are particularly favourable for the multijunction application.
In conclusion, the author likes to point out that JV-curve shape considerations are a necessity for the optimisation of stacked cell component cells, independent of the means of optimisation. Also, it can be learnt from these considerations that a detailed exploitation of these factors can lead to additional gains that are not apparent in a pure 'single-junction view' of p-i-n solar cells.

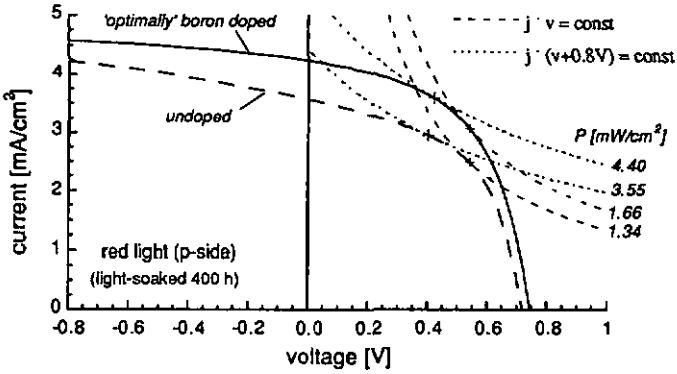

Figure 4.30: Measured red light (AM1.5, λ > 610 nm) JV-curves of the undoped, and the 1 ppm $l^{2}/3$ 'optimal' graded boron doped p-i-n solar cell after 400 hours of light-soaking (same curves as in Figure 4.24, bottom, right). The dashed lines mark the loci of constant single junction or constant, idealised 2-fold multijunction power output. The +symbols mark the maximal power points for the single junction or the 2-fold multijunction configuration.

4.4 Conclusions regerding low-level greded i-layer doping

The investigations of graded low-level doping of the i-layer are motivated by an assessment of the fundamental importance of the i-layer electric field in the operation of p-i-n solar cells. It is shown that in the amorphous silicon solar cells considered today, the i-layer defect densities after light-soaking are in a range that causes significant distortions of the i-layer electric field. Also, the results of material investigations concerning the quality of very low-level doped materials are judged not to exclude the beneficial application of dopants in the i-layer. It is thus proposed to systematically apply i-layer doping to tailor the electric field distribution for an optimised degraded state performance.

The practical implementation of different graded i-layer doping profiles, employing boron and phosphorus concentrations in the 1 ppm range, shows that the i-layer electric field distribution of p-i-n solar cells can be effectively manipulated over wide ranges. For the first time these manipulations are substantiated by direct electric field measurements based on µs charge transients. The detailed measured collection behaviours of the graded doped p-i-n solar cells are shown to arise from the sole effect of dopant induced space-charges on the electric field. In particular they do not indicate major material deterioration in the doped zones. Based on Poisson's equation, the collection in graded doped solar cells allows in fact to directly determine the concentration of active dopants in the doped sections of the i-layer.

The experimentally observed recovery of the collection during the light-soaking strongly indicates that in low-level doped solar cells, the dopant concentrations and the concentrations of the light induced defects are in the same range, and that the electric fields of the degraded state arise from a balance of the dopant and defect space-charges. The fact that recovery is observed only in the case of boron doping, but not for phosphorus doping, confirms that after light-soaking a positive space-charge is dominating the electric field in the i-layer.

The modelling, employing an original method to determine the doping profile for an ideal electric field compensation, together with the experimental recovery results indicate that the most beneficial i-layer doping profile is a boron profile starting at the p-i interface and gradually decreasing towards the n-side. An improvement is predicted to be more easily achieved in the conversion of homogeneously absorbed red light. It is thus proposed to apply graded boron doped cells as second cells of double stacked multijunction cells.

The experimental implementation of diborane doping profiles that decrease linearly from the p-i interface yields p-i-n solar cells with an improved degraded state conversion efficiency for homogeneously absorbed red light. In agreement with the modelling results, for the conversion of the strongly absorbed AM1.5 spectrum no improvements are observed.
This result shows that indeed the low-level graded i-layer doping is a viable method to increase the degraded state performance of amorphous silicon p-i-n solar cells. In particularly it is clearly demonstrated that, depending on the detailed device structure and illumination, the gains due to low-level doping are higher than the generally feared losses of dopant incorporation into the photovoltaically active i-layer.
A high degree of recovery of the collection at the p-i interface after the degradation is found to be a necessity for a successful boron doping scheme. Also, the capability of recovery as a function of the p-i interface doping concentration is shown to be a direct measure of the degraded state defect density in the i-layer. For the solar cells employed in the present investigation, this method yields a defect density of approximately $2 - 4 \cdot 10^{16} cm^{-3}$ in the p-i interface region.
Finally, the detailed JV-curve shapes of the graded boron doped cells are considered in view of the application in the multijunction cell. The faster saturation of the currents in the forward voltage range of the low-level doped cells is found to make these cells particularly apt for the stacked cell application.

5 Final conclusions and outlook

The present work was motivated by the idea that amorphous silicon is a most promising solar cell technology, with various fundamental advantages over other solar cell technologies. Amorphous silicon p-i-n solar cells and the details of their operation were judged to represent a field with many open questions and also with many improvement potentials yet to be discovered. In the consequent study, the author came to the following conclusions:

The role of the electric field distribution in the p-i-n solar cell operation

The distribution of the i-layer electric field, supplied by a fixed built-in potential of about 1 V, is the key to the photocarrier collection in an amorphous silicon p-i-n solar cell. Depending on the illumination mode, degradation status, or i-layer thickness of the p-i-n solar cell, the local space-charge due to either dangling-bonds, band-tail-states, or dopants can become large enough to significantly distort this electric field. These influences of the local space-charge have non-local effects on the electric field distribution in the whole i-layer, and can explain the carrier collection in the different regions of the i-layer.
With the electric field linked to the i-layer space-charge by Poisson's equation, the voltage dependent collection of p-i-n cells can be quantitatively explained in terms of the electric field extension in the i-layer. This direct link can be used to determine the absolute concentration of charged gap-states by a simple solar cell measurement (collection threshold method). Dangling-bond, band-tail-state, or dopant concentrations in the i-layer can be assessed in this way.

p-i-n solar cell modelling and characterisation

A numerical model which models only the i-layer with suitable boundary conditions is sufficient to qualitatively explain the features seen in the measurements of illuminated p-i-n solar cells. With the doped layers not modelled in depth, unnecessary complexity is avoided and the transparency of the modelling is increased.
For the characterisation of p-i-n solar cells, the differential spectral response under bias-light, and its analysis by the DICE method, are powerful tools for assessing the collection within the i-layer. The use of both p- and n-side measurements is essential to obtain information from all i-layer regions. The simultaneous use of p- and n-side collection data directly increases the achievable resolution of the DICE analysis (bifacial DICE method).

Light-induced degradation of p-i-n solar cells

The light-induced degradation of p-i-n solar cells is due to an increase of the dangling-bond density in the bulk of i-layer. This is concluded from a detailed comparison of measured i-layer collection data and numerical simulation results. Based on the observations of the bias-light dependency of the collection in degraded cells, the concept that the degradation is due to an increase of the defects at the doped-layer/i-layer interfaces can be eliminated.

The p/n-asymmetry of the i-layer collection, generally observed in p-i-n solar cells after degradation, is explained as the effect of the mobility difference between electrons and holes. This mobility difference leads to a predominant positive charging of the light-induced dangling-bonds, and consequenily to an asymmetry of the electric field, with a high field at the p-i interface, and a low field on the n-side of the i-layer. The charged tail-states on the other hand have a negligible influence on the electric field distribution in p-i-n cells of 0.5 µm thickness, and thus cannot be responsible for a p/n collection asymmetry.
The measurement of charged defects, based on the voltage dependent collection, indicates i-layer defect densities in the lower $10^{16}cm^{-3}$ range after light-soaking, with a trend of increasing defect densities from the p- to the n-side of the i-layer.

Low-level graded doping of the i-layer

With graded doping of the i-layer in the 1 ppm range it is possible to manipulate the distribution of the electrical potential in the i-layer in a controlled way, and over the full range of the built-in potential. These manipulations are in particular not limited by doping induced, or Fermi-level dependent defect growth.
During light-soaking, graded boron doped p-i-n solar cells show strong recovery effects. This confirms the model of a positive dangling-bond space-charge causing the p-n asymmetry in degraded p-i-n solar cells. Further, the capability of recovery as a function of the boron concentration at the p-i interface is a direct measure of the degraded state defect density in the i-layer.
In p-i-n cells with boron doping profiles linearly decreasing from the p-i interface, the degraded state collection in the i-layer is more homogeneously distributed than in cells without i-layer doping, and consequently the degraded state conversion efficiency for red light is improved. This is explained with the successful compensation of the positive dangling-bond space-charge by ionised acceptors, and a correspondingly more homogenous electric field distribution after the degradation. With their improved red light conversion efficiency, the low-level boron doped p-i-n cells, used as second cells, have the potential to increase the degraded state performance of multijunction cells.

Further investigations would be particularly interesting in the following areas:

- comparison of the defect-densities obtained by the collection threshold method in p-i-n cells with the defect-densities obtained by conventional film measurement methods (ESR, CPM, PDS)
- analysis of the distribution of the light-induced defects within the i-layer of p-i-n cells, and determination of the detailed defect creation mechanism, by application of various illumination and voltage-bias schemes for degradation, defect analysis by the collection threshold method, and comparison with solar cell numerical modelling
- implementation of graded low-level boron doped p-i-n component cells in multijunction solar cells, including a further detailed optimisation of the doping profiles
- application of the graded low-level doping in alloyed and graded-alloyed a-Si:H p-i-n cells, i.e. in silicon carbide (SiC), and silicon-germanium (SiGe) solar cells, as well as in alloyed interface buffer-layers [see REC94]

References

AIG84: M. Aiga et al, Proc. of 1st Int'l PVSEC (1984) p.225

ASE92: J.M. Asensi et al, Proc. of 11th EC Photovoltaic Energy Conf. (1992) p.769

ARC90: J.K. Arch et al, "A manual for AMPS/1D", Center for Electronic Materials and Processing, Pennsylvania State University, State College, PA, USA

ARC91: J.K. Arch, PhD thesis, Pennsylvania State University, State College, PA, USA

ARY87: R.R. Arya et al, Proc. of 3rd Int'l PVSEC (1987) p.457

BEN86: M.S. Bennet et al, Proc. of 7th EC Photovoltaic Energy Conf. (1986) p.547

BEN88: M.S. Bennet and K. Rajan, Proc. of 20th IEEE PVS Conf. (1988), p.67

BEN93: M.S. Bennet, Solarex Thin Film Division, privat communication (1993)

BER93: R. van der Berg et al, Solar Energy Materials and Solar Cells, No.31 (1993) p.253

BEY84: W. Beyer and H. Overhof, in "Semiconductors and Semimetals", Vol. 21, Part C (1984), p.257, ed. by Academic Press, Inc.

BRU92: R. Brüggemann et al, MRS Symposium Records, Vol.258 (1992), p.729

CAR76: D.E. Carlson and C.R. Wronski, Appl.Phys.Letters, Vol. 28, No. 11(1976) p.611

CAT85: A. Catalano, Proc. of 18th IEEE PVS Conf. (1985), p.1378

CAT86: A. Catalano, Solar Energy Materials, Vol.13 (1986), p.65

CAT91: A. Catalano et al, Solar Cells, Vol.30 (1991) p.261

CHI91: D. Chianese et al, Proc. of 10th EC Photovoltaic Energy Conf. (1991) p.755

CLA94: L. Clavadetscher et al, Proc. of 12th EC Photovoltaic Energy Conf. (1994) p.292

DAL93: V. Dalal, Iowa State University, private communication (1993)

DIE91: K. Dietrich, PhD thesis, Technische Universität München (1991), München, Germany

FAU84: B.W. Faughnan and R.S. Crandall, Appl.Phys.Letters, Vol. 44, (1984) p.537

FIS91: D. Fischer et al, Proc. of 10th EC Photovoltaic Energy Conf. (1991) p.201

FON81: S. Fonash, "Solar Cell Device Physics", Academic Press, New York (1981)

FOR88: C. M. Fortmann et al, J. of Appl. Physics, Vol.64, No.8 (1988) p.4219

FOR93: C. M. Fortmann and D. Fischer, Proc. of 23rd IEEE PVS Conf. (1993), p.966

FUJ93: S. Fujikake et al, Techn. Digest of 7th PVSEC (1993) p.285

GOR86: M. Gorn and N. Kniffler, Proc. of 7th EC Photovoltaic Energy Conf. (1986) p.582

GOR88: M. Gorn and N. Kniffler, Proc. of 8th EC Photovoltaic Energy Conf. (1988) p.940

GUH86: S. Guha et al, Appl.Phys.Letters, Vol. 49, No 4 (1986) p.218

HAR83: H. Haruki et al, Solar Energy Materials, Vol.8 (1983), p.441

HAT92: N. Hata and S. Wagner, J. of Appl. Physics, Vol.72, No.7 (1992) p.2857

HOU92: J. Hou et al, Proc. of 11th EC Photovoltaic Energy Conf. (1992) p.750

HUB93: J. Hubin, PhD thesis, University of Neuchâtel (1992), Neuchâtel, Switzerland

ICH90: Y. Ichikawa et al, Proc. of 21st IEEE PVS Conf. (1990), p.1475

ICH91: Y. Ichikawa et al, Proc. of 22nd IEEE PVS Conf. (1991), p.1296

ICH92: Y. Ichikawa et al, Proc. of 11th EC Photovoltaic Energy Conf. (1992) p.203

ICH93: Y. Ichikawa et al, Proc. of 23rd IEEE PVS Conf. (1993), to be published

ISO92: M. Isomura et al, Japanese J. of Appl. Physics, Vol.31, No.11 (1992) p.3500

ISO94: M. Isomura et al, Proc. of 12th EC Photovoltaic Energy Conf. (1994) p.1288

KAL89: J. Kalina et al, Solar Cells, Vol.27, No.1-4 (1989), p.341

KAU88: H. Kausche et al, Proc. of 8th EC Photovoltaic Energy Conf. (1988) p.866

KON82: M. Konagai et al, Proc. of 16th IEEE PVS Conf. (1982), p.1321

KOP92: W.J. Kopetzky, PhD thesis, Technische Universität München (1992), München, Germany

KOP93: W.J. Kopetzky and R. Schwarz, Appl.Phys.Letters, Vol.62, No.23 (1993) p.2959
KUS85: W. Kusian et al, J. of Non-Cryst.Solids, Vol 87&88 (1985), p.1489
KUS87: W. Kusian, PhD thesis, Technische Universität München (1987), München, Germany
KUS89: W. Kusian et al, Proc. of 9th EC Photovoltaic Energy Conf. (1989) p.52
KUS91: W. Kusian and H. Pfleiderer, AIP Conference Proc.,Vol. 234 (1991) p.290
KUW87: Y. Kuwano and S. Tsuda, AIP Conference Proc.,Vol. 94 (1987) p.378
LEE91: S. Lee et al, Appl. Phys. Letters, Vol. 13, No. 59 (1991) p.1578
LEC90: P. Lechner et al, MRS Symposium Records, Vol. 192 (1990) p.81
LEC91: P. Lechner et al, Proc. of 10th EC Photovoltaic Energy Conf. (1991) p.354
LEN94: M. Lenzlinger et al, SEV/VSE-Bulletin, Zürich, Switzerland, No.18(1994) p.45
LI92: X. R. Li et al, MRS Symposium Records, Vol. 258 (1992) p.929
LIN92: M.B. von der Linden et al, MRS Symposium Records, Vol.258 (1992), p.935
MAC90: J. Macneil et al, Proc. of 21st IEEE PVS Conf. (1990), p.1501
MAR84: H.P. Maruska et al, IEEE Trans. on Electron Devices, Vol.31, No.9 (1984) p.1343
MAT84: R.J. Matson et al, Solar Cells, Vol.11, No.2 (1984), p.105
MEI94: Ch. Meier, SEV/VSE-Bulletin, Zürich, Switzerland, No.10(1994) p.23
MIT85: K. Mitchell et al, Proc. of 18th IEEE PVS Conf. (1985), p.914
MOE85: M. Moeller et al, MRS Symposium Records, Vol. 49 (1985), p.325
NAT90: P. Nath et al, Proc. of 21st IEEE PVS Conf. (1990), p.1667
ONI91: M. Onishi et al, MRS Symposium Records, Vol. 219 (1991) p.421
PLA84: R. Plättner et al, Proc. of 1st PVSEC (1984) p.695
PRE86: W.H. Press et al, "Numerical Recipes", ed. Cambridge Univ. Press (1986)
QUR89: S. Qureshi et al, MRS Symposium Records, Vol. 149 (1989) p.649
RAG92: P. Ragot et al, Proc. of 11th EC Photovoltaic Energy Conf. (1992) p.553
REC94: B. Rech et al, Proc. of the 1st World Conf. on PV Energy Conversion, Hawaii (1994), to be published
RUB92: F.A. Rubinelli et al, Proc. of 6th PVSEC (1992) p.811
RUB94: F.A. Rubinelli, J. of Appl. Physics, Vol.75, No.2 (1994) p.998
SAU93: E. Sauvain et al, Solid State Communications, Vol.85, No.3 (1993) p.219
SAE92: R. Saeng-udom et al, Proc. of 11th EC Photovoltaic Energy Conf. (1992) p.609
SAK89: H. Sakai et al, Proc. of 4th PVSEC (1989) p.653
SCH88: H.E.P. Schade, United States Patent, No. 4.772.933, Sept. 20, 1988
SHA88: A. Shah et al, Proc. of 8th EC Photovoltaic Energy Conf. (1988) p.876
SHA92: A. Shah et al, MRS Symposium Records, Vol. 258 (1992) p.15
SIC83: P. Sichanugrist et al, Appl.Phys.Letters, Vol. 54, No.11 (1983) p.6705
SMO92: F. Smole and J. Furlan, Proc. of 11th EC Photovoltaic Energy Conf. (1992) p.765
STR82: R.A. Street, Phys. Rev. Letters, Vol.49, No.16 (1982), p.1187
STR83: R.A. Street, Phys. Rev. B, No.8 (1983), p.4924
STR91: R.A. Street, "Hydrogenated amorphous silicon", Cambridge University Press, (1991), Cambridge, GB
SZE85: S. M. Sze, "Semiconductor devices", (1985), John Wiley &Sons, Inc., New York, USA
TAK86: T. Takahama et al, Japanese J. of Appl. Physics, Vol.23 (1986) p.1538
TAK86/2: K. Takahashi and M. Konagai, 'Amorphous silicon solar cells', (1986), North Oxford Academic Publishers Ldt., London, GB
TAY72: G.W. Taylor and J.G. Simmons, J. of Non-Crystalline Solids, 8-10 (1972) p.940
UCH83: Y. Uchida et al, Solar Cells, Vol.9 (1983), p.3
UCH86: Y. Uchida, Proc. of 7th EC Photovoltaic Energy Conf. (1986) p.395
VAI86: F. Vaillant and D. Jousse, Phys. Rev. B, Vol. 34, No. 6 (1986), p.4088

VAN89: R. Vanderhaghen and C. Longeaud, MRS Symposium Records, Vol. 149 (1989) p.357
VAU93: S. Vaucher, 'Aspects ecologiques de la production des cellules solaires en silicium amorphe: Nouvelle etude, et comparaison avec le silicium cristallin', Inst. de Microtechnique, Neuchâtel, Switzerland, Nov. 1993
WIN94: K. Winz et al, Proc. of 12th EC Photovoltaic Energy Conf. (1994) p.85
WRO90: C.R. Wronski, Proc. of 21th IEEE PVS Conf. (1990), p.1487
WYR92: N. Wyrsch, PhD thesis, University of Neuchâtel (1992), Neuchâtel, Switzerland
XI85: J.P. Xi et al, Proc. of 18th IEEE PVS Conf. (1985), p.519
XU93: X. Xu et al, Proc. of 23rd IEEE PVS Conf. (1993), p.971
YAN91: L. Yang et al, Appl.Phys. Lett., Vol.59, No.7 (1991) p.840
YAN93: L. Yang, MRS Symposium Records, Vol.297 (1993) p.619

Table of symbols

Light/photons

λ	[cm]	wavelength
α	[cm^{-1}]	absorption coefficient
$p(\lambda)$	[Wcm^{-3}]	spectral power density
$\pi(\lambda)$	[cm^{-1}]	normalised spectral power density
$I, I(\lambda)$	[Wcm^{-2}]	light intensity
$\Phi, \Phi(\lambda)$	[$cm^{-2}s^{-1}$]	photon flow

Solar cell external quantities

j, J	[Acm^{-2}]	current density
J_m, J_{max}	[Acm^{-2}]	voltage at the maximal power point
J_{sc}	[Acm^{-2}]	short-circuit current
J_{sat}	[Acm^{-2}]	saturated current
j_{ext}	[Acm^{-2}]	external solar cell current
v, V	[V]	voltage
V_m, V_{max}	[V]	voltage at the maximal power point
V_x	[V]	threshold voltage
V_i	[V]	internal voltage
V_{ext}	[V]	external voltage
V_{oc}	[V]	open circuit voltage
FF	[-]	fill factor
FF_{sat}	[-]	saturated fill factor
η	[-]	solar cell conversion efficiency
P	[Wcm^{-2}]	power density
$SR(\lambda)$	[-]	spectral response
$SR_{sat}(\lambda)$	[-]	saturised spectral response
$SR_{norm}(\lambda)$	[-]	normalised spectral response

Solar cell internal quantities

G	[$s^{-1}cm^{-3}$]	generation rate
Φ_G	[$s^{-1}cm^{-2}$]	integrated i-layer generation rate
γ	[$s^{-1}cm^{-2}$]	generation rate distribution in the i-layer
R	[$s^{-1}cm^{-3}$]	recombination rate
Q	[cm^{-3}]	space charge density
E	[Vcm^{-1}]	electric field
x	[cm]	i-layer position
w	[cm]	space-charge width
n	[cm^{-3}]	electron density
p	[cm^{-3}]	hole density
j_p	[Acm^{-2}]	hole current density
j_n	[Acm^{-2}]	electron current density
d(x)	[-]	collection as a function of the i-layer position (DICE)

intrinsic layer boundary conditions

V_{bi}	[V]	built-in potential
S_{n0}	[cms^{-1}]	surface recombination velocity for electrons at the p-i interface
S_{pL}	[cms^{-1}]	surface recombination velocity for holes at the n-i interface
S_{nL}	[cms^{-1}]	surface recombination velocity for electrons at the n-i interface
S_{p0}	[cms^{-1}]	surface recombination velocity for holes at the p-i interface
$p_{equ}(0)$	[cm^{-3}]	equilibrium hole density at the p-i interface
$n_{equ}(L)$	[cm^{-3}]	equilibrium electron density at the n-i interface
L	[μm]	intrinsic layer thickness

general intrinsic layer material parameters

ε_r	[-]	relative dielectric permitivity
v_{th}	[cms^{-1}]	thermal velocity
μ_n	[$cm^2V^{-1}s^{-1}$]	free electron mobility
μ_p	[$cm^2V^{-1}s^{-1}$]	free hole mobility
C_μ	[-]	mobility ratio μ_n/μ_p
E_C	[eV]	energy of the conduction-band edge
E_V	[eV]	energy of the valence-band edge
N_C	[cm^{-3}]	effective density of states in the conduction-band
N_V	[cm^{-3}]	effective density of states in the valence-band
N_A	[cm^{-3}]	density of ionised acceptors
N_D	[cm^{-3}]	density of ionised donors

dangling bond parameters

N_{DB}	[cm^{-3}]	dangling-bond density
E_{DB}	[eV]	energy of the D^+/D^0 dangling-bond state
E_U	[eV]	correlation energy (energy offset of the D^- dangling-bond state
f^-, f^0, f^+	[-]	occupation (fullness) of the negatively, neutral, and positively charged dangling bond state
σ^0_{DB}	[cm^2]	cross section of the neutral dangling-bond state
C	[-]	cross section ratio of the dangling-bond state (charged/neutral)
σ^i_j	[cm^2]	cross section of the dangling-bond state i for carrier j
c^i_j	[s^{-1}]	capture rate of the dangling-bond state i for carrier j
e^i_j	[s^{-1}]	emission rate of the dangling-bond state i for carrier j
D^-, D^0, D^+		negatively, neutral, and positively charged dangling bond states
$U_{1,2,3,4}$		electron transitions between dangling-bonds and the conduction band
$H_{1,2,3,4}$		hole transitions between dangling-bonds and the valence band

band-tail states parameters

E_{0C}	[meV]	characteristic energy of the conduction-band tail-states
E_{0V}	[meV]	characteristic energy of the valence-band tail-states
N_{CBT0}	[$cm^{-3}eV^{-1}$]	density of states at the conduction-band edge
N_{VBT0}	[$cm^{-3}eV^{-1}$]	density of states at the valence-band edge
σ_n^{CBT}	[cm^2]	cross section of the conduction-band tail-states for electrons
σ_p^{CBT}	[cm^2]	cross section of the conduction-band tail-states for holes

σ_p^{VBT}	[cm^2]	cross section of the valence-band tail-states for electrons
σ_n^{VBT}	[cm^2]	cross section of the valence-band tail-states for holes
E_t	[eV]	trapping state energy level
σ_j^i	[cm^2]	cross section of the tail state i for carrier j
c_j^i	[s^{-1}]	capture rate of the tail state i for carrier j
e_j^i	[s^{-1}]	emission rate of the tail state i for carrier j
E_{FN}, E_{FP}	[eV]	pseudo Fermi-level for electrons and holes
E_{tn}, E_{tp}	[eV]	characteristic energies of Taylor and Simmons for electrons and holes

General physical constants

q	[As]	$1.6 \cdot 10^{-19}$	electron charge
h	[Js]	$6.6 \cdot 10^{24}$	Planck's constant
c	[ms^{-1}]	$3 \cdot 10^8$	speed of light
kT	[eV]	0.025	thermal energy at room temperature
ε_o	[AsV^{-1}m^{-1}]	$8.8 \cdot 10^{-12}$	*dielectric permitivity of the vacuum*

Acronyms

a-Si:H	hydrogenated amorphous silicon
a-SiC:H	hydrogenated amorphous silicon carbide
a-SiGe:H	hydrogenated amorphous silicon germanium
AM1.5	air mass 1.5 solar spectrum [MAT84]
BL	bias-light
CB	conduction band
CBT	conduction band tail
DB	dangling bond
JV	current voltage curve
LS	light-soaking
DICE	dynamic inner collection efficiency
RF	radio frequency
SIMS	secondary ion mass spectroscopy
SR	spectral response
SVD	singular value decomposition
TCO	transparent conducting oxyde
TOF	time-of-flight
VB	valence band
VBT	valence band tail
VHF	very high frequency

Acknowledgements

This work was supported by the Bundesamt für Energiewirtschaft (BEW) in the framework of the Neuchâtel amorphous silicon solar cell research project. I wish to thank for this continued support of renewable energy research. Also, the scholarship of the Schweizer Nationalfonds, enabling my one year stay at the University of Delaware (USA), is gratefully acknowledged.

Professor Arvind Shah takes a central role in the recent years of my career. I thank him for providing in Neuchâtel an ideal environment for amorphous silicon solar cell research, for leaving me a large freedom to develop my own ideas, and for his complete confidence in my efforts. Beyond this, I would like in particular to honour his continued and untiring promotion of a sensible photovoltaic solar energy technology. I hope that this commitment, often not in line with an easy success within the research establishment, will pay off in the long run.

I further owe very much to my mentors and friends Charles Fortmann and Herbert Keppner. To Charles for his hospitality during my stay in the US, and his extremely valuable help and critics during the accomplishment of this work. And to Herbert for his limitless availability to help with all the practical aspects of solar cell technology, as well for his optimism and good spirits at all times.

I also thank the members of the board of examiners, i.e. Dr. Schade, Prof. Ilegems, and Prof. de Rooij, for investing their time to read this thesis, and for their constructive comments.

Further I'd like to acknowledge the hospitality of the IEC at the University of Delaware, and of the group of Prof. Fonash at Penn State University, on occasion of my stay in the USA.

My colleagues and friends from the Neuchâtel amorphous silicon group, with their constant availability to discuss and help, contributed much to the present work. Their support, as well as that of members from different other sections of the Institut de Microtechnique, is gratefully acknowledged.

Last but not least, I'd like to thank in particular my wife Johanna, firstly for her linguistic help, but much more actually for her great moral support under all circumstances. Finally, I'd like to stress how much I appreciate my parent's and grandparent's interest in both my personal undertakings, as well as in the solar energy cause in general.